Physical Human-Robot Interaction with a Lightweight, Elastic Tendon Driven Robotic Arm

Modeling, Control, and Safety Analysis

TECHNISCHE
UNIVERSITÄT
DARMSTADT

Vom Fachbereich Informatik der
Technischen Universität Darmstadt
zur Erlangung des akademischen Grades eines
Doktor-Ingenieurs (Dr.-Ing.)
genehmigte

Dissertation

von

Dipl.-Ing. Thomas Lens
(geboren in Leuven, Belgien)

Referent:	Prof. Dr. Oskar von Stryk
Koreferent:	Prof. Dr. Karsten Berns (Technische Universität Kaiserslautern, Deutschland)

Tag der Einreichung:	23.05.2012
Tag der mündlichen Prüfung:	04.07.2012

D17
Darmstadt 2013

Contents

Abstract

Humans have since long desired to be assisted by robotic systems in productive and home environments. To fulfill this need, efforts are made to increase the cognitive abilities that robots lack to autonomously interpret their environment and human intentions. But equally important, new hardware and actuation designs are required to increase the safety and sensitivity of robots that operate in the vicinity of humans.

A main restriction of most current robot arm designs for physical human-robot interaction (pHRI) is the discrepancy of safety and dynamic performance in terms of, for instance, velocity and payload. This thesis therefore deals with the challenges involved in the development of fast robot arms that are safe for the operation in human-centered environments and for applications requiring close pHRI. It presents design guidelines for lightweight robot arms with elastic tendon actuation and, additionally, suitable methods for dynamic modeling and control and safety evaluation. This novel type of robotic arm aims at enabling automation of applications that combine critically high safety requirements for pHRI with high performance and flexibility demands. The BioRob-X4 robot arm is used as a robotic hardware platform for evaluation of the developed models and methods, which are tested in simulation and validated on the robot hardware.

In contrast to other robot arm designs, the actuation principle of the BioRob arm is non-modular in order to enable an extreme lightweight and low-inertia design with high safety and acceleration properties. The use of tendons spanning multiple joints, however, introduces kinematic coupling and the use of extension coil springs to maintain tendon tension and to decouple link and rotor inertia introduces undesirable joint oscillations. These effects have to be modeled accurately to investigate the behavior of the actuators and the whole arm dynamics in theory, simulation, and experiment and to allow for the development and design of model-based algorithms. Therefore, detailed mathematical models for the highly compliant and kinematically coupled tendon actuators and the low inertia link structure are developed and validated against experimentally measured data. The actuation models are analyzed with respect to highly dynamic motions inherent to low inertia link designs. Associated effects such as dynamic and static tendon slackening are discussed and from these considerations, guidelines for shaping the actuator characteristic output curves are derived.

State space partitioning of the manipulator is proposed for the formulation of the full robot arm dynamics model. By partitioning the model into three state spaces, the dynamics model of the robot arm can be formulated in joint space by reflecting the model states and parameters to the joint space. The presented approach is generally applicable to tendon-driven robotic arms and, furthermore, helpful in reducing the modeling complexity.

The design and hardware constraints of the investigated robot arm demand for the development of specific calibration and filter methods for the joint position and velocity states. Thus, a joint position sensor calibration method and a multilevel switching observer are developed that are both in general applicable to robotic arms with high joint elasticity. Based on the inverse dynamics model and the decoupling of tendon actuators spanning multiple joints we derive a position tracking controller by using the developed state space model segmentation. The proposed observer and control methods are evaluated in simulation and on the robot hardware.

A new prediction method for maximum collision and clamping forces based on the current dynamic state of the manipulator and its compliant actuators by monitoring also the potential energy stored in the springs is developed and applied successfully. A worst case safety evaluation considering the possibility of software and hardware failures is performed. In this context, the impact behavior of the elastic tendon actuators is compared to robot arms with backdrivable motors that are either stiffly or elastically coupled to the link and either coupled by tendon to the joint or placed directly in the joint.

The theoretical and experimental results presented in this thesis demonstrate the feasibility of constructing fast robotic arms with very high safety properties that are suitable for pHRI and operation in close and direct vicinity of humans. The developed detailed multibody dynamics models are applicable to lightweight manipulator arms with stiff kinematic link chains that are driven by highly elastic tendon actuators.

Keywords: *physical human-robot interaction*, *compliant tendon actuation*, *dynamic modeling and control*, *safe robot arm design*, *safety evaluation*

Zusammenfassung

Sowohl am Arbeitsplatz als auch im Haushalt besteht seit längerem seitens des Mensch der Wunsch, von Robotersystemen unterstützt zu werden. Um diesen Anforderung zu erfüllen, gibt es Bemühungen zur Steigerung der kognitiven Fähigkeiten, die Robotern momentan noch fehlt, um autonom ihre Umgebung und die Absichten des Menschen zu interpretieren. Gleichermaßen wichtig ist aber die Entwicklung von neuartigen Hardware- und Aktuierungskonzepten, die die Sicherheit und Feinfühligkeit von Robotern, die in der direkten Umgebung des Menschen agieren, steigern.

Eine Haupteinschränkung aktueller Roboterarmkonstruktionen für die physische Mensch-Roboter-Interaktion (pMRI) stellt die Diskrepanz von Sicherheit und dynamischer Performanz, beispielsweise in Bezug auf Geschwindigkeit und Traglast, dar. Die vorliegende Arbeit setzt sich daher mit den Herausforderungen auseinander, die die Entwicklung von schnellen und sicheren Roboterarmen für den Einsatz in menschlichen Umgebungen und für Anwendungen mit großem Fokus auf pMRI umfassen. Sie stellt Entwurfsrichtlinien für leichtgewichtige Roboterarme mit elastischer Seilzugaktuierung und zusätzlich geeignete Methoden für die dynamische Modellierung und Regelung und die Sicherheitsanalyse solcher Systeme vor. Das Ziel dieses neuen Roboterarmtyps besteht darin, die Automatisierung von Anwendungen zu ermöglichen, die kritisch hohe Sicherheitsanforderungen für pMRI mit hohen Performanz- und Flexibilitätsanforderungen kombinieren. Als Roboterhardwareplattform für die Evaluierung der entwickelten Modelle und Methoden, die in Simulation getestet und auf der Roboterhardware validiert werden, wird der BioRob-X4 Roboterarm verwendet.

Im Vergleich zu anderen Roboterarmkonstruktionen ist das Antriebsprinzip des BioRob-Arms nicht modular, um ein extrem leichtgewichtige Konstruktion mit geringer Trägheit und hohen Sicherheits- und Beschleunigungseigenschaften zu ermöglichen. Der Gebrauch von mehreren Gelenken umspannenden Seilen jedoch führt zu kinematischer Verkopplung und der Gebrauch von Schraubenzugfedern, um eine Seilvorspannung aufrechtzuerhalten und die Rotorträgheiten von den Robotergliedern zu entkoppeln, führt zu unerwünschten Gelenkoszillationen. Diese Effekte müssen präzise modelliert werden, um das Verhalten dieser Aktuatoren und der vollständigen Roboterarmdynamik in Theorie, Simulation und Experiment zu untersuchen und den Entwurf und die Entwicklung modellbasierter Algorithmen zu ermöglichen. Daher werden in dieser Arbeit detaillierte mathematische Modelle für die hoch nachgiebigen und kinematisch verkoppelten Seilzugaktuatoren und die kinematische Gliederkette mit geringer Trägheit entwickelt und anhand experimenteller Messdaten validiert. Die Antriebsmodelle werden hinsichtlich hoch dynamischer Bewegungen, die bei kinematischen Gliederketten mit niedriger Trägheit auch mit leistungsschwachen Antrieben vorkommen, analysiert. Hierbei werden assoziierte Effekte wie dynamische und statische Seillockerung diskutiert und, basierend auf diesen Überlegungen, werden Entwurfsrichtlinien für das Formen der charakteristischen Aktuatorkurven hergeleitet.

Für die Formulierung des vollständigen Roboterarmdynamikmodells wird eine Zustandsraumpartitionierung des Robotarms vorgeschlagen. Durch die Partitionierung des Modells in drei Zustandsräume kann das Roboterarmdynamikmodell anhand reflektierter Modellzustände und -parameter im Gelenkraum formuliert werden. Das vorgestellte Verfahren ist im Allgemeinen auf durch Seilzug aktuierte Roboterarme anwendbar und erweist sich zudem als hilfreich, um die Modellkomplexität zu reduzieren.

Die Design- und Hardwareanforderungen des untersuchten Roboterarms erfordern die Entwicklung spezifischer Kalibrierungs- und Filtermethoden für die Zustände der Gelenkwinkel und -geschwindigkeiten. Daher werden eine Kalibrierungsmethode für die Gelenkwinkelpositionssensoren und ein mehrstufig schaltender Beobachter, die beide im Allgemeinen auf Roboterarme mit hoher Gelenkelastizität anwendbar sind, entwickelt. Basierend auf dem Inversdynamikmodell und der Entkoppelung der mehrere Gelenke umspannenden Seilzugaktuatoren leiten wir anhand der entwickelten Zustandsraummodellsegmentierung einen Positionsfolgeregler her.

Anhand des aktuellen Dynamikzustands des Roboterarms und der nachgiebigen Aktuatoren und der zusätzlichen Überwachung der in den Federn gespeicherten potentiellen Energie wird eine neue Prognosemethode für maximal auftretende Kollisions- und Einklemmkräfte entwickelt und erfolgreich eingesetzt. Es wird eine Worst-Case-Sicherheitsanalyse, die die Möglichkeit von Software- und Hardwareausfällen berücksichtigt, durchgeführt. In diesem Zusammenhang wird das Aufprallverhalten des von elastischen Seilzugaktuatoren angetriebenen Roboterarms verglichen mit dem Kollisionsverhalten von Roboterarmen mit nicht selbsthemmenden Motoren, die entweder steif oder elastisch an das Robotergelenk gekoppelt sind und entweder über Seilzüge mit dem Gelenk verbunden oder direkt im Gelenk platziert sind, verglichen.

Die in dieser Arbeit vorgestellten theoretischen und experimentellen Ergebnisse belegen die Machbarkeit, schnelle Roboterarme mit sehr hohen Sicherheitseigenschaften zu konstruieren, die für pMRI und den Einsatz in direkter Umgebung des Menschen geeignet sind. Die entwickelten detaillierten Mehrkörperdynamikmodelle und die daraus abgeleiteten Methoden sind anwendbar auf leichtgewichtige Roboterarme mit steifen kinematischen Gliedketten, die durch hochelastische Seilzugaktuatoren angetrieben werden.

Stichworte: *physische Mensch-Roboter-Interaktion, nachgiebige Seilzugaktuierung, dynamische Modellierung und Regelung, sicheres Roboterarmdesign, Sicherheitsevaluierung*

Acknowledgments

I would like to warmly thank some people who accompanied me through my thesis.

Oskar von Stryk as my supervisor provided me with the possibility to work on this interesting topic. I would like to thank him for his continuous support, valuable suggestions and the stimulating discussions. I would also like to thank the advisory committee, especially Karsten Berns as my second referee, for valuable feedback.

Bernhard Möhl had the original idea to transfer the properties of the human arm and musculoskeletal system to the mechanical design of lightweight and elastically actuated robotic arms. He provided me with many inspiring thoughts at the beginning of my work.

My colleagues Sebastian Klug, Jürgen Kunz, and Jérôme Kirchhoff closely worked with me and devoted their time and energy to improving the BioRob arm and have been a continuous source of inspiring ideas. The other members of our group also provided me with many useful hints and tips.

I would also like to thank our long-year cooperation partners Andreas Karguth, Christian Trommer, and Markus Schweitzer from TETRA Gesellschaft für Sensorik, Robotik und Automation mbH, who constructed the BioRob arm hardware.

Very special thanks go to Katayon Radkhah for her invaluable thematic and moral support and fresh ideas and views in the field of robotic systems with highly elastic musculoskeletal actuation.

List of Figures

List of Tables

Symbols

Robot and Actuator Kinematics

N	[-]		degrees of freedom (DOF)
q_i, $\dot{q}_i$, $\ddot{q}_i$			angular position, velocity, and acceleration of joint i
θ_i, $\dot{\theta}_i$, $\ddot{\theta}_i$			angular position, velocity, and acceleration of motor rotor i
$\boldsymbol{q}$	[rad]	$N \times 1$	angular joint position state vector
${}^{\mathrm{e}}\boldsymbol{q}$	[rad]	$N \times 1$	angular joint position state vector with respect to the elastic actuator input state space
${}^{\mathrm{m}}\boldsymbol{q}$	[rad]	$N \times 1$	angular joint position state vector with respect to the motor state space
$\boldsymbol{\theta}$	[rad]	$N \times 1$	angular motor position state vector
${}^{\mathrm{j}}\boldsymbol{\theta}$	[rad]	$N \times 1$	angular motor position state vector with respect to the joint state space
${}^{\mathrm{e}}\boldsymbol{\theta}$	[rad]	$N \times 1$	angular motor position state vector with respect to the elastic actuator input state space
$\boldsymbol{\tau}_{\mathrm{m}}$	[Nm]	$N \times 1$	motor torque
$\boldsymbol{\tau}_{\mathrm{e}}$	[Nm]	$N \times 1$	elastic actuator torque with respect to the actuator input state space
$\boldsymbol{J}_{\mathrm{g}}$	[-]	$N \times N$	diagonal gearbox transmission ratio Jacobian
$\boldsymbol{J}_{\mathrm{t}}$	[-]	$N \times N$	tendon Jacobian and coupling matrix
${}^{0}\boldsymbol{J}_{\mathrm{N}}$		$6 \times N$	robot arm end-effector Jacobian
θ, α	[rad]		rotational Denavit-Hartenberg parameters
d, a	[m]		translational Denavit-Hartenberg parameters
${}^{0}\boldsymbol{r}_i$	[m]	3×1	position of coordinate frame i with respect to the base frame
${}^{0}\boldsymbol{R}_i$	[rad]	3×3	orientation of coordinate frame i with respect to the base frame

Elastic Tendon Actuator

k	[N/m]	spring stiffness
k_{e}	[Nm/rad]	input stiffness
${}^{\mathrm{j}}k_{\mathrm{e}}$	[Nm/rad]	output stiffness
d_i	[Ns/m]	tendon damping
d_{e}	[Nms/rad]	input damping
${}^{\mathrm{j}}d_{\mathrm{e}}$	[Nms/rad]	output damping
z_{g}	[—]	gear ratio
z_{p}	[—]	kinematic transmission ratio
z	[—]	total transmission ratio between motor and joint
x_i	[m]	spring elongation
l_{r}	[m]	spring rest length
l_{p}	[m]	prestretched spring deflection
l_{max}	[m]	maximum spring elongation
F	[N]	spring force
r	[m]	motor pulley radius
R	[m]	joint pulley radius
I_{r}	[kg m^2]	rotor inertia
I_{g}	[kg m^2]	gearbox inertia
R_{a}	[Ω]	DC motor armature resistance
L_{a}	[H]	DC motor armature inductance
k_{t}	[Nm/A]	DC motor torque constant
k_{v}	[Vs/rad]	DC motor speed constant
τ_{m}	[Nm]	generated motor torque
${}^{\mathrm{e}}\tau_{\mathrm{m}}$	[Nm]	generated motor torque with respect to the elastic tendon actuator input
${}^{\mathrm{j}}\tau_{\mathrm{m}}$	[Nm]	generated motor torque with respect to the joint side
V_{a}	[V]	DC motor voltage
I_{a}	[A]	DC motor current

$\boldsymbol{M}(\boldsymbol{q})$	$[\mathrm{Nms^2/rad}]$	$N \times N$	mass matrix of the robot arm
$\boldsymbol{C}(\dot{\boldsymbol{q}}, \boldsymbol{q})$	$[\mathrm{Nms/rad}]$	$N \times N$	Coriolis matrix of the robot arm
$\boldsymbol{g}(\boldsymbol{q})$	$[\mathrm{Nm}]$	$N \times N$	gravitational torque vector of the robot arm
$\boldsymbol{I}_\mathrm{m}$	$[\mathrm{kg\,m^2}]$	$N \times N$	diagonal rotor and gearbox inertia matrix with respect to the motor side
${}^\mathrm{j}\boldsymbol{I}_\mathrm{m}$	$[\mathrm{kg\,m^2}]$	$N \times N$	rotor and gearbox inertia matrix with respect to the joint side
$\boldsymbol{D}_\mathrm{m}$	$[\mathrm{Nms/rad}]$	$N \times N$	diagonal viscous motor and gearbox friction matrix with respect to the motor side
${}^\mathrm{j}\boldsymbol{D}_\mathrm{m}$	$[\mathrm{Nms/rad}]$	$N \times N$	viscous motor and gearbox friction matrix with respect to the joint side
$\boldsymbol{D}_\mathrm{e}$	$[\mathrm{Nms/rad}]$	$N \times N$	diagonal viscous elastic actuator friction matrix with respect to the elastic actuator input
${}^\mathrm{j}\boldsymbol{D}_\mathrm{e}$	$[\mathrm{Nms/rad}]$	$N \times N$	viscous elastic actuator friction matrix with respect to the joint side
$\boldsymbol{K}_\mathrm{e}$	$[\mathrm{Nm/rad}]$	$N \times N$	diagonal elastic actuator stiffness matrix with respect to the elastic actuator input
${}^\mathrm{j}\boldsymbol{K}_\mathrm{e}$	$[\mathrm{Nm/rad}]$	$N \times N$	elastic actuator stiffness matrix with respect to the joint side
$\boldsymbol{\Lambda}(\boldsymbol{q})$		6×6	operational space inertia matrix at the end-effector
$\mathbf{v}_\mathrm{c}$		6×1	spatial velocity
k_c	$[\mathrm{N/m}]$		collision stiffness
l_c	$[\mathrm{m}]$		collision compression

1 Problem Statement and Motivation

Despite many efforts, automation in industrial applications based on robotic manipulators is still restricted to highly structured environments with fixed conditions, strictly separated from humans, for example as common in car production in automotive industry. Most of the automation solutions are also highly specialized and only cost-effective for mass production.

As production requirements change towards versatility and flexibility, industrial applications in less structured environments that are not strictly separated from humans, become increasingly important, such as in many small and medium enterprises (SMEs). Humans possess cognitive abilities that no machine can currently even nearly match and could therefore boost the flexibility and versatility of (semi-)autonomous production processes. This would, however, drastically change the requirements posed to the process. These new applications demand high collision safety, intuitive user interface and programming, the capability to flexibly change the surroundings and the place of operation as well as moderate installation and running costs.

Common industrial robots that are currently available on the market are typically not flexible and safe enough, oversized, or too expensive for these applications considering invest and running cost. Compared to biological arms these systems are highly stiffly actuated and exhibit a poor payload to dead weight ratio, leading to considerable deficiencies for a safe and efficient operation in direct surroundings of humans if the relatively large arm masses are moving fast.

If robots are to share workspaces or to even directly physically cooperate with humans, new developments for robot arms are needed. Many research projects therefore focus on building safe robots that can breach the boundary to direct cooperation of humans and robots [19, 4, 48]. Research over the last years indicates that biologically inspired compliant actuation and lightweight construction could help designing new types of robots that have more resemblance to key properties of the human arm and allow for safer and more flexible operation than conventional robotic arms with a rigid and heavy link structure and non-backdrivable motors [52, 45, 71, 63, 65]. These new robot designs ask for completely different methods for modeling, control, and programming than for conventional rigid robots, and they attracted increasing attention in research over the last decade .

1.1 Context

This thesis was motivated by the development of a novel type of robotic arms, the lightweight and compliant, biologically inspired BioRob arm with highly elastic coupled tendon actuation, in the scope of the BioRobAssist project [7]. Many applications in SMEs have only moderate demands regarding load and accuracy, but high demands regarding safety properties, performance and flexibility. In many cases, no automation solution for these applications exists. The features of the BioRob arm with loads up to 2 kg, inherent safety even at high velocities, and quick deployment and programming, match the requirements of these applications very well. The project therefore aims at deploying the BioRob robot arm in SMEs for efficient operation under frequently changing production conditions as a survey, inspection, and handling assistant. The hardware features of the BioRob arm make it an ideal candidate robotic platform for deployment as a service robot in applications with very strict safety requirements demanding flexible, efficient and quick programming and operation of the robot arm.

1.2 Contributions

To clarify the contributions of this thesis, first a very compact overview of the state of the art in safe robot arm design for physical human-robot interaction (pHRI) is given. Subsequently, the novel design approach of the BioRob arm is highlighted, showing the opportunities and challenges of the design and illustrating the need for developing new models and methods.

Short Overview of the State of the Art on Safe Robot Arm Design for pHRI

The common basic approach for the design of robotic arms intended for safe pHRI is the reduction of link weight. If the link weight is overly reduced, undesired elastic link effects occur under bending load. While it is possible to control elastic link structures, this comes at the cost of complex control methods which are only feasible for a few degrees of freedom and at the cost of a general tracking control performance degradation.

The design of a link therefore depends on the weight of the kinematic chain attached to that link and on the maximum load defined by the requirements of the robot arm application. The link weight can be further minimized by designing the link geometry using structural analysis to minimize load bending effects and by choosing a lightweight and stiff material, which is both a cost and manufacturing issue.

For a modular actuator-link design, the link and actuator form a unit and in addition to the loads of the attached links, each link has also to bear the weight of its actuator and of all the actuators of the remaining kinematic chain attached to that link. Using novel, lightweight actuators, such as pneumatic muscles, can be a solution to reduce the weight of the actuators. Another approach is non-modular actuation, such as connecting conventional actuators with cables to the joints. In this case, the actuators can be placed at the bottom of the kinematic structure, hereby removing the weight of the actuators from the links and also enabling a more lightweight link design.

In case of a collision the link and the motor inertia of robot arms with rigid actuation are both involved in the impact. Therefore it is nowadays widely recognized that a certain amount of transmission elasticity is beneficial to decouple the motor and link inertia in case of impacts to increase collision safety. This is a paradigm shift compared to conventional robot arm design, where elasticity and compliance were seen as by all means undesirable.

But still, the transmission elasticity is generally kept low because the control bandwidth degrades with increasing transmission elasticity. Some designs even rely solely on the inherent gearbox elasticity in combination with active compliance control. The control bandwidth of these approaches is limited by the sensors and actuators, which is why these robot arms show compliant behavior only for low and medium velocity collisions, and behave stiffly and less safe in case of high speed impacts.

High transmission elasticity is commonly considered as dangerous because of undesired link oscillations and the possibility to store energy in the springs. Transmission elasticity is rather regarded as a possibility to increase performance for cyclic, oscillatory, or ballistic tasks. It is seen as beneficial to regain properties, such as backdrivability, that are lost when using non-backdrivable motors. In fact, the combination of non-backdrivable motors with elasticity is recommended, because in that case little or no motor torque is required to hold the elastic energy.

Elastic Tendon Approach for High Performance Safety

Most of the described design approaches lack safety in case of high speed impacts and clamping. Therefore, the main design objective of the lightweight BioRob arm is high collision safety for high speed pHRI. The aim is to enable high performance applications with close human-robot cooperation, such as pick-and-place applications with cycle times of the human arm.

While for a long time mostly used in robotic hands [56, 49, 16, 50], tendon-driven actuation also has a great potential in reducing the mass and inertia of robotic arm links [54, 55, 41]. Compared to tendon actuation in robotic hands, tendons used in robotic arms are longer and have to bear stronger tension forces. It is also more complicated to avoid tendon slackening and to achieve a robust and well damped behavior.

The main design objective of the arm is high collision safety for high speed physical human-robot interaction (pHRI) and applications with low payloads of up to 0.5 kg [38]. The aim is to enable high performance applications with close human-robot cooperation, such as pick-and-place applications with cycle times as achieved by the human arm.

The robot arm design combines both radical lightweight design based on tendon actuation as well as preloaded elasticity between the geared motors and the joints realized by integrated springs in the tendons.

The low power motors use planetary gears with a low transmission ratio and are therefore backdrivable. An additional reduction ratio is achieved by using motor and joint pulleys of different size. Due to the antagonistic pulley actuation, most of the robot's mass can be located at the base of the robot arm. This results in low inertia and allows for installing less powerful and smaller motors and transmission elements reducing the mass of the robot arm significantly. The motors are partly placed near the base of the robot structure and partly used to counterbalance the weight of the links. The result is an almost gravitationally balanced robot arm, such that only a fraction of the available maximum motor torques are required for gravity compensation, leaving more of the motor torques to handle loads. As a consequence of the motor placing, the effective mass of the robot arm is extremely low, which effectively reduces the clamping forces caused by gravity. An interesting side effect of the lightweight links is that no motor or joint brakes are required.

The preloaded springs in the tendons have two functions. First, they help preventing slackening in the tendons, which is important for control. Second, they dynamically decouple the link and motor inertia, thereby increasing the safety properties of the robot arm and also protecting the geared motors and the tendons from force peaks, which are low pass filtered through the elasticity. This is an important issue for tendon-actuated robot arms, because high strain can cause plastic stretching or fatigue in unprotected tendons.

Challenges and Main Contributions

The result of the described approach is a non-modular actuation and a radical lightweight link design that is able to quickly accelerate to high velocities and exhibits high clamping and impact safety. The main safety concern stated in literature regarding high transmission elasticity is that energy stored in the springs can be dangerous and that low joint stiffness can cause high joint velocities and oscillations. This thesis proposes a real-time safety evaluation method to monitor the current collision and clamping safety level of the robot arm and shows how the backdrivable

property of the motors can be used to release spring energy that exceeds a predefined safety level, causing the energy to be transferred to the motor rotors, where it is dissipated. Thereby bridging the gap between the formerly contradictory design goals performance and collision safety. It is ultimately shown that the presented actuation design combined with the developed algorithms enables a high performance mode with a high level of safety for pHRI, whereas other robot arm designs have strictly separate performance and safety modes.

While the compliant tendon actuation is highly beneficial for safety, this novel actuation type demands for the development of new concepts and algorithms for oscillation damping, tracking control, and safety evaluation and monitoring to fully utilize the potential of such physically compliant robotic arms. Detailed models of the actuators and the full multibody system (MBS) dynamics are essential prerequisites for the development of most of these algorithms. The unusually low actuation stiffness and the kinematic coupling introduced by the non-modular elastic tendon actuation poses the main challenge in the development of the aforementioned algorithms. On the other hand, the extremely low actuation compliance combined with the drastic reduction of the link inertia, that is enabled by the tendon actuation approach, also offers completely new possibilities to enable close pHRI even at high robot arm velocities.

The main contributions of this work cover the kinematic and dynamic modeling, analysis, and control of this robot arm and its novel actuators. A major focus lies on the safety evaluation of the robot arm for applications with close pHRI and on the comparison with other actuation designs.

Kinematic and Dynamic Modeling of the BioRob-X4 Robot Arm

Most of the methods developed in this thesis are based on kinematic or dynamic models of the investigated robot arm. The tracking controller, for example, uses the inverse dynamics model, and the safety estimation is calculated using the kinematics and dynamics matrices. Therefore, the development and the experimental validation of detailed mathematical models of the robot arm and its actuators is the foundation of this thesis. The novel elastic tendon actuation design with integrated springs and kinematic tendon coupling requires special consideration for several reasons.

First, a particular novelty is the ability to preload the springs integrated in the tendons, which affects the characteristic impedance curve of the actuator. It is shown that the preloading spring force can be adjusted to largely cancel out the effect of Coulomb friction. Second, the transmission ratio introduced by the motor and joint pulleys and the kinematic tendon coupling increases the model complexity compared to standard elastic joint robot arm models. Therefore, a systematic approach is developed that divides the robot arm into several state spaces and allows the formulation of the dynamics equations with respect to each of these state spaces. This results in a large reduction of model complexity and allows to transform the dynamics model of the robot arm into the common elastic joint robot arm model. In this process, the robot arm states and parameters are reflected to the joint space. Thus parameters and states originally defined in different state spaces become comparable. For example, the motor position or the rotor inertia defined in the motor space can be compared quantitatively to the joint position or link inertia, respectively, defined in the joint space. The state and parameter transformation is also used at a later stage for collision safety evaluation to create comparable parameter sets for robot arms with different actuation designs.

The first step of modeling is the development of a detailed mathematical model of the kinematic and dynamic properties of the elastic tendon actuators with focus on single joint actuation. From the developed model the characteristic stiffness and damping curves are derived. In contrast to the models of robotic cable and belt actuation presented in literature, this thesis focuses on the highly dynamic use of tendons with viscoelastic transmission properties that lead to the occurrence of static and dynamic cable slackening. The effect of pretension and transmission elasticity and damping on dynamic and static tendon slacking is therefore thoroughly analyzed with respect to the impact on the actuator performance. From this analysis design guidelines are derived for shaping the characteristic curves by choosing the spring pretension force.

Because of the complex, non-modular design of the robot arm, one of the objectives of the modeling approach is to minimize the model complexity without sacrificing accuracy. To this end, a systematic approach is presented dividing the robot arm into several state spaces, namely the motor space, the elastic actuator space, the joint space, and the operational space. Transformation rules are derived to transform states, such as the motor or joint position and velocity, and model parameters, such as rotor and gearbox inertia and damping, between these different state spaces. The result is a reduction of the model complexity in such a way that the dynamics equations can be formulated coherently in one state space, which can be any of the defined spaces. Also, better physical understanding of the effect of particular parameters and better comparability of model properties are achieved. As will be shown, this method is especially useful when comparing the BioRob robot arm with its coupled elastic tendon actuation to robot arms with different actuation designs. Using the defined state spaces and the state space transformation approach, kinematic models of the tendon coupling and robot link structure are presented, which extend the previously derived model of a single link elastic tendon actuator to a whole arm coupled elastic tendon actuator. With these developments a complete MBS dynamics model of the robot arm is derived. Using the presented state space transformation method, the dynamics equations are expressed with respect to the joint state space and then reduced to the common model structure of elastic joint robot arms. The introduced method of state space division of the dynamics model is not limited to this specific robot arm and the different actuators examined in this work. It is characterized by general applicability for modeling complex mechanical systems.

Simulation and Experimental Validation

The dynamics models of the actuators and the link structure are validated using experimental data and by identification of the model parameters. For this purpose a simulation model was developed, which was also used for controller design, dynamic behavior and safety analysis.

In order to enable simulation of robotic arms with combinations of different types of actuators and to be able to investigate highly transient impact situations, as needed for the evaluation of impact safety and the quantitative comparison of different actuation designs, a modular simulation library for the presented model parts was developed. Using technical computing software, a combination of model-based programming for the complex physical models and class-based programming for data and parameter storage was chosen. This approach proved to be very efficient for comparing robot arms with different types of actuators and for transformation from a particular robot arm and actuator configuration to other configurations under the constraint of preserving properties such as the overall transmission ratio or reflected actuator inertia.

Dynamic Analysis and Control

Due to the particularly high joint velocity and spring deflection ranges of the BioRob robot arm approaches for joint position calibration and joint velocity filtering had to be developed as an important prerequisite for tracking control of the robot arm.

The quality of the measured joint position is essential for all model-based control methods. A calibration method is presented to enhance the readings of the compact, custom-tailored, medium-resolution joint sensors. The developed method is based on velocity-based separation of zero-gravity measurement data to take the hysteresis effects into account and on local polynomial regression filtering of the measurement sets. By this calibration method calibrated and smooth joint sensor measurements are obtained.

The second crucial state is the joint velocity, which is of particular importance for tracking control and vibration damping. It is not directly measured and has to be extracted from the medium-resolution joint position sensor. In contrast to the motor velocity calculation, which benefits from the transmission reduction ratios, numerical differentiation is not feasible. Moreover, a single filter as used for most robot arm designs is not sufficient because of the extreme joint velocity range achieved by the BioRob arm. To cover this wide velocity range, a switching Kalman filter is proposed as a velocity observer that aims at obtaining smooth estimations with low noise at low velocities and low time-delay estimations at high velocities that do not compromise the stability of the controlled system.

Finally, a position tracking controller based on the inverse dynamics model and the joint equilibrium positions is proposed and evaluated in simulation and experiments. As experimental setup, a practical pick-and-place application is chosen with trajectory velocities up to $2\,\mathrm{m/s}$.

Safety Evaluation

A main design criterion of the BioRob robot arm is to maintain a high level of safety even at high velocities and in case of hard- or software failures, which is in contrast to most current robot arm designs, which rely on the presumption that at least one of the safety mechanisms is activated in case of danger. In contrast to other evaluation studies, the safety evaluation presented in this work derives a worst case impact and clamping scenario assuming a high speed collision with the maximum end-effector velocity and an impact robot arm configuration which maximizes the effective end-effector mass. This means that the safety evaluation poses much higher requirements on the robot arm than other safety evaluations in literature.

To support the experimental safety studies, a realistic contact model with a finite state machine for friction and stiction modeling was developed in simulation and experimentally validated with collision experiments on a force plate. As a result of the safety evaluation a model-based prediction of maximum collision forces and stress is presented. Existing safety evaluation methods from literature focus on conventional robot arm design and do not cover the important safety issue of the actuation elasticity. The proposed method therefore extends these approaches to also incorporate an analysis of the potential energy stored in the springs. The method can be used to evaluate the online safety state of the robot arm or as offline evaluation of the desired trajectory in planning.

The safety evaluation is concluded by a comparison of the safety properties of elastic tendon actuation compared to other actuation designs. By defining worst-case trajectories and a realistic

impact scenario, properties such as impact forces, kinetic and potential energy, joint torques, and effective end-effector mass are discussed. Usual approaches assume that at least one of the safety mechanisms prevents or mitigates the effects of an undesired collision. The safety analysis performed in this thesis investigates the worst case clamping scenario at the maximum robot arm velocity without collision detection. The impact of particular design features, such as compliant or tendon actuation and hardware safety devices, on collision safety is evaluated and compared to other actuation and robot arm designs.

1.3 Outline

This thesis is organized as follows. **Chapter 2** discusses the state of the art in safe robot arm design for applications with pHRI. In **Chapter 3**, detailed dynamic models for the actuators and the complete MBS dynamics model are derived. **Chapter 4** presents the proposed position tracking controller and joint state filter algorithms. A detailed safety evaluation of the robot arm is presented in **Chapter 5**. The results of the thesis are summarized and discussed in **Chapter 6**.

2 State of the Art of Robotic Arms for Physical Human-Robot Interaction

The following key requirements are important for successful practical establishment of service robots, especially in small and medium enterprises (SMEs) and applications with an unstructured and shared environment for humans and robots:

- *Safety*: Inherent safety even at high velocities and in case of failures enable efficient and flexible operation with or near humans in unstructured production environments.
- *Flexibility*: Mobility and short installation and deployment times allow to quickly change the robot's location and to flexibly react to changing production conditions and current needs.
- *Usability*: Simple and intuitive programming that can be performed by untrained personnel.
- *Performance*: Task execution with speed and accuracy comparable to a human arm.

In contrast to conventional industrial applications, accuracy is in most cases less important than the listed requirements [4]. Further important requirements involve energy efficiency and the ability to operate the robot arm in the same workspace of humans without the need for costly and performance-reducing safety measures.

These requirements show that safety plays a crucial role for the deployment of robot arms in applications where human and robot workspaces are not completely separated. The branch of the research field Human-Robot Interaction (HRI) dealing with these safety-related issues and contact situations between robots and humans is physical Human-Robot Interaction (pHRI) [5]. The second branch, cognitive and social Human-Robot Interaction (cHRI) covers aspects of social interaction and communication between humans and robots [8].

The state of research concerning safety in HRI is discussed in Section 2.1 and safe robot arm design is discussed in Section 2.2.

2.1 Safety in Physical Human-Robot Interaction

Robots in human environments can pose a safety risk that is not easy to cope with. Many efforts are taken to increase safety for applications with pHRI. Especially during pHRI collisions can not always be avoided or are even part of the process. Therefore, a lot of research has been and is being conducted on safe robot arms to increase collision safety as needed for these applications.

Many capable demonstrators have been presented over the last years. Some of the research is focused on enabling active safety for conventional robotic arms using sensor based collision avoidance or collision detection and reaction methods. But the certification of safety is a huge challenge, because for humans sharing the workspace of the robot it requires high levels of safety even in case of hardware or software failures.

Beyond safety from injuries, perceived safety and convenience play also a very important psychological role in applications with pHRI. Due to the hardware limitation regarding safety of conventionally built robots, especially in case of high velocities, clamping situations, or hard- and software failures, new actuation designs for increased passive safety are being developed. One of the main design goals is meeting the strict safety requirements of pHRI applications without compromising performance.

2.1.1 Pre-Collision Safety

Collision safety can be divided in two phases, pre-collision and post-collision safety [23]. Pre-collision strategies aim at reducing the effects of an imminent impact, whereas post-collision strategies try to limit the forces the robot can apply while in contact with a person or object. Pre-collision safety can be obtained by padding the robot links, reduction of effective inertia by changing the robot arm configuration, as well as surveillance of the workspace around the robot by a virtual fence of non-contact sensors preventing collisions. Post-collision safety strategies include tactile sensors, active and passive compliance.

A pre-collision strategy to limit the maximum impact force that can be generated by a robot arm colliding with a static object to a preset value was proposed in [23]. A method evaluating explicit measures of danger was proposed in [33].

The aforementioned strategies and standard guidelines aim at actively reducing the impact forces and the effective robot arm inertia. They alone are therefore not appropriate for HRI applications. Elimination of hazards through passive pre-collision strategies such as reduction of the robot arm mass and inertia by mechanical design is more effective and more fail-safe. Still, active pre-collision safety methods have the advantage to allow the definition of a quantifiable value for the maximum impact forces, thus being an important supplement to passive pre-collision safety strategies. The surveillance of the workspace is also very useful, as it can significantly reduce the probability of a collision.

2.1.2 Post-Collision Safety

Lightweight design and active compliance combined with collision detection and reaction schemes can increase safety for robots [21]. Since the bandwidth of actively controlled compliance is limited to the bandwidth of the sensors, actuators, and controller frequency, more effort is necessary for applications with high velocity and safety requirements.

A rigid robot manipulator can be made actively compliant by control with additional sensors. Two approaches have been proposed to achieve active compliance: force control and impedance control. Both are not designed to control or limit collision forces of robots [23]. Because of limited sensor and actuator bandwidth, the system behaves stiff in case of a collision. High safety properties can only be obtained when limiting the maximum joint velocity and operating at speeds far below the possible maximum speed. A high performance reduction is the result.

Instead of actively controlling the behavior of the robot, mechanical compliance can be built into the joints or links. The advantage is the possibility to save energy in the elastic elements. As opposed to active, controlled compliance, mechanical compliance exhibits a delay-free compliant behavior in case of a collision. As a result, the motor and link inertia are physically decoupled. This is particularly important when using high gearbox ratios. In that case, the reflected motor inertia can be of the same magnitude as the link inertia. Contrary to active compliance, passive compliance therefore reduces the impact forces to a certain degree.

An early concept involving a constant elastic coupling between motor and link was the Series Elastic Actuator (SEA) [52]. When using a constant passive compliance design, a trade-off between performance and safety must be made, because the force and position bandwidth decline with increasing joint compliance, whereas compliance bandwidth increases. To overcome this limitation, variable compliance actuation is seen as a promising candidate. Several variable

impedance actuation concepts have been presented over the last years, such as distributed parallel actuation [72], antagonistic actuation [4], and others [63]. Almost all of the demonstrators of these concepts are still rather heavy and complex.

2.1.3 Safety Metrics

During the last decade, the safety evaluation of robotic systems attracted increasing attention in research. The main goal of most of the current research on safety is to avoid severe and lethal injuries. In that context, the HIC-index [66] is often used as a safety index for impacts for the head area, which is regarded as the most vulnerable part of the body.

For conventional industrial robots it makes sense to focus on the danger of severe injuries, for which the Head Injury Criterion (HIC) is a good measure. For lightweight service robots, further criteria for measuring the danger of lower severity injuries are needed.

Industrial safety standards, such as [1], have been conceived for industrial manipulators with the main goals of preventing bone fractures and laceration. For fast applications either a maximum dynamic power of 80 W or a maximum static force of 150 N are allowed.

A method to evaluate skin stress in blunt impact depending on the shape and material properties of the robotic arm was proposed in [68]. A detailed study of a realistic collision model of a robot arm with soft covering and human head with multi-layer structure for covering design to prevent soft-tissue injuries was presented in [51]. To evaluate the danger of contusions, a maximum impact energy density of $2.52\,\mathrm{J/cm^2}$ and for lacerations, the skin tensile strength of $\sigma = 10^6\,\mathrm{N/m^2}$ was used.

In contrast to safety, which can be defined as prevention of injury, pain is a very subjective measure. But nevertheless, it can be important for HRI applications to also consider pain limits. Pain thresholds can be given as separate pressure limits for the static and dynamic case. The lowest Pressure Pain Thresholds (PPT's) reported in literature refer to the temporal areas of the head [9, 26], with maximum static pressure of $\sigma_{\mathrm{s,max}} = 150\,\mathrm{kN/m^2}$ and maximum dynamic pressure of $\sigma_{\mathrm{c,max}} = 250\,\mathrm{kN/m^2}$.

According to an extensive study on robot arm safety in [22], unconstrained collisions (depicted in Fig. 5.6) without clamping are not as problematic as previously assumed with respect to injuries, even with heavier robots. However, constrained impacts are pointed out as the most difficult and dangerous safety issue (see Fig. 5.6). For such impacts with sharp objects a collision detection and reaction scheme was presented that is capable of preventing injuries up to a certain velocity limit [20].

2.2 Safe Link Structure and Actuation Design

Because of the hardware limitation of conventional robotic systems for high velocities, in clamping situations, and in case of hard- or software failures, new actuation designs for increased passive safety are being developed. Elasticity in the drivetrain and lightweight design are now widely seen as key features for safety. Because the bandwidth of actively controlled compliance is limited to the bandwidth of the sensors, actuators, and controller frequency, passive compliance is considered as essential requirement for intrinsic safety. This can be achieved by using an elastic element, e.g. a spring, in series with the actuator [52, 45, 36].

2.2.1 Compliant Actuation

Elasticity in the actuation of robotic arms was for a long time seen as undesirable. Research on SEAs [52] showed that mechanical compliance in the joint actuation can simplify force control in constrained situations, increase safety by the low-pass filtering of torque and force peaks between joints and gearbox (infinite compliance bandwidth), and increase performance of specific tasks because of the possibility to store mechanical energy in the elasticity. The increase of performance for throwing was also examined in [69].

There are also disadvantages when introducing a series elasticity in the joint actuation, namely reduced torque and force bandwidth and increasing complexity for oscillation damping and tracking control. Flexible link manipulators are also subject to current research. But these systems are even harder to control, especially several degrees of freedom. An overview over research on flexible joint and link systems with an emphasis on flexible links is given in [14]. A classification of elastic joint actuation principles is given in [63] and [72].

Elasticity can be realized by using inherently compliant actuators, such as artificial pneumatic muscles [6, 62] or by using elastic elements in series with standard geared motors [52, 35]. Additional actuators can be used to adapt stiffness or damping [57, 63, 2], or to combine actuators with complementary features [58].

Introducing elasticity can increase safety when using geared motors because of the decoupling of motor and joint. The degree of elasticity does not necessarily have to be high. In [22] it has been shown that even the elasticity introduced by Harmonic Drives can be sufficient to actively decouple the motor from the joint side in case of a collision.

But introducing elasticity does not result into more safety by default. It can be even dangerous since higher joint velocities than motor velocities are possible. In addition, there is always the possibility of a sensor, actuator or software malfunction. Therefore, a robotic arm should be intrinsically safe for humans by lightweight and safe design.

Furthermore, tracking control performance degrades as compliance is brought into the drive train [52, 25]. Variable impedance by changing the stiffness of the elastic transmission with two motors can be used to regain control bandwidth with high impedance while benefiting from low impedance during fast motions or in contact situations [63]. In contact situation, however, and in applications that benefit from energy storage, elasticity can increase stability and drastically reduce energy consumption [64, 69].

Industrial safety standards, such as [1], have been conceived for industrial manipulators with the main goals of preventing bone fractures and laceration. In fact, many applications in service robotics require high velocities in strongly unstructured environments, where impacts and clamping can occur on a frequent basis when making extensive use of pHRI. Using collision detection in these environments can be a serious problem, because a reaction to a collision in uncertain environments can be dangerous by itself.

Several approaches try to simultaneously achieve collision safety and force/position tracking accuracy. In most cases, however, these approaches are not fail-safe, often too heavy, and have to be operated at reduced speed near humans. Also, clamping is a concern, especially with joints with brakes and high transmission ratio (high reflected damping) and with heavy links. Without collision detection, effects such as clamping in near-singular configurations can pose a big threat [22], even for low-inertia robots. As additionally sensor, hardware and software failures

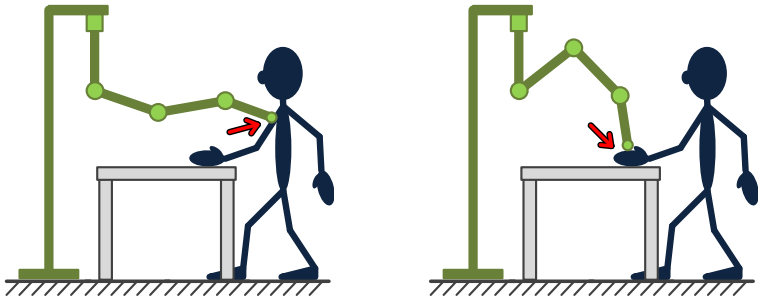

Figure 2.1.: Unconstrained (left) and constrained (right) collision (cf. [22]).

can occur, the use of low-power motors should be considered in order to reduce dangerous effects.

According to an extensive study on robot arm safety in [22], unconstrained collisions (depicted in Fig. 5.6) without clamping are not as problematic as previously assumed with respect to injuries, even with heavier robots. This is due to the HIC safety metric that saturates for robot structures with a reflected inertia higher than the body part of the colliding subject, e.g. human head (4 kg). However, constrained impacts are pointed out as the most difficult and dangerous safety issue (see Fig. 5.6). For such impacts with sharp objects a collision detection and reaction scheme has been presented that is capable of preventing injuries up to a certain velocity limit [20].

2.2.2 Low Inertia Design

Above approaches increase safety solely by active control and decoupling of motor and joint. There are also methods that additionally reduce the system's inertia. One of these concepts uses two combined actuators with complementing bandwidth features and connects the heavier and stronger actuator with a series elastic cable transmission to the joint [71]. Other concepts use cable transmission [54], or lightweight actuators with inherent compliant properties [6]. In [65] an intrinsically mechanically safe design for a manipulator has been presented that is capable of moving a useful payload of 1.2 kg by the use of low-power actuators applying a mechanical gravitation compensation design.

2.3 Conclusions

This chapter offered a short overview over the state of research and technology of robot arms for applications with pHRI. The limitations of conventional robotic arm designs for safe and cooperative HRI can be overcome to a certain extent, as shown in the project SMErobot, which presented the vision of a three-day-deployable integrated robot system and several technologies and demonstrators showing the feasibility of the concept [48]. Many SMEs, however, have to cope with frequently changing conditions of the production process. For these applications, there is a need for a mobile, cost-effective robot platform with installation, deployment and programming times of only a few minutes to be able to use the robot arm according to the current demand.

For these requirements robotic arms with safety and performance properties comparable to the human arm are needed. These properties can not be sufficiently achieved with conventional

robotic arm designs. This chapter presented a summary of new actuator and robot arm designs and control methods specifically developed for pHRI, resulting in demonstrators with remarkable features. Nevertheless, these robotic arm platforms rely to a certain extent on hardware devices or software control methods to ensure safety. In case of a hardware or software failure, safety is not guaranteed. An additional important aspect is that convenience and perceived safety play an important psychological role in HRI. Cooperation between humans and robots will only be effective if the common user does not think about the robotic arm as a threat.

This thesis therefore concentrates on a novel design of a lightweight robotic arm that uses elastic tendon actuation to achieve inherent safety even in case of very fast robot arm velocities.

3 Modeling and Simulation of Robotic Arms with Elastic Tendon Actuation

A short version of Section 3.2 was published in: Proceedings of the IEEE-RAS International Conference on Humanoid Robots 2012 [40]. A condensed version of Sections 3.4 and 3.6 was published in: Proceedings of the IEEE International Conference on Robotics and Automation 2013 [39].

This chapter outlines the kinematics and dynamics model required for the arm and a new coupled kinematics model which accounts for the elastic tendon driven robot.

The BioRob robot arm is based on an antagonistic, series elastic actuation concept inspired by the elastic muscle-tendon apparatus. Each joint is actuated by a DC motor coupled to the joint by four cables containing springs and other compliant elements as series elasticity. In addition to motor position sensors, also angular joint position sensors are used [31, 44].

The BioRob arm used in this scenario consists of four elastically actuated joints. Due to the antagonistic pulley actuation most of the robot's mass can be located at the base of the robot arm. Figure 3.1 illustrates the position of the motors and sensors in the robot arm. This results in low inertia and allows for installing less powerful and smaller motors and transmission elements reducing the mass of the robot arm significantly.

3.1 BioRob-Arm Design and Properties

The BioRob-X4 robot arm, depicted in Fig. 3.1, consists of four joints that are elastically coupled by cables with built-in translational springs to the electrical motors. Two of the motors are located in the first link and two as a counterweight in the second link. Thus, most of the mass is located near the base and the center of mass of the second link r_{c2} is located at the axis of joint 2 (cf. DH parameter a_2). The joint actuation principle is illustrated in Figure 3.18.

The built-in translational springs in the cables decouple the links and motors, similar to the original Series Elastic Actuator (SEA) [52], and enable additionally manual pretension, with the potential to decrease backlash effects. The low-pass filtering effect on force peaks protects the transmission system and geared motors from shocks (cf. Section 5), as elaborated in many previous works.

The joint elasticity k_e and the absence of joint brakes also enable high backdrivability, a property that is lost when using gearboxes, and increase the stability in contact situations. The design of BioRob-X4 allows the use of smaller motors with lower gearbox ratio z_g and rotor inertia I_r, eventually leading to low reflected rotor inertia. As can be seen from Table 3.7, the design of the robot arms leads to a link inertia lower than the reflected motor inertia in links 2–4. Decoupling of motor and joint inertia is therefore very important and effective for this design.

Without payload the robot arm is capable of performing extremely fast motions due to its low inertia. Fig. 3.2 displays such a trajectory with Cartesian velocities as high as $6.88\,\mathrm{m/s}$ with very low mean power consumption of 54 W for these high velocities. As can be seen, the dynamic peak power of the robot arm can easily exceed the 80 W limit for fast motions.

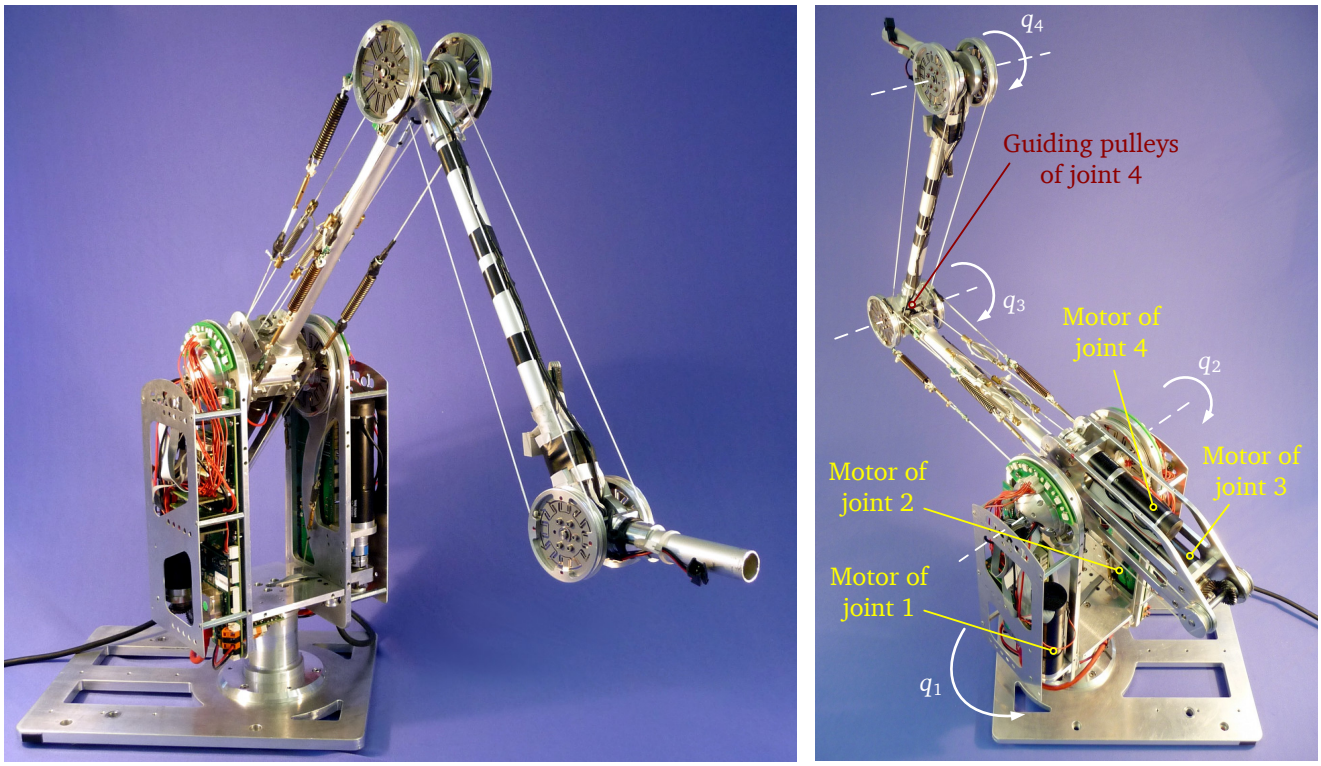

Figure 3.1.: BioRob-X4 (4 DOF) arm without gripper (left) and location of the motors (right).

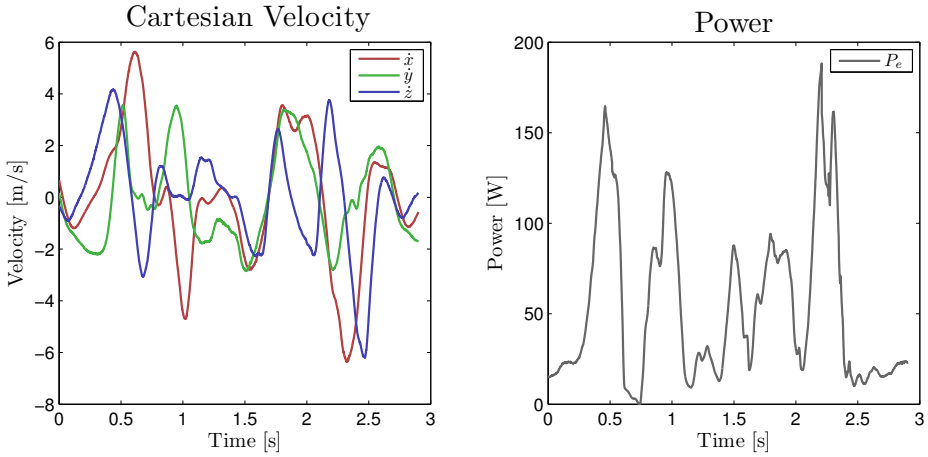

Figure 3.2.: Cartesian velocities and electrical power consumption of a fast trajectory.

The design leads to a very low overall weight of the robot arm of 4 kg (including power electronics), while still enabling it to carry an end-effector load of 2 kg without exceeding the maximum torques.

3.2 Single Joint Elastic Tendon Actuator Model

The actuation approach of the BioRob arm as shown in Figure 3.1 aims at combining the robust behavior of standard electrical motors with the safety characteristics of elasticity in the drivetrain and a radical lightweight design by using tendons to actuate the robot joints. When using

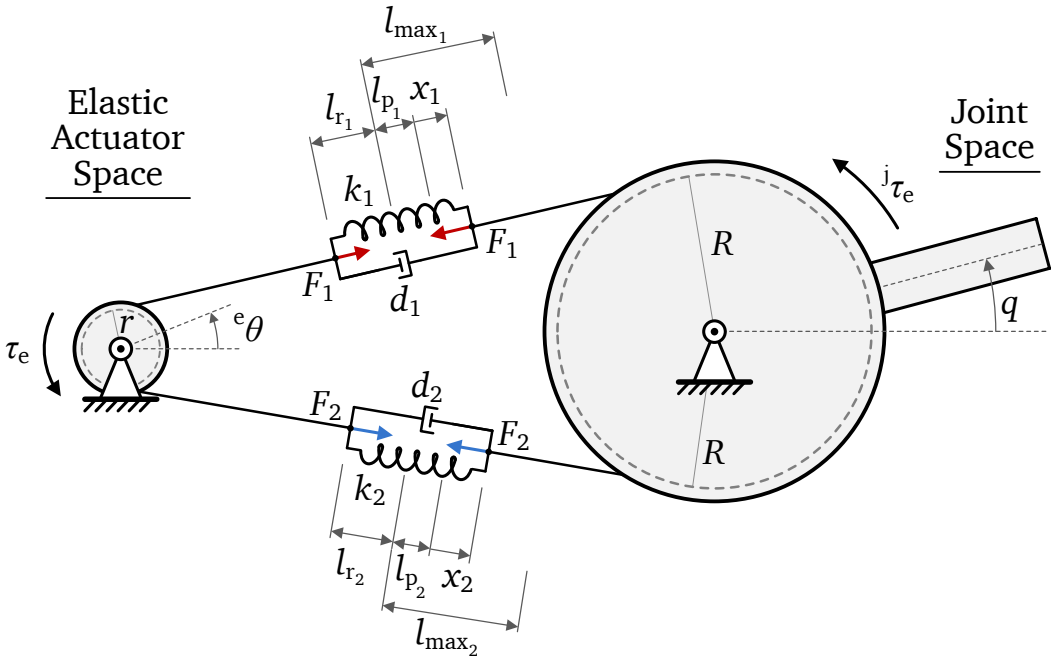

Figure 3.3.: Model of the elastic transmission with parameters motor pulley radius r, joint pulley radius R, spring rest length l_r, spring prestretched deflection l_p, maximum spring deflection l_{max}, and state variables angular joint position q, angular motor position with respect to the elastic actuator ${}^{e}\theta$, elastic actuator torque τ_e, elastic actuator joint torque ${}^{j}\tau_e$, spring force F, and spring deflection x with respect to prestretched length. The indices 1 and 2 stand for the upper and the lower spring, respectively.

tendons spanning multiple joints, additional friction is introduced. However, this comes also with several advantages. By using tendons, the motors can be placed near the base, thus reducing the robot arm's inertia. As an alternative, they can even be used as a counterbalance for the weight of the links. The reduction of mass and inertia allows to use smaller and less heavy motors and gears. In addition, by using elasticity in the tendons, the reflected rotor inertia and friction are dynamically decoupled from the link side, reducing shocks on the gearbox as well as on the environment in case of a collision.

In this chapter, a detailed mathematical model for a single joint elastic tendon actuator, as displayed in Figure 3.3, is derived. The specific characteristics of this actuator will be analyzed, such as the case of dynamic or static tendon slacking, the characteristic stiffness and damping curves, and the role of prestretching for shaping the characteristic curves. With regard to the aim to reduce complexity, the state spaces of the elastic actuator, of the DC motor, and of the joint are introduced together with transformation rules for state transformation between these spaces.

3.2.1 Kinematics and Dynamics Model

For the derivation of the single elastic tendon actuator, it is assumed that the elastic elements integrated in the tendons can be approximated as massless springs. This is a valid assumption if the mass of the springs is small compared to the effective mass of the motor and gearbox inertia and the effective mass of the joint pulley and attached link. For the motors, this is especially true

when using gearboxes with high reduction ratios. The effective mass of the link is normally also higher by at least one order of magnitude.

Only in case of a very lightweight last link without attached further links and without end-effector or load, the spring mass may not be negligible compared to the effective link mass. In this case the spring and link with low joint damping can behave as a two-mass oscillator. Excited at the resonance frequency by minimal motor motions, the spring and link can easily start oscillating. This behavior was observed experimentally with the fourth and last joint of the BioRob-X4 robot arm when using heavy springs. The constellation of two-mass oscillator driven by the motor is highly undesirable and unfavorable for control and should be avoided by choosing a spring with a mass at least a magnitude smaller than the effective link mass.

Figure 3.3 gives an overview of the important parameters and variables of the single joint elastic tendon actuator.

Kinematic Tendon Constraints and Maximum Deflection

The tendons are made of prestretched, high-performance polyethylene and can be regarded as stiff compared to the springs. Because of the kinematic constraint enforced by the constant tendon length, the displacement x_1 of the upper spring equals the negative displacement $-x_2$ of the lower spring

$$x_1 = -R\,q + r\,{}^{\mathrm{e}}\theta \tag{3.1}$$

$$x_2 = R\,q - r\,{}^{\mathrm{e}}\theta = -x_1 \tag{3.2}$$

where R is the radius of the joint pulley, and r the radius of the pulley attached to the motor gearbox shaft. The angular motor position ${}^{\mathrm{e}}\theta$ is given with respect to the elastic actuator input, which is indicated with the index e. The kinematic constraint (3.1) can also be reformulated as

$$x_2 = -x_1 = R\left(q - \frac{r}{R}\,{}^{\mathrm{e}}\theta\right) = R\,(q - {}^{\mathrm{j}}\theta) \tag{3.3}$$

where ${}^{\mathrm{j}}\theta$ represents the virtually reflected motor position with respect to the joint side, which is the joint equilibrium position in the absence of external forces. This also defines the transmission ratio

$$z_{\mathrm{p}} = \frac{{}^{\mathrm{e}}\theta}{{}^{\mathrm{j}}\theta} = \frac{R}{r} \tag{3.4}$$

Using the transmission ratio, the kinematics Equations (3.1) and (3.3) can be expressed either with respect to the joint state space

$$x_1 = -R\,(q - {}^{\mathrm{j}}\theta) = -x_2\,, \tag{3.5}$$

or with respect to the elastic actuator state space

$$x_1 = -r\,({}^{\mathrm{e}}q - {}^{\mathrm{e}}\theta) = -x_2 \tag{3.6}$$

The reflected motor position ${}^{\mathrm{j}}\theta$ therefore equals the joint position q if the elastic actuator is in equilibrium position with $x_i = 0$ and $\tau_{\mathrm{e}} = 0$.

The maximum relative joint deflection with respect to the reflected motor position depends on the maximum spring extension $l_{\max_i}$ and the prestretched spring length l_{p_i}, which limit the spring elongation x_i

$$l_{\max_i} \geq l_{p_i} + x_i \tag{3.7}$$

Using the prestretching spring force F_p instead of the prestretched spring lengths

$$F_p = k_1 \, l_{p_1} = k_2 \, l_{p_2} \tag{3.8}$$

and the kinematic tendon constraints (3.3) yields

$$-\frac{l_{\max_1}}{R} + \frac{F_p}{k_1 R} \leq (q - {}^j\theta) \leq \frac{l_{\max_2}}{R} - \frac{F_p}{k_2 R} \tag{3.9}$$

as constraint for the maximum joint deflection.

Elastic Pulley Torques

The force to displacement characteristic curve of the springs is modeled as ideally viscoelastic. The force F_i exerted by the stretched springs depends on the prestretched length l_{p_i}, the spring stiffness k_i and damping d_i and the elongation x_i

$$F_i = k_i \, (l_{p_i} + x_i) + d_i \, \dot{x}_i \qquad \text{with} \quad i \in \{1, 2\} \tag{3.10}$$

In the equilibrium position with $x_i = 0$ and $\dot{x}_i = 0$ both spring forces equal the prestretching force, yielding the ratio of the prestretching lengths l_{p_i}

$$\frac{l_{p,1}}{l_{p,2}} = \frac{k_2}{k_1} \tag{3.11}$$

Slackening in a tendon occurs if the force is zero or negative ($F_i \leq 0$), whereas tension is maintained for positive forces ($F_i > 0$). The forces F_i can become zero for two reasons. First, because the cables can only transmit pulling spring forces ($F_i > 0$) and no pushing forces ($F_i < 0$), which is referred to in the following as *dynamic tendon slackening*. Second, cable slackening occurs for spring displacement smaller than the prestretched spring length ($x_i < l_{p_i}$), which is referred to as *static tendon slackening*. The resulting torque on the joint produced by the elastic pulley actuation can be expressed using the step function σ

$$\sigma(x) = \begin{cases} 0 & : \quad x < 0 \\ 1 & : \quad x \geq 0 \end{cases} \tag{3.12}$$

as

$$\begin{aligned} {}^j\tau_e = &+ R \, F_1 \, \sigma(F_1) \, \sigma(x_1 + l_{p_1}) \\ &- R \, F_2 \, \sigma(F_2) \, \sigma(x_2 + l_{p_2}) \end{aligned} \tag{3.13}$$

Table 3.1.: State transformations between the elastic actuator state space and the joint state space with transmission ratio $z_\mathrm{p} = \frac{R}{r}$.

State	Actuator Input	Joint
Elastic actuator torque	$\tau_\mathrm{e} = \frac{1}{z_\mathrm{p}}\ {}^\mathrm{j}\tau_\mathrm{e}$	${}^\mathrm{j}\tau_\mathrm{e} = z_\mathrm{p}\ \tau_\mathrm{e}$
Motor position	${}^\mathrm{e}\theta = z_\mathrm{p}\ {}^\mathrm{j}\theta$	${}^\mathrm{j}\theta = \frac{1}{z_\mathrm{p}}\ {}^\mathrm{e}\theta$
Joint position	${}^\mathrm{e}q = z_\mathrm{p}\ q$	$q = \frac{1}{z_\mathrm{p}}\ {}^\mathrm{e}q$

and the elastic pulley torque at the motor side is, using the motor pulley radius r,

$$\begin{aligned}\tau_e = &+ r\ F_1\ \sigma(F_1)\ \sigma(x_1 + l_{\mathrm{p}_1}) \\ &- r\ F_2\ \sigma(F_2)\ \sigma(x_2 + l_{\mathrm{p}_2})\end{aligned} \tag{3.14}$$

As can be seen from Equations (3.13) and (3.14), the kinematic transmission ratio z_p from (3.4) can not only be used to reflect the motor position ${}^\mathrm{e}\theta$ through the elasticity to the joint side

$$\frac{1}{z_\mathrm{p}} = \frac{{}^\mathrm{j}\theta}{{}^\mathrm{e}\theta} = \frac{r}{R}\,, \tag{3.15}$$

but also to reflect the elastic torque τ_e from the motor side to the joint side

$$z_\mathrm{p} = \frac{{}^\mathrm{j}\tau_\mathrm{e}}{\tau_\mathrm{e}} = \frac{R}{r} \tag{3.16}$$

Table 3.2 summerizes the defined state transformations.

Static and Dynamic Tendon Slackening

As described by Equations (3.13) and (3.14), tendon slackening can be caused by the displacement $x_i + l_{p_i} < 0$ as static slackening, or by the spring force $F_i < 0$ as dynamic slackening. Figure 3.7 lists the possible tendon slackening states of a single joint elastic tendon actuator.

Static slackening in the lower tendon occurs if the elongation of the spring in that tendon becomes negative. This yields the constraint for the angular displacement of the joint position q with respect to the reflected motor position ${}^\mathrm{j}\theta$

$$l_{\mathrm{p}_2} + x_2 \ \leq\ 0 \quad \Rightarrow \quad (q - {}^\mathrm{j}\theta) \ \leq\ -\frac{F_\mathrm{p}}{Rk_2} \tag{3.17}$$

The constraint for the upper side is calculated respectively

$$l_{\mathrm{p}_1} + x_1 \ \leq\ 0 \quad \Rightarrow \quad (q - {}^\mathrm{j}\theta) \ \geq\ \frac{F_\mathrm{p}}{Rk_1} \tag{3.18}$$

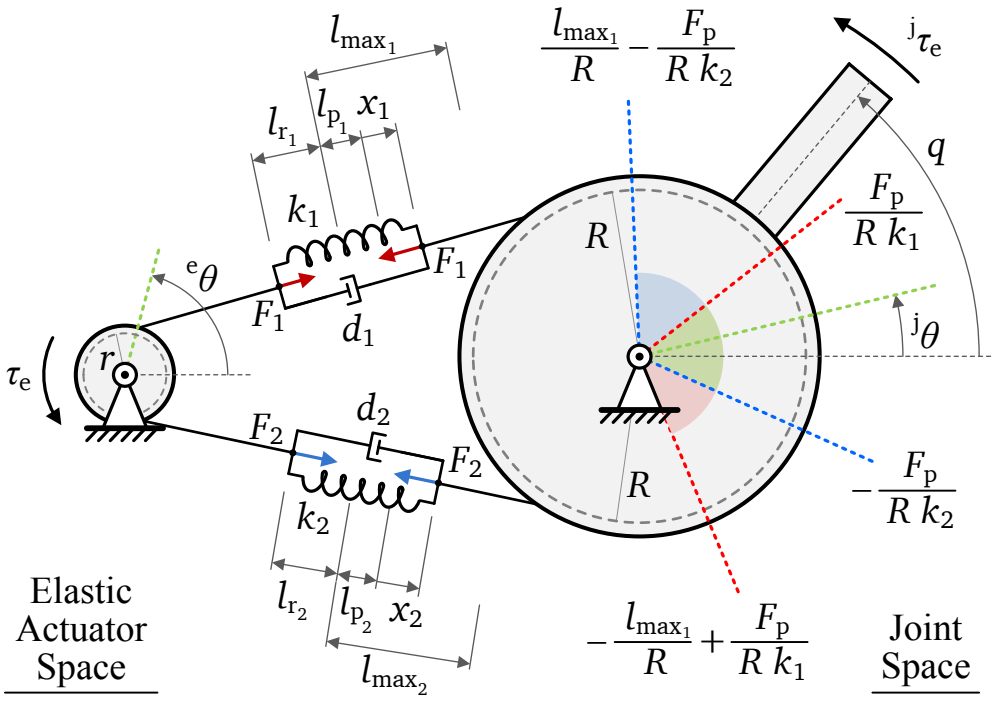

Figure 3.4.: Model of the elastic tendon actuator (Figure 3.3) complemented by the tendon slackening areas on the joint side. The motor position ${}^{j}\theta$ with respect to the joint side marks the equilibrium position of the joint position q. The colors of the boundaries and areas refer to the dependency on the upper (red), lower (blue), or both (green) spring parameters. The joint angle area without static tendon slackening is marked by the green arc area, whereas the blue arc marks static slackening in the lower spring, and the red arc slackening in the upper spring.

Static tension in both tendons is therefore maintained for the angular joint displacement range

$$-\frac{F_p}{R\,k_2} \;\leq\; (q - {}^{j}\theta) \;\leq\; \frac{F_p}{R\,k_1} \tag{3.19}$$

Dynamic slackening occurs for pushing forces $F_i < 0$. This can happen in case of high relative velocities between joint and motor causing damping forces in the respective spring that cancel out the elastic forces. In the lower tendon this is the case for

$$F_p + k_2\,x_2 + d_2\dot{x}_2 \;\leq\; 0 \quad\Rightarrow\quad \dot{q} - {}^{j}\dot{\theta} \;\leq\; -\frac{F_p}{R\,d_2} - \frac{k_2}{d_2}(q - {}^{j}\theta) \tag{3.20}$$

and in the upper tendon this is the case for

$$F_p + k_1\,x_1 + d_1\dot{x}_1 \;\leq\; 0 \quad\Rightarrow\quad \dot{q} - {}^{j}\dot{\theta} \;\geq\; \frac{F_p}{R\,d_1} - \frac{k_1}{d_1}(q - {}^{j}\theta) \tag{3.21}$$

Dynamic tension on both tendons is therefore maintained for

$$-\frac{F_p}{R\,d_2} - \frac{k_2}{d_2}(q - {}^{j}\theta) \;\leq\; (\dot{q} - {}^{j}\dot{\theta}) \;\leq\; \frac{F_p}{R\,d_1} - \frac{k_1}{d_1}(q - {}^{j}\theta) \tag{3.22}$$

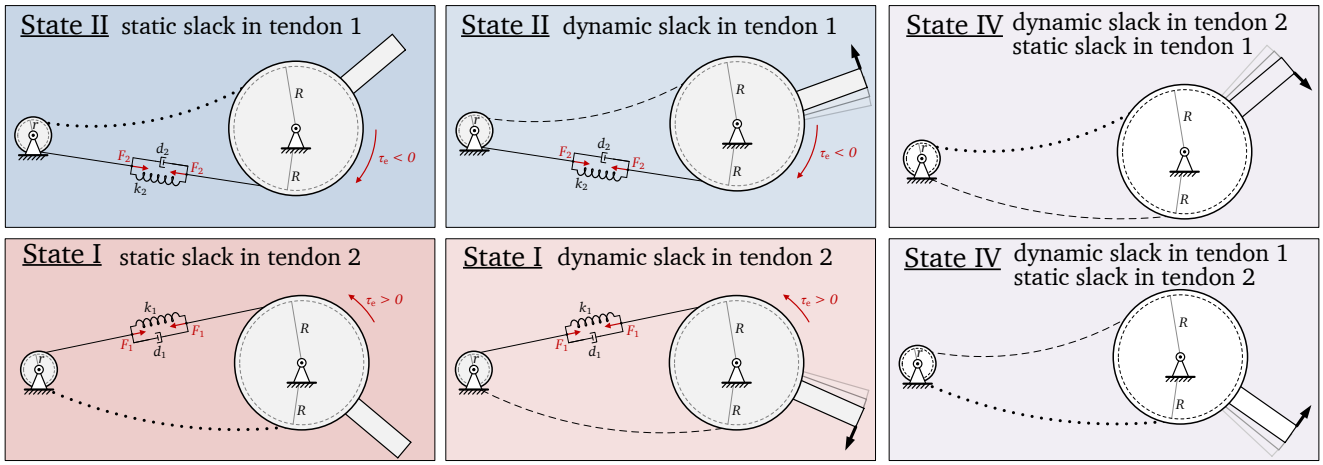

Figure 3.5.: Definition of dynamic and static tendon slackening states of the elastic tendon actuator. Static slackening in the tendons (indicated by dashed lines) occurs in case of large joint deflections and dynamic slackening (indicated by dotted lines) occurs at high velocities with dominating damping forces. State I describes dynamic or static slackening in the lower tendon (with index 2), State II dynamic or static slackening in the upper tendon (with index 1), State III is the normal operation mode without slackening (not displayed, cf. Figure 3.3), State IV combines static slackening in one of the tendons and dynamic slackening in the other tendon.

Table 3.2.: Parameter transformations between the elastic actuator state space and the joint state space.

State Space	Actuator Input	Joint
Stiffness	${}^{\mathrm{e}}k = \frac{1}{z_{\mathrm{p}}^2}\,{}^{\mathrm{j}}k$	${}^{\mathrm{j}}k = z_{\mathrm{p}}^2\,{}^{\mathrm{e}}k$
Damping	${}^{\mathrm{e}}d = \frac{1}{z_{\mathrm{p}}^2}\,{}^{\mathrm{j}}d$	${}^{\mathrm{j}}d = z_{\mathrm{p}}^2\,{}^{\mathrm{e}}d$

The resulting areas are displayed in Figure 3.6. The static tension range from Equation (3.19) only depends on the relative joint deflection $(q - {}^{\mathrm{j}}\theta)$ and is marked by vertical boundaries. This is also the case for the maximum deflection from Equation (3.9). The dynamic tension range is from Equation (3.22) is defined by two lines with slope $\frac{k_i}{d_i}$. The size of the areas depends on the prestretching force F_{p}. The shifting direction of the area boundaries with increasing prestretching force are indicated with arrows in Figure 3.6.

Characteristic Stiffness and Damping Curves

In this section the output torque function of the actuator states defined in Figure 3.7 is derived.

State I With dynamic or static slackening in the lower tendon (index 2), the elastic torque is generated only by the taut upper tendon (index 1):

$$ {}^{\mathrm{j}}\tau_{\mathrm{e_I}} = R\,(F_{\mathrm{p}} + k_1\,x_1 + d_1\,\dot{x}_1) \tag{3.23}$$

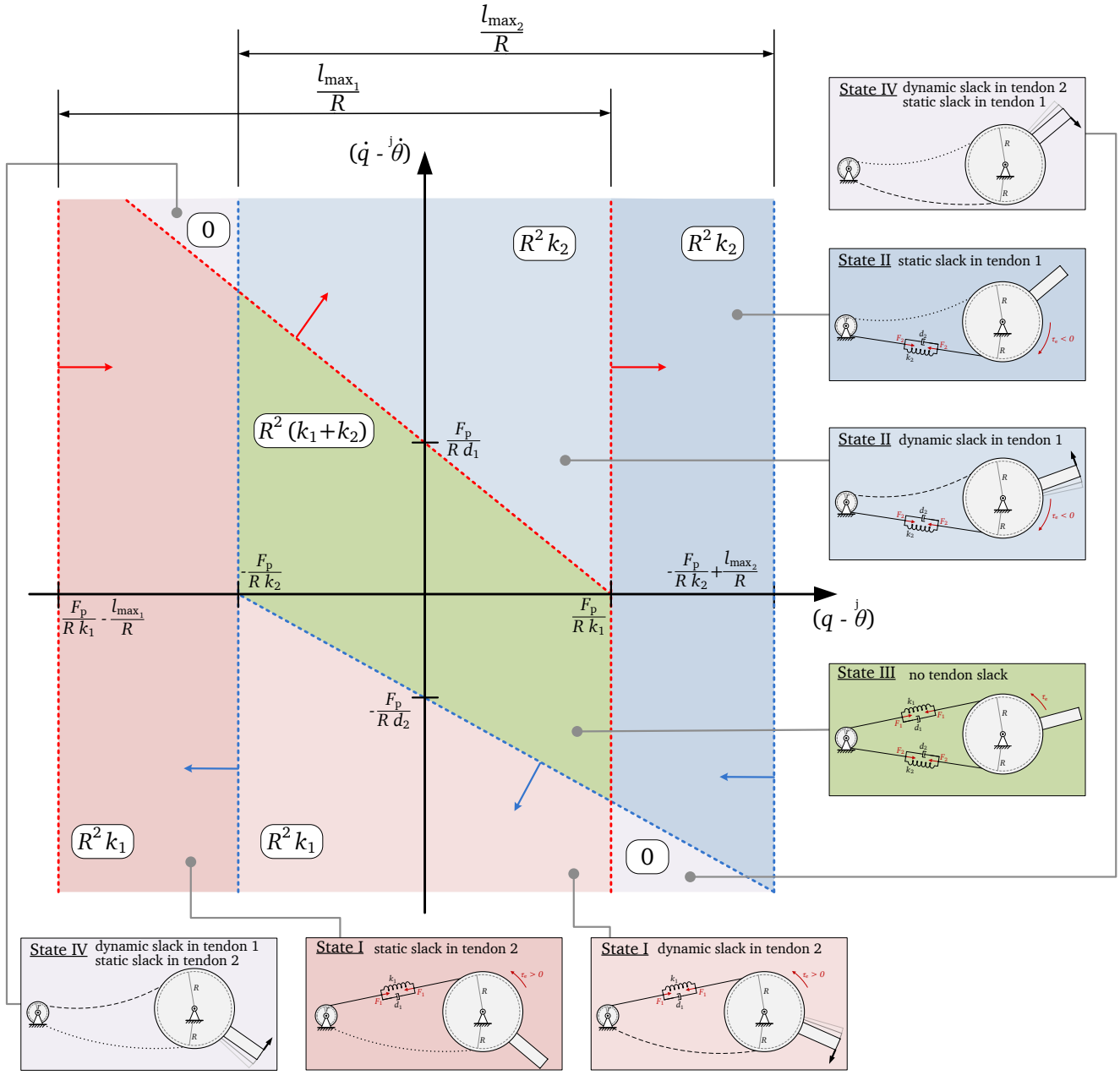

Figure 3.6.: Phase diagram of the joint displacement with respect to the reflected motor position of the elastic tendon actuator incorporating all constraints and boundaries. The arrows indicate the shifting direction of the boundaries when increasing the pre-stretching force F_p. The white labels indicate the stiffness of the respective areas. Red areas and lines depend on the parameters of the spring on the upper side (index 1), blue areas and lines depend on the parameters of the spring on the lower side (index 2). The pictures of State I to IV indicate the tendon state; dotted lines indicate static slackening, dashed lines indicate dynamic slackening.

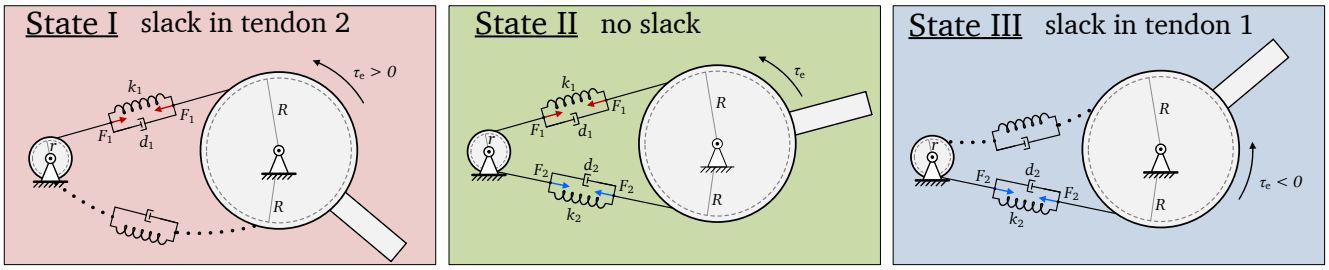

Figure 3.7.: Definition of static tendon slack states of the elastic tendon actuator. Static slack in the tendons (indicated by dotted lines) occurs in case of large joint deflections. State I describes static slack in the lower tendon (index 2), State II the normal operation mode without slack, and State III static slack in the upper tendon (index 1).

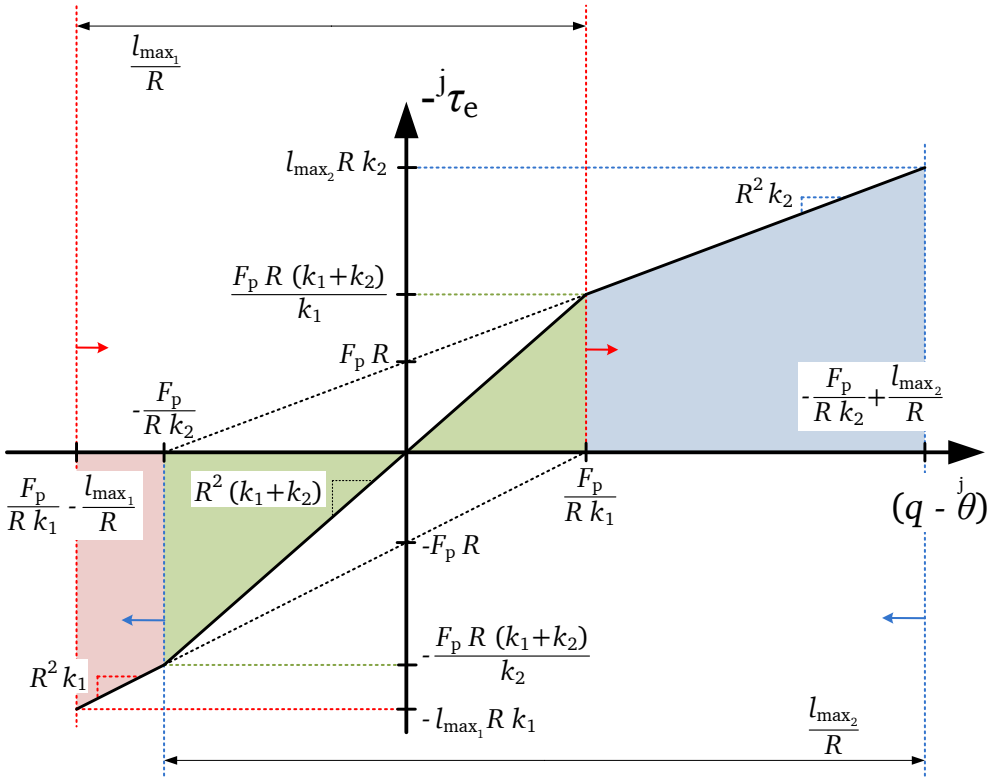

Figure 3.8.: Negative actuator output torque function $-^{j}\tau_e$ of the single joint elastic tendon actuator with respect to the joint side. The shifting directions of the area boundaries for an increasing prestretching force F_p are indicated with arrows. The colors of the torque function areas and boundaries refer to the dependency on the parameters of the upper (red), lower (blue), or both (green) spring parameters. The area with slack in the upper spring (index 1) is marked in red, as well as the boundaries depending on parameters of the upper spring. Respectively, the area and boundaries that are marked in blue depend on parameters of the lower spring (index 2). The plot shows an example for asymmetric configuration with a stiffer spring on the upper side $k_1 = 1.33\, k_2$ with maximum deflection $l_{\max_1} = 0.67\, l_{\max_2}$.

$$= R F_{\mathrm{p}} - k_1 R^2 \left(q - {}^{\mathrm{j}}\theta\right) - d_1 R^2 \left(\dot{q} - {}^{\mathrm{j}}\dot{\theta}\right) \tag{3.24}$$

The output stiffness and damping can be obtained by derivation with regard to the joint deflection and its velocity

$${}^{\mathrm{j}}k_{\mathrm{e_I}} = -\frac{\partial \tau_{\mathrm{e_I}}}{\partial (q - {}^{j}\theta)} = R^2 k_1 \quad , \quad {}^{\mathrm{j}}d_{\mathrm{e_I}} = -\frac{\partial \tau_{\mathrm{e_I}}}{\partial (\dot{q} - {}^{j}\dot{\theta})} = R^2 d_1 \tag{3.25}$$

State II Equivalent to State I, with transposed indices: dynamic or static slackening in the upper tendon (index 1), the elastic torque is generated only by the taut lower tendon (index 2):

$${}^{\mathrm{j}}\tau_{\mathrm{e_{II}}} = -R \left(F_{\mathrm{p}} + k_2 x_2 + d_2 \dot{x}_2\right) \tag{3.26}$$

$$= -R F_{\mathrm{p}} - k_2 R^2 \left(q - {}^{\mathrm{j}}\theta\right) - d_2 R^2 \left(\dot{q} - {}^{\mathrm{j}}\dot{\theta}\right) \tag{3.27}$$

with stiffness and damping

$${}^{\mathrm{j}}k_{\mathrm{e_{II}}} = R^2 k_2 \quad , \quad {}^{\mathrm{j}}d_{\mathrm{e_{II}}} = R^2 d_2 \tag{3.28}$$

State III Without slackening, both tendons contribute to the elastic torque:

$${}^{\mathrm{j}}\tau_{\mathrm{e_{III}}} = -R^2 \left(k_1 + k_2\right) \left(q - {}^{\mathrm{j}}\theta\right) - R^2 \left(d_1 + d_2\right) \left(\dot{q} - {}^{\mathrm{j}}\dot{\theta}\right) \tag{3.29}$$

with stiffness and damping

$${}^{\mathrm{j}}k_{\mathrm{e_{III}}} = R^2 \left(k_1 + k_2\right) \quad , \quad {}^{\mathrm{j}}d_{\mathrm{e_{III}}} = R^2 \left(d_1 + d_2\right) \tag{3.30}$$

State IV With slackening in both cables, the elastic torque is zero:

$${}^{\mathrm{j}}\tau_{\mathrm{e_{IV}}} = 0 \tag{3.31}$$

This yields distinct stiffness and damping values for each of the four states. The phase diagram in Figure 3.6 indicates the areas of all states. The stiffnesses are indicated in the respective areas with white text labels. The resulting steady state output characteristic stiffness curve is plotted in Figure 3.8.

The equivalent derivation of the actuator input stiffness and damping values yields the same results, except that the motor pulley radius r is used instead of the joint pulley radius R. Therefore, the stiffness and damping parameters can be reflected from the actuator input to the joint side using the square of the transmission ratio z_{p}^2, as listed in Table 3.2.

3.2.2 Design Guidelines

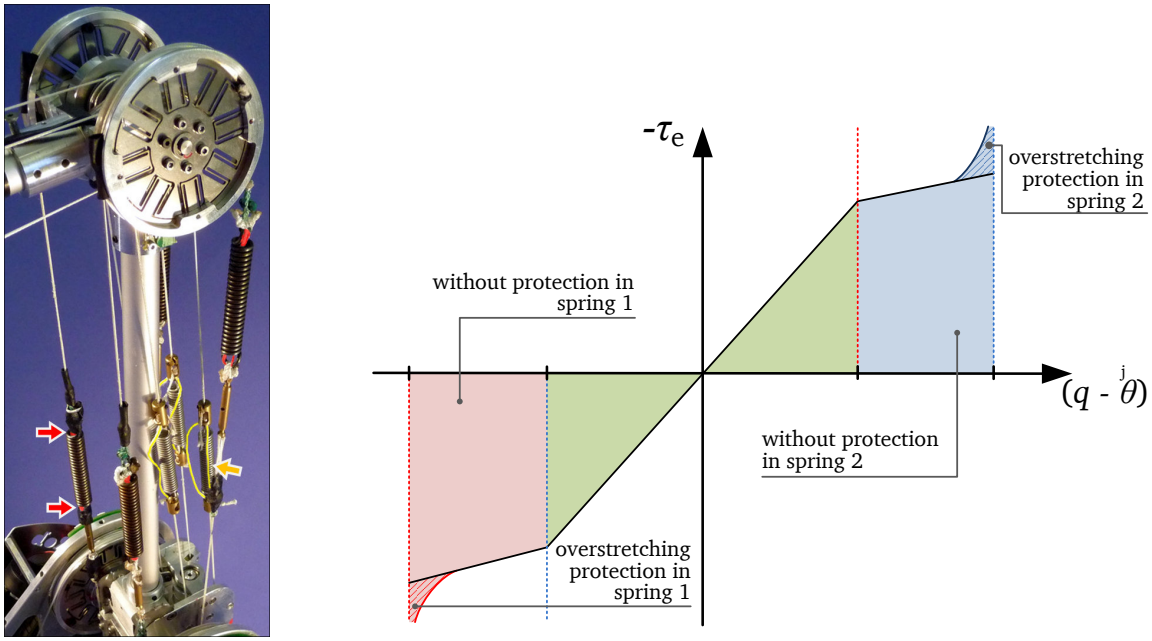

Figure 3.9.: Symmetric spring configuration with protection against overstretching and progressive curve. Possible hardware implementations for the protective elements are displayed in the left picture. Protective strings guided within the springs are marked in red, strings on the outside of the springs are marked in yellow.

Guidelines for Choosing Spring Stiffnesses and Prestretching Force

If the stiffnesses of the upper and lower spring differ, an asymmetric stiffness curve configuration results. An example for a stiffer upper spring is shown in Figure 3.8. The asymmetric stiffness curve as in Figure 3.10 exhibits a larger high stiffness area for negative joint deflection angles compared to a symmetric configuration, as shown in Figure 3.11. In case the direction of gravitational forces is constant, the asymmetric spring configuration can be very useful to compensate for the shift in the joint equilibrium position caused by gravity.

The high stiffness area with both springs stretched, preventing static tendon slackening, can be enlarged by increasing the prestretching force F_p. Figure 3.8 displays the boundaries of the areas with combined and single stiffness. The arrows indicate the shifting direction of the boundaries in case F_p is increased. As can be seen from that figure, enlarging the high stiffness area by increasing the prestretching force also reduces the maximum joint deflection. Figures 3.10 and 3.11 show the effect of the prestretching force on the actuator output torque and on the maximum joint deflection.

The maximum allowed prestretching force is defined by the product of the maximum allowed elongation of the springs and the spring stiffnesses

$$F_{\mathrm{p,max}} = \min_{i=\{1,2\}} \left(l_{\mathrm{max}_i} \, k_i \right), \tag{3.32}$$

where the spring with the lowest value defines the upper limit of the prestretching force. For this prestretching force, the area of joint deflection as given by (3.9) is reduced to zero in at least in one direction.

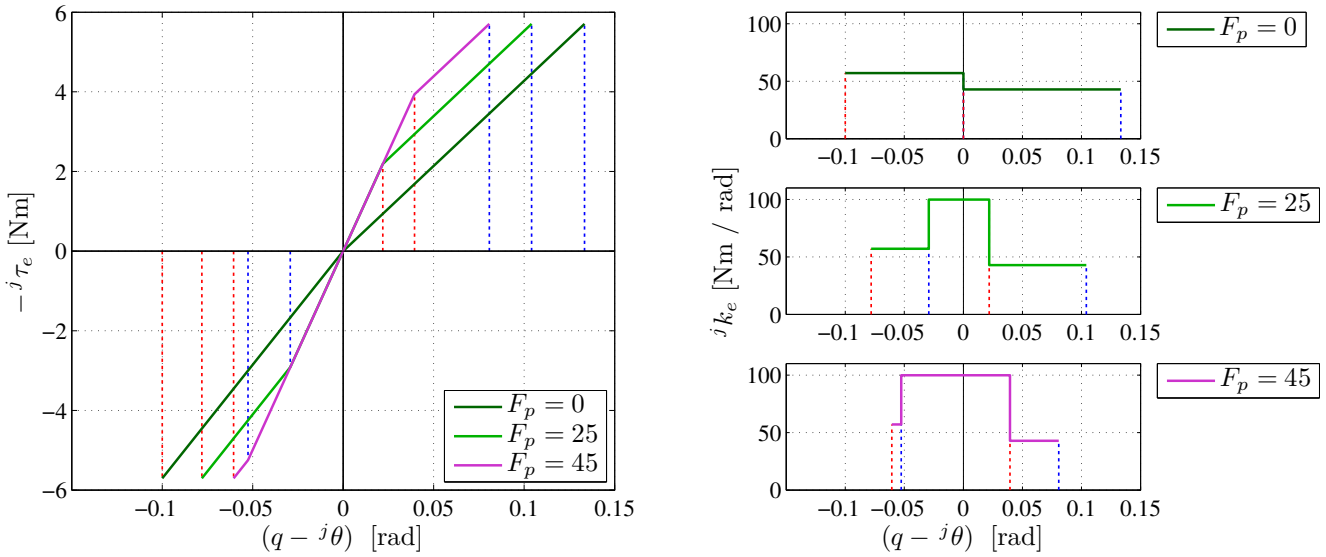

Figure 3.10.: Effect of prestretching on the characteristic stiffness curve with respect to the joint side. Example for asymmetric configuration with $k_1 = 22.820\,\mathrm{kN/m}$, $k_2 = 0.75\ k_1$, $l_{\mathrm{max}_1} = 5\,\mathrm{mm}$, $l_{\mathrm{max}_2} = 1.33\ l_{\mathrm{max}_1}$, $R = 5\,\mathrm{cm}$. The maximum torque remains constant, whereas the maximum joint deflection decreases for increasing pretension force F_p.

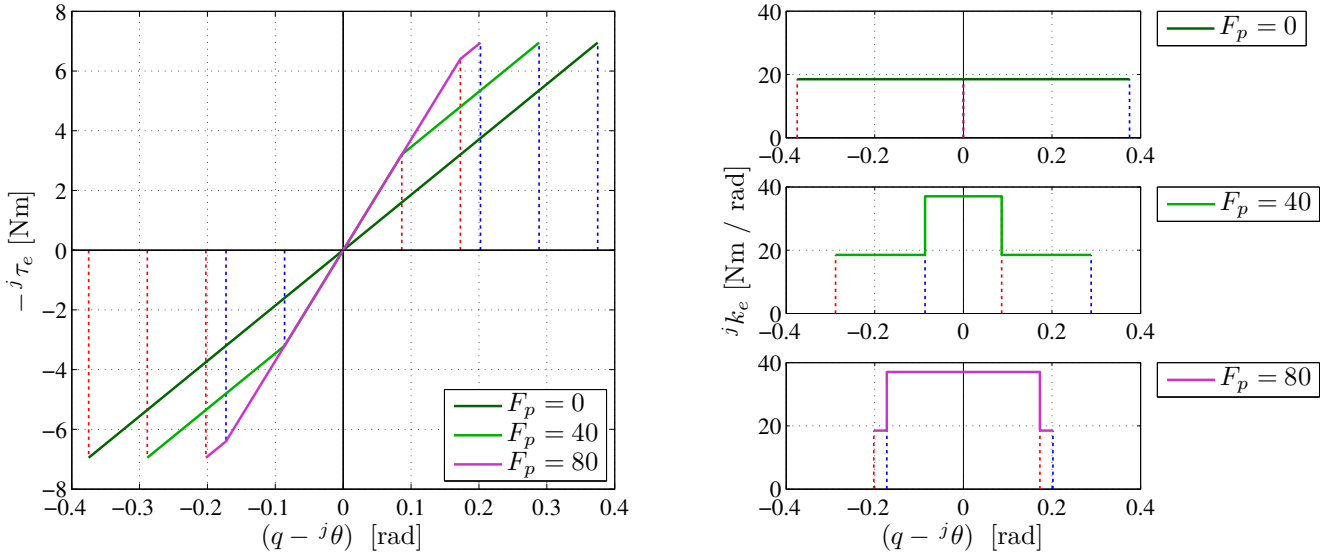

Figure 3.11.: Effect of prestretching on the characteristic stiffness curve with respect to the joint side. Example for symmetric configuration with $k_i = 11.580\,\mathrm{kN/m}$, $l_{\mathrm{max}_i} = 15\,\mathrm{mm}$, $R = 4\,\mathrm{cm}$. The maximum torque remains constant, whereas the maximum joint deflection decreases for increasing pretension force F_p.

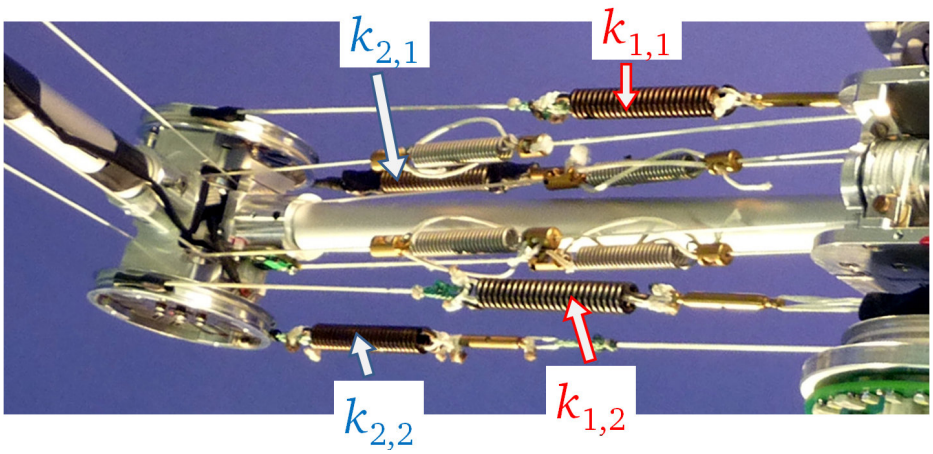

Figure 3.12.: BioRob-X4 actuation of third joint with two tendons in parallel. For the actuator model, only the combined stiffnesses $k_i = k_{i,1} + k_{i,2}$ are used, marked by the same color in the picture.

A reasonable goal for setting the prestretched force could be maximizing the high stiffness area. With (3.9), maximizing the high stiffness area in direction of negative deflections yields

$$\frac{F_\mathrm{p}}{R\,k_1} - \frac{l_{\max_1}}{R} = -\frac{F_\mathrm{p}}{R\,k_2}\,, \tag{3.33}$$

and for positive deflections

$$-\frac{F_\mathrm{p}}{R\,k_2} + \frac{l_{\max_2}}{R} = \frac{F_\mathrm{p}}{R\,k_1}\,, \tag{3.34}$$

which yields

$$F_\mathrm{p} = \min_{i=\{1,2\}} \left(l_{\max_i} \left(\frac{1}{k_1} + \frac{1}{k_2} \right)^{-1} \right) \tag{3.35}$$

The result is an almost linear characteristic joint stiffness curve for most of the deflection range, which can be beneficial for controller design. For springs with equal maximum stretching length l_max, the maximum pretension force can be therefore chosen as

$$F_\mathrm{p} = l_\mathrm{max} \left(\frac{1}{k_1} + \frac{1}{k_2} \right)^{-1}\,, \tag{3.36}$$

which maximizes the high stiffness area in both positive and negative direction of deflection.

When increasing the pretension force, it should always be ensured that the mechanical joint construction can bear the given prestretching forces as well as dynamical and external forces.

Guidelines for Increasing the Maximum Output Torque

The maximum output torque can be increased by using springs with a higher maximum force $F_{\max_i}$ and an appropriate maximum deflection $l_{\max_i}$

$$F_{\max_i} = l_{\max_i}\, k_i \tag{3.37}$$

It must be noted, however, that heavier springs increase the danger of undesired oscillations of the spring mass.

If no stiffer spring with the desired properties is available, parallel tendons with equal springs can be used. In this case, the resulting spring stiffness is the sum of all spring stiffnesses used in parallel. Figure 3.12 displays the use of two parallel tendons for joint three of the BioRob-X4 arm, resulting in the combined stiffnesses

$$k_1 = k_{1,1} + k_{1,2} \tag{3.38}$$
$$k_2 = k_{2,1} + k_{2,2} \tag{3.39}$$

3.2.3 Analysis of the BioRob-X4 Elastic Tendon Actuator Configuration

The characteristic stiffness curve of joint 3 is displayed in Figure 3.13. The springs are preloaded with 40 N. As can be seen from Figure 3.12, two cable pairs are used leading to a combined prestretching force of $F_{\mathrm{p}} = 80\,\mathrm{N}$. The upper and lower spring therefore generate a combined radial bearing load of 160 N in the actuated joint.

The damping coefficients of the springs are not given in the data sheets. By assuming viscously damped springs with load mass m, viscous damping d, and stiffness k, the internal dynamics are given as:

$$m\,\ddot{x} + d\,\dot{x} + k\,x = 0\,, \tag{3.40}$$

or with damping ratio D, and undamped natural frequency ω_0:

$$\ddot{x} + 2D\,\omega_0\,\dot{x} + \omega_0^2\,x = 0 \tag{3.41}$$

with

$$d = 2D\,\sqrt{m\,k} \qquad \text{and} \qquad \omega_0 = \sqrt{\frac{k}{m}} \tag{3.42}$$

The logarithmic damping decrement Λ defined as

$$\Lambda = \frac{1}{n}\ln\left|\frac{q(t_k)}{q(t_k + nT)}\right| \tag{3.43}$$

is related to the damping ratio D as follows [13]

$$\Lambda = \frac{2\pi\,D}{\sqrt{1-D^2}} \tag{3.44}$$

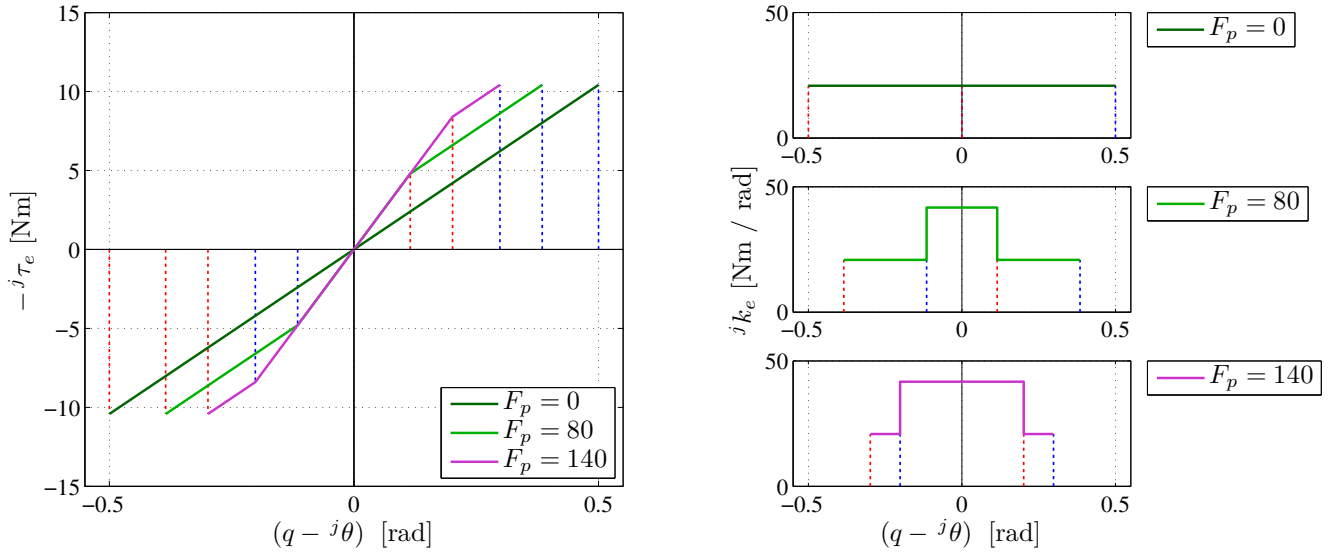

Figure 3.13.: Characteristic stiffness curve of BioRob-X4 joint 3 with two parallel elastic tendon actuators with spring stiffness $k_i = 11.580\,\mathrm{kN/m}$, maximum spring elongation $l_{\mathrm{max}_i} = 15\,\mathrm{mm}$, and joint pulley radius $R = 3\,\mathrm{cm}$. The resulting stiffness curves for various spring preloading forces F_p are shown.

If a measurement value or estimation for Λ is given, the damping ratio can be therefore calculated as

$$D = \frac{\Lambda}{\sqrt{\Lambda^2 + 4\pi^2}} \tag{3.45}$$

and the viscous damping as

$$d = 2D\sqrt{m\,k} = \frac{2\Lambda\sqrt{m\,k}}{\sqrt{\Lambda^2 + 4\pi^2}} \tag{3.46}$$

For a load mass of $m = 1\,\mathrm{kg}$ and spring stiffness $k = 11.580\,\mathrm{kN/m}$, an amplitude decay rate of 1% per oscillation is estimated. With the logarithmic damping decrement

$$\Lambda = \ln\Big(\frac{1}{0.99}\Big) = 0.0101\,, \tag{3.47}$$

the resulting viscous damping in each spring is

$$d_{i,1} = d_{i,2} = 0.344\,\mathrm{Ns/m}\,, \tag{3.48}$$

resulting in an effective spring damping of

$$d_i = d_{i,1} + d_{i,2} = 0.6885\,\mathrm{Ns/m} \tag{3.49}$$

The parameters of the actuator in the third joint actuator of the BioRob-X4 arm are given in Figure 3.15. With these parameters, the boundaries of the phase diagram for this actuator can be calculated. Static slackening occurs at a joint deflection of

$$\pm(q - {}^{\mathrm{j}}\theta) = \frac{F_\mathrm{p}}{R\,k_i} = 0.1151\,\mathrm{rad} = 6.60^\circ\,, \tag{3.50}$$

and the maximum joint deflection is

$$\pm(q - {}^{\mathrm{j}}\theta) = -\frac{F_{\mathrm{p}}}{R\,k_i} + \frac{l_{\max_i}}{R} = 0.385\,\mathrm{rad} = 22.05^\circ\,, \tag{3.51}$$

The dynamic slackening boundary value at the joint equilibrium position $q = {}^{\mathrm{j}}\theta$ yields

$$\pm(\dot{q} - {}^{\mathrm{j}}\dot{\theta}) = \frac{F_{\mathrm{p}}}{R\,d_i} = 3.87 \cdot 10^3\,{}^{\mathrm{rad}}/_{\mathrm{s}}\,, \tag{3.52}$$

with a slope of

$$-\frac{k_1}{d_1} = -3.37 \cdot 10^4\,{}^{1}/_{\mathrm{s}}\,, \tag{3.53}$$

indicating that dynamic slackening is only likely to occur in the vicinity of the boundary of static slackening (cf. Figure 3.6). The dynamic slackening state can therefore be neglected when modeling and simulating the robot arm with the given parameters. For this case, the phase diagram is reduced to the characteristic stiffness (Figure 3.8) and damping curves.

The angular stiffness and damping parameters in the state without slackening (State III) are

$$k_{\mathrm{e_{III}}} = R^2\,(k_1 + k_2) = 41.69\,{}^{\mathrm{Nm}}/_{\mathrm{rad}} \tag{3.54}$$

$$d_{\mathrm{e_{III}}} = R^2\,(d_1 + d_2) = 1.24\,{}^{\mathrm{mNms}}/_{\mathrm{rad}} \tag{3.55}$$

and in case of static slackening (State I and II)

$$k_{\mathrm{e_I}} = R^2\,k_1 = k_{\mathrm{e_{II}}} = R^2\,k_2 = 20.8\,{}^{\mathrm{Nm}}/_{\mathrm{rad}} \tag{3.56}$$

$$d_{\mathrm{e_I}} = R^2\,d_1 = d_{\mathrm{e_{II}}} = R^2\,d_2 = 0.620\,{}^{\mathrm{mNms}}/_{\mathrm{rad}} \tag{3.57}$$

The resulting characteristic torque and stiffness curves of the BioRob-X4 elastic tendon actuator for the third joint are displayed in Figure 3.13.

3.2.4 DC Motor Model

Motors can be controlled to generate the desired torque $\boldsymbol{\tau}_{\mathrm{m,d}}$, which can be seen as the input of the mechanical system. Many simulation approaches only use a reduced motor model without the electrical subsystem by assuming that a desired torque can be produced without delay, that is, the motor is regarded as an ideal torque source. Or the controlled electrical subsystem is modeled as a first order linear low pass system with a time constant of a few milliseconds.

Instead of using the simple torque source model, a complete model of the electrical motor dynamics allows for the examination of the motor currents and voltages, which are both limited in reality. In simulation, these limitations can be taken into account with the electrical motor model. The motors used in the BioRob robot arm are direct current (DC) motors. The electrical dynamics can be described as:

$$U_{\mathrm{a}} = U_{\mathrm{R}} + U_{\mathrm{L}} + U_{\mathrm{ind}} \tag{3.58}$$

$$= R_{\mathrm{a}}\,I_{\mathrm{a}} + L_{\mathrm{a}}\,\frac{\mathrm{d}I_{\mathrm{a}}}{\mathrm{d}t} + k_{\mathrm{v}}\,\dot{\theta} \tag{3.59}$$

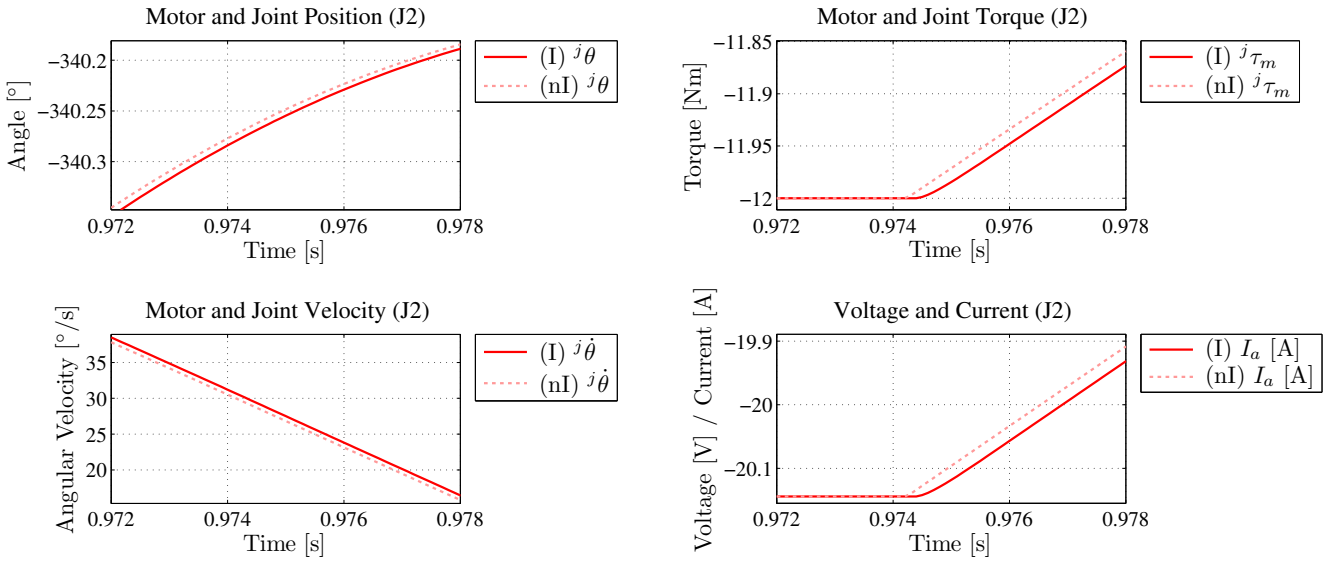

Figure 3.14.: Comparison of the states of the second joint of a four DOF robot arm with stiff actuation with (I) and without inductance (nI). The motors in this simulation model are the DC motors used in the BioRob-X4 hardware. The delay introduced by the modeled inductance is about 0.2 to 0.4 ms. Also, a slight low pass filtering of the anker current I_a (bottom right) and thereby also of the motor torque τ_m (top right) is obtained.

with armature resistance R_a and inductance L_a, torque constant k_t, and speed constant k_v and generated motor torque τ_m, which drives the rotor.

Figure 3.14 compares the output of a simulation model with and without inductance. The delay introduced by the inductance is lower than 0.4 ms. For these motors the time constant of the armature inductance can therefore be neglected compared to the mechanical time constant of the motor, which is about 5 to 10 ms. The generated torque is proportional to the motor current

$$\tau_\mathrm{m} = k_\mathrm{t}\, I_\mathrm{a} \tag{3.60}$$

This motor torque drives the rotor with inertia I_m and viscous friction d_m. The mechanical dynamics of a freely rotating motor is

$$I_\mathrm{m}\,\ddot{\theta} + d_\mathrm{m}\,\dot{\theta} = \tau_\mathrm{m} \tag{3.61}$$

When connected to the robot, the mechanical motor model has to be modeled together with the robot arm mechanics to receive the mechanical dynamics equations of the coupled system. The full MBS dynamics model is described in Section 3.4.

For use as actuators for revolute joints in robotic systems, electrical motors usually require gearboxes to achieve the desired torques. Gearboxes can be modeled with a transmission ratio z_g reducing the speed $\dot{\theta}$ of the motor to the slower gearbox output angular velocity $^{g}\theta$

$$^{g}\theta = \frac{1}{n_\mathrm{g}}\dot{\theta} \qquad \text{with} \qquad |n_\mathrm{g}| > 1 \tag{3.62}$$

Assuming conservation of power for an ideal gearbox yields an increase of the motor torque τ_m by factor z_g at the gearbox output shaft

$$^{\mathrm{g}}\tau_\mathrm{m} = z_\mathrm{g}\,\tau_\mathrm{m} \tag{3.63}$$

In reality the quotient of the gearbox output and input power, the gearbox efficiency, is lower than one. These losses can be modeled by introducing additional frictional and inertial terms. With the inverse model of the motor dynamics

$$U_\mathrm{a} = \frac{R_\mathrm{a}}{k_\mathrm{t}}\,\tau_\mathrm{m} + \frac{L_\mathrm{a}}{k_\mathrm{t}}\,\frac{\mathrm{d}\tau_\mathrm{m}}{\mathrm{d}t} + k_\mathrm{v}\,\dot{\theta} \tag{3.64}$$

and the assumption that the inductance can be neglected, the inverse motor model for an external load torque $^{\mathrm{m}}\boldsymbol{\tau}$ with respect to the motor axis is given by

$$U_\mathrm{a} = \frac{R_\mathrm{a}\,I_\mathrm{m}}{k_\mathrm{t}}\,\ddot{\theta} + \Big(\frac{R_\mathrm{a}\,d_\mathrm{m}}{k_\mathrm{t}} + k_\mathrm{v}\Big)\,\dot{\theta} - \frac{R_\mathrm{a}}{k_\mathrm{t}}\,^{\mathrm{m}}\boldsymbol{\tau}\ , \tag{3.65}$$

which will be used for the tracking controller.

3.2.5 Reflected Motor Variables Model

The motor positions θ_i and torques τ_i of the N actuators can be stacked into a single motor position state vector $\boldsymbol{\theta}$:

$$\boldsymbol{\theta} = \begin{pmatrix} \theta_1 \\ \vdots \\ \theta_N \end{pmatrix} \quad , \quad \boldsymbol{\tau}_\mathrm{m} = \begin{pmatrix} \tau_1 \\ \vdots \\ \tau_N \end{pmatrix} \tag{3.66}$$

The motor position $\boldsymbol{\theta}$ and velocity $\dot{\boldsymbol{\theta}}$ vector can be reflected to the elastic actuator input by defining a diagonal $[N \times N]$ Jacobian $\boldsymbol{J}_\mathrm{g}$ consisting of the combined gearbox and bevel gears transmission ratios z_{g_i}:

$$^{\mathrm{e}}\boldsymbol{\theta} = \boldsymbol{J}_\mathrm{g}\,\boldsymbol{\theta} = \mathrm{diag}\Big(\tfrac{1}{n_{\mathrm{g}_1}} \quad \cdots \quad \tfrac{1}{n_{\mathrm{g}_N}}\Big) \qquad \text{with} \quad |n_{\mathrm{g}_i}| > 1 \ \ \boldsymbol{\theta} \tag{3.67}$$

With the principle of virtual work

$$\dot{\boldsymbol{\theta}}^\top\,\boldsymbol{\tau}_\mathrm{m} \;=\; {}^{\mathrm{e}}\dot{\boldsymbol{\theta}}^\top\,{}^{\mathrm{e}}\boldsymbol{\tau}_\mathrm{m} \;=\; (\boldsymbol{J}_\mathrm{g}\,\dot{\boldsymbol{\theta}})^\top\,{}^{\mathrm{e}}\boldsymbol{\tau}_\mathrm{m} \;=\; \dot{\boldsymbol{\theta}}^\top\,\boldsymbol{J}_\mathrm{g}^\top\,{}^{\mathrm{e}}\boldsymbol{\tau}_\mathrm{m} \tag{3.68}$$

the reflected motor torque with respect to the gearbox output shaft is obtained

$$\boldsymbol{\tau}_\mathrm{m} = \boldsymbol{J}_\mathrm{g}{}^\top\,{}^{\mathrm{e}}\boldsymbol{\tau}_\mathrm{m} \tag{3.69}$$

With these reflected states the mechanical motor dynamics equation formulated in matrix form

$$\boldsymbol{I}_\mathrm{m}\,\ddot{\boldsymbol{\theta}} + \boldsymbol{D}_\mathrm{m}\,\dot{\boldsymbol{\theta}} = \boldsymbol{\tau}_\mathrm{m} \tag{3.70}$$

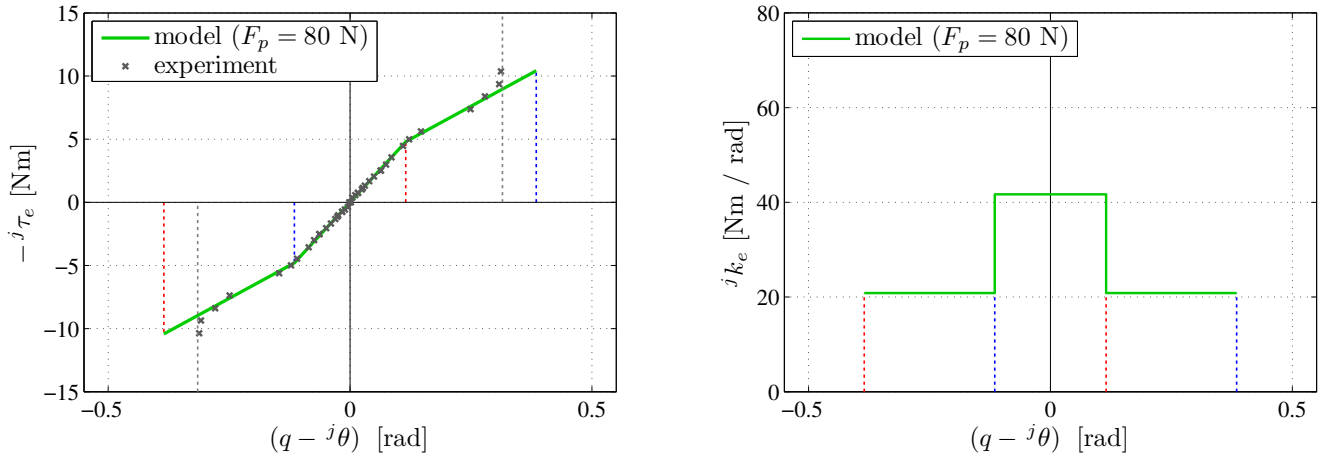

Figure 3.15.: Measured characteristic stiffness curve of the third joint of a BioRob-X4 arm with two parallel elastic tendon actuators with spring stiffnesses $k_{i,j} = 11.580\,\mathrm{kN/m}$, maximum spring elongation $l_{\mathrm{max}_i} = 15\,\mathrm{mm}$, and joint pulley radius $R = 3\,\mathrm{cm}$.

with the diagonal matrices rotor inertia $\boldsymbol{I}_\mathrm{m}$ and viscous friction $\boldsymbol{D}_\mathrm{m}$

$$\boldsymbol{I}_\mathrm{m} = \mathrm{diag}\big(I_{m_1}, \ldots, I_{m_N}\big) \tag{3.71}$$

$$\boldsymbol{D}_\mathrm{m} = \mathrm{diag}\big(d_{m_1}, \ldots, d_{m_N}\big)\,, \tag{3.72}$$

can be reflected to the gearbox output shaft

$$\boldsymbol{I}_\mathrm{m}\boldsymbol{J}_\mathrm{g}^{-1}\,{}^{\mathrm{e}}\ddot{\boldsymbol{\theta}} + \boldsymbol{D}_\mathrm{m}\boldsymbol{J}_\mathrm{g}^{-1}\,{}^{\mathrm{e}}\dot{\boldsymbol{\theta}} = \boldsymbol{J}_\mathrm{g}^{\top}\,{}^{\mathrm{e}}\boldsymbol{\tau}_\mathrm{m} \tag{3.73}$$

$$\Rightarrow \quad (\boldsymbol{J}_\mathrm{g}^{-\top}\boldsymbol{I}_\mathrm{m}\boldsymbol{J}_\mathrm{g}^{-1})\,{}^{\mathrm{e}}\ddot{\boldsymbol{\theta}} + (\boldsymbol{J}_\mathrm{g}^{-\top}\boldsymbol{D}_\mathrm{m}\boldsymbol{J}_\mathrm{g}^{-1})\,{}^{\mathrm{e}}\dot{\boldsymbol{\theta}} = {}^{\mathrm{e}}\boldsymbol{\tau}_\mathrm{m}\quad, \tag{3.74}$$

resulting in the compact representation

$${}^{\mathrm{g}}\boldsymbol{I}_\mathrm{m}\,{}^{\mathrm{e}}\ddot{\boldsymbol{\theta}} + {}^{\mathrm{g}}\boldsymbol{D}_\mathrm{m}\,{}^{\mathrm{e}}\dot{\boldsymbol{\theta}} = {}^{\mathrm{e}}\boldsymbol{\tau}_\mathrm{m} \tag{3.75}$$

Because of the diagonality of the matrices, the reflected rotor inertia matrix ${}^{\mathrm{e}}\boldsymbol{I}_\mathrm{m}$ and viscous motor and gearbox friction ${}^{\mathrm{e}}\boldsymbol{D}_\mathrm{m}$ are given as

$${}^{\mathrm{e}}\boldsymbol{I}_\mathrm{m} = (\boldsymbol{J}_\mathrm{g}^{-\top}\boldsymbol{I}_\mathrm{m}\boldsymbol{J}_\mathrm{g}^{-1}) = (\boldsymbol{J}_\mathrm{g}^{-1}\boldsymbol{I}_\mathrm{m}\boldsymbol{J}_\mathrm{g}^{-1}) = \mathrm{diag}\big(z_{\mathrm{g}_1}^2\, I_{\mathrm{m}_1}, \ldots, z_{\mathrm{g}_N}^2\, I_{\mathrm{m}_N}\big) \tag{3.76}$$

and

$${}^{\mathrm{e}}\boldsymbol{D}_\mathrm{m} = (\boldsymbol{J}_\mathrm{g}^{-\top}\boldsymbol{D}_\mathrm{m}\boldsymbol{J}_\mathrm{g}^{-1}) = (\boldsymbol{J}_\mathrm{g}^{-1}\boldsymbol{D}_\mathrm{m}\boldsymbol{J}_\mathrm{g}^{-1}) = \mathrm{diag}\big(z_{\mathrm{g}_1}^2\, d_{\mathrm{m}_1}, \ldots, z_{\mathrm{g}_N}^2\, d_{\mathrm{m}_N}\big) \tag{3.77}$$

3.2.6 Experimental Validation

For validation of the actuator models, the joint torque over joint deflection characteristic curve of the third joint was measured and compared to the theoretical models.

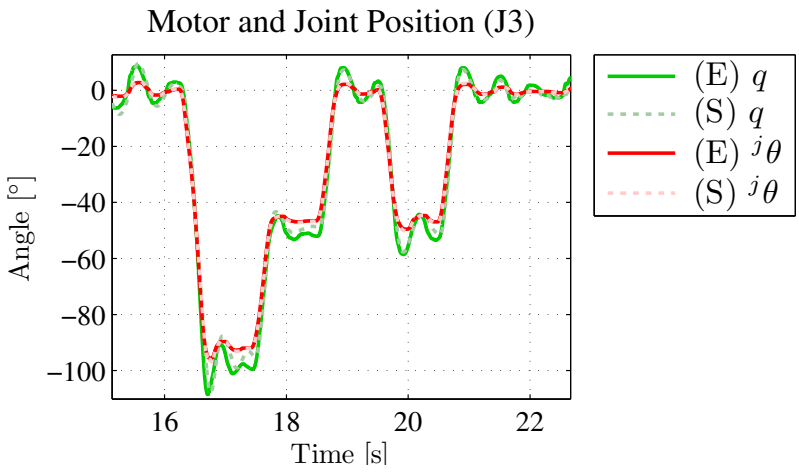

Figure 3.16.: Experimental data (solid lines, marked with 'E') of an excitation trajectory of the third joint of a BioRob-X4 arm compared with the simulated dynamic behavior using the elastic tendon actuator model (dashed lines, marked with 'S').

The stiffness of the springs is $k = 11.580\,\mathrm{kN/m}$. Because two parallel sets of cables are used, the effective stiffness is, according to (3.38),

$$k_i = k_{i,1} + k_{i,2} = 23.160\,\mathrm{kN/m} \tag{3.78}$$

No additional mechanical damping elements are used in parallel to the springs. As analyzed in Section 3.2.3, the internal damping of the springs and tendons is small compared to the damping in the joints and motors. Therefore, the damping parameters of the elastic transmission in the model are set to $d_i = 0\,\mathrm{Ns/m}$. The maximum elongation of the springs is $l_{\max} = 15\,\mathrm{mm}$, the radius of the joint pulley is $R = 3\,\mathrm{cm}$. The pretension force in all springs was set to 40 N, resulting in a combined pretension force of $F_\mathrm{p} = 80\,\mathrm{N}$ for both parallel cables.

The resulting characteristic torque and stiffness curves of the BioRob-X4 elastic tendon actuator for the third joint have been presented in Section 3.2.3. To validate the model, static measurements of the actuator output torque over deflection curve have been made. The results are compared to the calculated stiffness curve in Figure 3.15. The measured values match the derived model quite well. The deviation of the measured data at the corners of the stiffness curve is due to the use of overstretching protection in the springs, as depicted in Figure 3.9.

In addition to the static measurements, also a validation of the dynamic behavior of the elastic tendon actuator has been conducted, as shown in Figure 3.16. For this experiment, the motor position was controlled according to a given excitation trajectory ${}^{\mathrm{j}}\theta_\mathrm{d}$ with respect to the joint side. The resulting joint trajectory q in simulation shows a very good agreement with the measured experimental data.

3.3 Kinematics Model of the BioRob Robot Arm

The BioRob robot arm as shown in Figure 3.1 consists of four elastically actuated joints. The links can be assumed to be stiff for the low payloads the robot arm is intended for and can therefore by modeled as a stiff kinematic chain. Classical modeling methods for rigid-link robotic arms such as the Denavit-Hartenberg (DH) formulation can be used to define the position and orientation

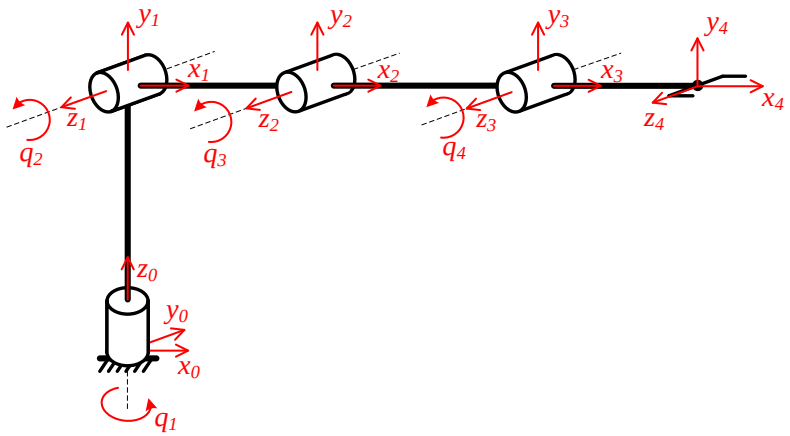

i	θ_i	d_i	a_i	α_i
1	q_1	l_1	0	$\frac{\pi}{2}$
2	q_2	0	l_2	0
3	q_3	0	l_3	0
4	q_4	0	l_4	0

Figure 3.17.: BioRob X4 robot arm kinematic structure and table of DH parameters (with respect to horizontal zero position)

of coordinate frames in each link. The DH parameters defining the kinematic model of the robot arms are listed in Figure 3.17.

3.3.1 Zero Position and Direct Kinematics Model with DH Formulation

The zero position of the kinematics equations can be changed by joint coordinate transformation from joint coordinates $\boldsymbol{q}$ to new joint coordinates $\boldsymbol{q}^*$ with respect to the new zero position $\boldsymbol{q}_0$ defined with respect to $\boldsymbol{q}$:

$$\boldsymbol{q} = \boldsymbol{q}^* + \boldsymbol{q}_0 \tag{3.79}$$

The homogeneous transformation matrices ${}^{i-1}\boldsymbol{T}_i$ defined by the Denavit-Hartenberg (DH) parameters are

$$\begin{aligned} {}^{i-1}\boldsymbol{T}_i &= \mathrm{Rot}(z;\theta_i)\cdot\mathrm{Trans}(0,0,d_i)\cdot\mathrm{Trans}(a_i,0,0)\cdot\mathrm{Rot}(x;\alpha_i) = \left(\begin{array}{c|c} {}^0\boldsymbol{R}_i & {}^0\boldsymbol{r}_i \\ \hline \boldsymbol{0}^\top & 1 \end{array}\right) \\ &= \begin{pmatrix} \cos(\theta_i) & -\sin(\theta_i) & 0 & 0 \\ \sin(\theta_i) & \cos(\theta_i) & 0 & 0 \\ 0 & 0 & 1 & 0 \\ 0 & 0 & 0 & 1 \end{pmatrix} \begin{pmatrix} 1 & 0 & 0 & 0 \\ 0 & 1 & 0 & 0 \\ 0 & 0 & 1 & d_i \\ 0 & 0 & 0 & 1 \end{pmatrix} \begin{pmatrix} 1 & 0 & 0 & a_i \\ 0 & 1 & 0 & 0 \\ 0 & 0 & 1 & 0 \\ 0 & 0 & 0 & 1 \end{pmatrix} \begin{pmatrix} 1 & 0 & 0 & 0 \\ 0 & \cos(\alpha_i) & -\sin(\alpha_i) & 0 \\ 0 & \sin(\alpha_i) & \cos(\alpha_i) & 0 \\ 0 & 0 & 0 & 1 \end{pmatrix} \end{aligned} \tag{3.80}$$

with the position ${}^0\boldsymbol{r}_i$ of coordinate frame i in joint $i+1$, the position of the end-effector ${}^0\boldsymbol{r}_4$, the orientation ${}^0\boldsymbol{R}_i$ of coordinate frame i, and orientation ${}^0\boldsymbol{R}_4$ of the end-effector coordinate frame,

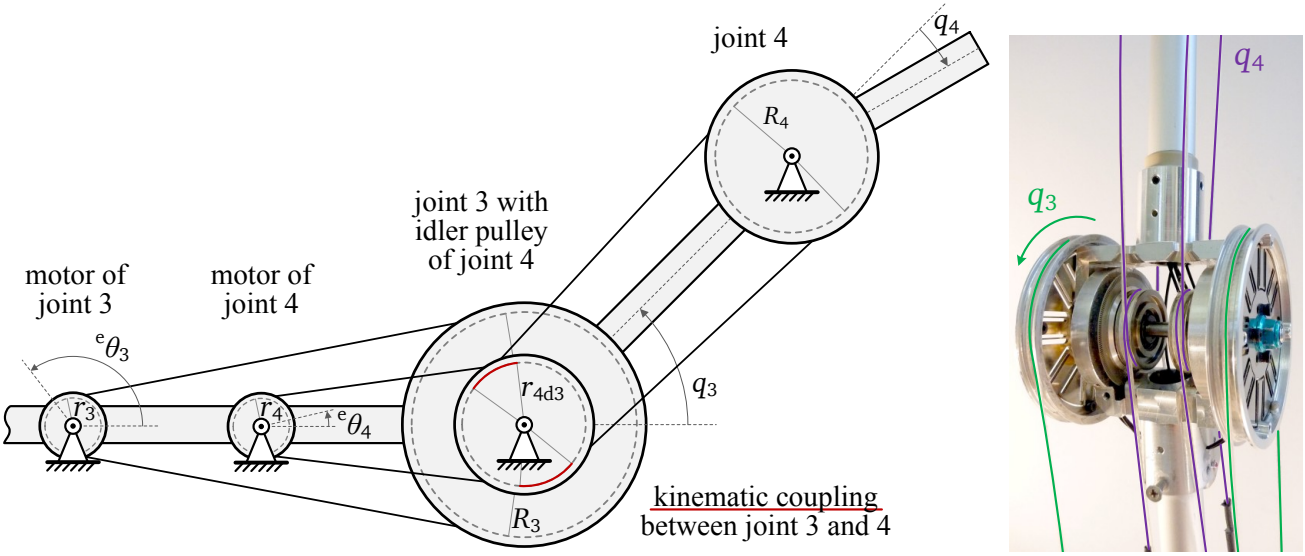

Figure 3.18.: The kinetic coupling of the links is caused by deflection of the tendons of the fourth joint in the third joint (marked in red). The image on the right shows the hardware implementation of the third joint in the BioRob arm.

all with respect to the coordinate system 0. The direct kinematics equations of the horizontal zero position are

$$ {}^0\boldsymbol{r}_1 = \begin{pmatrix} 0 \\ 0 \\ l_1 \end{pmatrix} \quad {}^0\boldsymbol{r}_2 = \begin{pmatrix} l_2 C_1 C_2 \\ l_2 S_1 C_2 \\ l_1 + l_2 S_2 \end{pmatrix} \quad {}^0\boldsymbol{r}_3 = \begin{pmatrix} C_1\left(l_2 C_2 + l_3 C_{23}\right) \\ S_1\left(l_2 C_2 + l_3 C_{23}\right) \\ l_1 + l_2 S_2 + l_3 S_{23} \end{pmatrix} \tag{3.81} $$

$$ {}^0\boldsymbol{r}_4 = \begin{pmatrix} C_1\left(l_2 C_2 + l_3 C_{23} + l_4 C_{234}\right) \\ S_1\left(l_2 C_2 + l_3 C_{23} + l_4 C_{234}\right) \\ l_1 + l_2 S_2 + l_3 S_{23} + l_4 S_{234} \end{pmatrix} \tag{3.82} $$

using the short notation

$$ C_1 = \cos(q_1) \quad , \quad S_1 = \sin(q_1) \quad , \quad C_{12} = \cos(q_1 + q_2) \quad , \tag{3.83} $$

The end-effector orientation is defined by the rotation matrix ${}^0\boldsymbol{R}_4$:

$$ {}^0\boldsymbol{R}_4 = \begin{pmatrix} C_1 C_{234} & -C_1 S_{234} & S_1 \\ S_1 C_{234} & -S_1 S_{234} & -C_1 \\ S_{234} & C_{234} & 0 \end{pmatrix} \tag{3.84} $$

3.3.2 Kinematic Tendon Coupling

Especially for control the equilibrium positions of the joints are important. These are the joint positions q_i and motor positions θ_i where the elasticity between motor and joint produces no

torque. If the motor is mounted on the link it actuates or on the previous link, a direct coupling of motor and joint with tendons is possible and the actuator model of the single joint elastic tendon actuator as described in Section 3.2 can be used. This is for example the case for the third joint. The kinematics equation depends on the motor pulley radius r_3 and on the joint pulley radius R_3 (cf. Figure 3.18) and yields

$$ {}^{\mathrm{g}}\theta_3 \, r_3 = q_3 R_3 \quad \Rightarrow \quad {}^{\mathrm{g}}\theta_3(q_3) = q_3 \frac{R_3}{r_3} \tag{3.85} $$

In case, however, the tendons span multiple joints, additional deflection pulleys are needed. As depicted in Figure 3.18, the motor driving the fourth joint is fixed to the second link and coupled with a deflection pulley with radius $r_{4\mathrm{d}3}$ to the fourth joint. Because of the kinematic coupling between the third and fourth joint, the equilibrium position of this motor not only depends on the joint position q_4 of the fourth joint, but also on the joint position q_3 of the third joint, because the cable wraps around the pulley. The amount of cable that is wrapped around the guiding pulley on the third joint must be equal to the amount of cable that unwinds from the pulley driving the fourth joint, yielding the kinematics equation

$$ {}^{\mathrm{e}}\theta_4 \, r_4 = q_4 R_4 + q_3 \, r_{4\mathrm{d}3} \, , \tag{3.86} $$

which indicates that the motor position ${}^{\mathrm{e}}\theta_4$ of motor four depends both on the joint position of joint three and four

$$ {}^{\mathrm{e}}\theta_4(\boldsymbol{q}) = q_4 \frac{R_4}{r_4} + q_3 \frac{r_{4\mathrm{d}3}}{r_4} \tag{3.87} $$

The resulting angular motor positions ${}^{\mathrm{e}}\boldsymbol{\theta}$ as defined by the joint side tendon position of the transmission elasticity can be transformed into the angular joint positions as defined by the kinematic coupling of the tendons, using a matrix $\boldsymbol{J}_{\mathrm{t}}$ similar to a tendon coupling matrix [47] used for modeling tendon actuated robotic fingers. For the BioRob-X4 arm the resulting matrix is

$$ {}^{\mathrm{e}}\boldsymbol{\theta} = \boldsymbol{J}_{\mathrm{t}}^{-1} \, \boldsymbol{q} = \begin{pmatrix} \frac{R_1}{r_1} & 0 & 0 & 0 \\ 0 & \frac{R_2}{r_2} & 0 & 0 \\ 0 & 0 & \frac{R_3}{r_3} & 0 \\ 0 & 0 & \frac{r_{4\mathrm{d}3}}{r_4} & \frac{R_4}{r_4} \end{pmatrix} \boldsymbol{q} \tag{3.88} $$

with the inverse

$$ \boldsymbol{q} = \boldsymbol{J}_{\mathrm{t}} \, {}^{\mathrm{e}}\boldsymbol{\theta} = \begin{pmatrix} \frac{r_1}{R_1} & 0 & 0 & 0 \\ 0 & \frac{r_2}{R_2} & 0 & 0 \\ 0 & 0 & \frac{r_3}{R_3} & 0 \\ 0 & 0 & -\frac{r_3}{R_3}\frac{r_{4\mathrm{d}3}}{R_4} & \frac{r_4}{R_4} \end{pmatrix} {}^{\mathrm{e}}\boldsymbol{\theta} \tag{3.89} $$

This transformation matrix also describes the transmission behavior from the motor to the joint pulleys and therefore contains the radii r_i of the motor pulleys and the radii of the joint pulleys R_i.

3.3.3 Jacobian

The end-effector Jacobian ${}^0\boldsymbol{J}_4$

$$\begin{pmatrix} -S_1(l_2C_2 + l_3C_{23} + l_4C_{234}) & -C_1(l_2S_2 + l_3S_{23} + l_4S_{234}) & -C_1(l_3S_{23} + l_4S_{234}) & -l_4C_1S_{234} \\ C_1(l_2C_2 + l_3C_{23} + l_4C_{234}) & -S_1(l_2S_2 + l_3S_{23} + l_4S_{234}) & -S_1(l_3S_{23} + l_4S_{234}) & -l_4S_1S_{234} \\ 0 & l_2C_2 + l_3C_{23} + l_4C_{234} & l_3C_{23} + l_4C_{234} & l_4C_{234} \\ 0 & S_1 & S_1 & S_1 \\ 0 & -C_1 & -C_1 & -C_1 \\ 1 & 0 & 0 & 0 \end{pmatrix} \tag{3.90}$$

$$= \begin{pmatrix} {}^0\boldsymbol{J}_{v_4}(\boldsymbol{q}) \\ {}^0\boldsymbol{J}_{\omega_4}(\boldsymbol{q}) \end{pmatrix} \tag{3.91}$$

can be used for transformation from joint velocities $\dot{\boldsymbol{q}}$ to Cartesian end-effector velocities ${}^0\dot{\boldsymbol{r}}_4$

$${}^0\dot{\boldsymbol{r}}_4 = {}^0\boldsymbol{J}_4(\boldsymbol{q})\,\dot{\boldsymbol{q}}\ , \tag{3.92}$$

or for mapping of Cartesian end-effector forces $\boldsymbol{f}$ to joint torques $\boldsymbol{\tau}$ [29]

$$\boldsymbol{\tau} = {}^0\boldsymbol{J}_{v_4}^{\top}(\boldsymbol{q})\,\boldsymbol{f} \tag{3.93}$$

3.4 Dynamics Model of BioRob Robot Arm

The dynamics model is used for simulation and controller design. In simulation, the behavior of the model can be studied without the need to perform time-consuming experiments, also avoiding wear of the hardware. It is especially useful for examining scenarios such as collision detection, which are difficult to perform with the hardware. Simulations can also provide additional data, that would be difficult to measure, such as collision reaction forces.

However, only effects can be studied that are modeled with sufficient accuracy. The most important effects are the robot arm dynamics consisting of the dynamics of the rigid structure and the joint elasticity, described in Section 3.4.2. The dynamics model of the motors (Section 3.2.4) is required to take actuator saturation into account. It also should allow to simulate the torque loads and peaks caused by collisions.

The primary requirement for the dynamics model is steady state accuracy, which is important for the controller design. Besides the steady state equations and parameters of motors and robot arm, the nonlinear joint elasticity is to be modeled accurately, shown in Section 3.4.2, due to the low elasticity and therefore large spring deflection. The second important requirement is the accurate modeling of the joint oscillations caused by the joint elasticity. An accurate model of this behavior allows for a better controller design in simulation.

A detailed analysis of the coupling effects of tendon-driven actuation on the dynamics of robot arms with general tendon routing can be found in [32]. In [53], a general model of tendon-driven robotic arms describing the dynamic effects of a multi-stage non-stiff transmission was presented. Such a level of detail, however, is only necessary if the idler pulley inertia is large or in case of a large number of transmission stages. As the presented robot arm design only uses small idler pulleys and at most two transmission stages, these effects are not modeled here.

Table 3.3.: Overview over the transformation between the motor state space, the elastic tendon actuator (ETA) output state space, and the joint state space. The gearbox transformation matrix $\boldsymbol{J}_{\mathrm{g}}$ is assumed to be a diagonal matrix, therefore $\boldsymbol{J}_{\mathrm{g}} = \boldsymbol{J}_{\mathrm{g}}^{\top}$. States not directly connected with arrows are reflected through the elasticity.

State	Motor	Actuator Output	Joint
Motor torque	$\boldsymbol{\tau}_m$ $\xrightarrow{\boldsymbol{J}_{\mathrm{g}}^{-\top} = \boldsymbol{J}_{\mathrm{g}}^{-1}}$ $\xleftarrow{\boldsymbol{J}_{\mathrm{g}}^{\top} = \boldsymbol{J}_{\mathrm{g}}}$	${}^{e}\boldsymbol{\tau}_m$	${}^{j}\boldsymbol{\tau}_m$
ETA torque	${}^{m}\boldsymbol{\tau}_e$	$\boldsymbol{\tau}_e$ $\xrightarrow{\boldsymbol{J}_{\mathrm{t}}^{-\top}}$ $\xleftarrow{\boldsymbol{J}_{\mathrm{t}}^{\top}}$	${}^{j}\boldsymbol{\tau}_e$
Motor position	$\boldsymbol{\theta}$ $\xrightarrow{\boldsymbol{J}_{\mathrm{g}}}$ $\xleftarrow{\boldsymbol{J}_{\mathrm{g}}^{-1}}$	${}^{e}\boldsymbol{\theta}$	${}^{j}\boldsymbol{\theta}$
Joint position	${}^{m}\boldsymbol{q}$	${}^{e}\boldsymbol{q}$ $\xrightarrow{\boldsymbol{J}_{\mathrm{t}}}$ $\xleftarrow{\boldsymbol{J}_{\mathrm{t}}^{-1}}$	$\boldsymbol{q}$

3.4.1 Elastic Tendon Coupling and Reflected Variables

In case of elastic decoupling of motor positions $\boldsymbol{\theta}$ and joint positions $\boldsymbol{q}$, the kinematic coupling caused by the tendon routing discussed in Section 3.3.2 describes the relationship between the joint positions $\boldsymbol{q}$ and virtual angular positions ${}^{e}\boldsymbol{q}$ which correspond to the link side position of the elasticity:

$$ {}^{e}\boldsymbol{q} = \boldsymbol{J}_{\mathrm{t}}^{-1}\,\boldsymbol{q} \qquad \text{and} \qquad \boldsymbol{q} = \boldsymbol{J}_{\mathrm{t}}\,{}^{e}\boldsymbol{q} \tag{3.94} $$

The principle of virtual work

$$ {}^{\mathrm{e}}\dot{\boldsymbol{q}}^{\top}\,\boldsymbol{\tau}_{\mathrm{e}} \;=\; \dot{\boldsymbol{q}}^{\top}\,{}^{\mathrm{j}}\boldsymbol{\tau}_{\mathrm{e}} \;=\; (\boldsymbol{J}_{\mathrm{t}}\,{}^{\mathrm{e}}\dot{\boldsymbol{q}})^{\top}\,{}^{\mathrm{j}}\boldsymbol{\tau}_{\mathrm{e}} \;=\; {}^{\mathrm{e}}\dot{\boldsymbol{q}}^{\top}\,\boldsymbol{J}_{\mathrm{t}}^{\top}\,{}^{\mathrm{j}}\boldsymbol{\tau}_{\mathrm{e}} \tag{3.95} $$

yields the matrices for transformation between actuator output space and joint space:

$$ {}^{\mathrm{j}}\boldsymbol{\tau}_{\mathrm{e}} = \boldsymbol{J}_{\mathrm{t}}^{-\top}\,\boldsymbol{\tau}_{\mathrm{e}} \qquad \text{and} \qquad \boldsymbol{\tau}_{\mathrm{e}} = \boldsymbol{J}_{\mathrm{t}}^{\top}\,{}^{\mathrm{j}}\boldsymbol{\tau}_{\mathrm{e}} \tag{3.96} $$

Table 3.3 summarizes the matrices used for transformation between motor space, actuator input space, and joint space.

The elastic torques at the gearbox shaft

$$ \boldsymbol{\tau}_{\mathrm{e}} \;=\; \boldsymbol{K}_{\mathrm{e}}\,({}^{\mathrm{e}}\boldsymbol{\theta} - {}^{\mathrm{e}}\boldsymbol{q}) \;+\; \boldsymbol{D}_{\mathrm{e}}\,({}^{\mathrm{e}}\dot{\boldsymbol{\theta}} - {}^{\mathrm{e}}\dot{\boldsymbol{q}}) \tag{3.97} $$

with the diagonal stiffness matrix $\boldsymbol{K}_{\mathrm{e}}$ and damping matrix $\boldsymbol{D}_{\mathrm{e}}$ with respect to the gearbox shaft, as derived in Section 3.2.1,

$$\boldsymbol{K}_{\mathrm{e}} = \mathrm{diag}\big(r_1^2\, k_1, \ldots, r_N^2\, k_N\big) \tag{3.98}$$

$$\boldsymbol{D}_{\mathrm{e}} = \mathrm{diag}\big(r_1^2\, d_1, \ldots, r_N^2\, d_N\big)\,, \tag{3.99}$$

can be transformed to the joint side

$$\begin{aligned} {}^{\mathrm{j}}\boldsymbol{\tau}_{\mathrm{e}} &= \boldsymbol{J}_{\mathrm{t}}^{-\top}\Big(\boldsymbol{K}_{\mathrm{e}}({}^{\mathrm{e}}\boldsymbol{\theta} - {}^{\mathrm{e}}\boldsymbol{q}) \;+\; \boldsymbol{D}_{\mathrm{e}}({}^{\mathrm{e}}\dot{\boldsymbol{\theta}} - {}^{\mathrm{e}}\dot{\boldsymbol{q}})\Big) && (3.100)\\ &= \boldsymbol{J}_{\mathrm{t}}^{-\top}\,\boldsymbol{K}_{\mathrm{e}}\,\boldsymbol{J}_{\mathrm{t}}^{-1}\big(\boldsymbol{J}_{\mathrm{t}}\,{}^{\mathrm{e}}\boldsymbol{\theta} - \boldsymbol{J}_{\mathrm{t}}\,{}^{\mathrm{e}}\boldsymbol{q}\big) \;+\; \boldsymbol{J}_{\mathrm{t}}^{-\top}\,\boldsymbol{D}_{\mathrm{e}}\,\boldsymbol{J}_{\mathrm{t}}^{-1}\big(\boldsymbol{J}_{\mathrm{t}}\,{}^{\mathrm{e}}\dot{\boldsymbol{\theta}} - \boldsymbol{J}_{\mathrm{t}}\,{}^{\mathrm{e}}\dot{\boldsymbol{q}}\big) && (3.101)\\ &= \boldsymbol{J}_{\mathrm{t}}^{-\top}\,\boldsymbol{K}_{\mathrm{e}}\,\boldsymbol{J}_{\mathrm{t}}^{-1}\big({}^{\mathrm{j}}\boldsymbol{\theta} - \boldsymbol{q}\big) \;+\; \boldsymbol{J}_{\mathrm{t}}^{-\top}\,\boldsymbol{D}_{\mathrm{e}}\,\boldsymbol{J}_{\mathrm{t}}^{-1}\big({}^{\mathrm{j}}\dot{\boldsymbol{\theta}} - \dot{\boldsymbol{q}}\big) && (3.102) \end{aligned}$$

As can be seen from this equation, the unloaded equilibrium joint positions $\boldsymbol{q}_{\mathrm{eq}}$ are given by

$$\boldsymbol{q}_{\mathrm{eq}} = {}^{\mathrm{j}}\boldsymbol{\theta} = \boldsymbol{J}_{\mathrm{t}}\,{}^{\mathrm{g}}\boldsymbol{\theta} = \boldsymbol{J}_{\mathrm{t}}\boldsymbol{J}_{\mathrm{g}}\,\boldsymbol{\theta} \tag{3.103}$$

Because of the kinematic tendon coupling, the joint side stiffness matrix ${}^{\mathrm{j}}\boldsymbol{K}_{\mathrm{e}}$ exhibits joint coupling, unlike $\boldsymbol{K}_e$

$${}^{\mathrm{j}}\boldsymbol{K}_{\mathrm{e}} = \boldsymbol{J}_{\mathrm{t}}^{-\top}\,\boldsymbol{K}_{\mathrm{e}}\,\boldsymbol{J}_{\mathrm{t}}^{-1} \tag{3.104}$$

For the BioRob-X4 arm the resulting stiffness matrix with respect to the joint side is

$${}^{\mathrm{j}}\boldsymbol{K}_{\mathrm{e}} = \begin{pmatrix} R_1^2\, k_1 & 0 & 0 & 0 \\ 0 & R_2^2\, k_2 & 0 & 0 \\ 0 & 0 & R_3^2\, k_3 + r_{4\mathrm{d}3}^2\, k_4 & R_4\, r_{4\mathrm{d}3}\, k_4 \\ 0 & 0 & R_4\, r_{4\mathrm{d}3}\, k_4 & R_4^2\, k_4 \end{pmatrix} \tag{3.105}$$

The damping matrix with respect to the joint side is defined similarly

$${}^{\mathrm{j}}\boldsymbol{D}_{\mathrm{e}} = \boldsymbol{J}_{\mathrm{t}}^{-\top}\,\boldsymbol{D}_{\mathrm{e}}\,\boldsymbol{J}_{\mathrm{t}}^{-1} \tag{3.106}$$

resulting in the matrix

$${}^{\mathrm{j}}\boldsymbol{D}_{\mathrm{e}} = \begin{pmatrix} R_1^2\, d_1 & 0 & 0 & 0 \\ 0 & R_2^2\, d_2 & 0 & 0 \\ 0 & 0 & R_3^2\, d_3 + r_{4\mathrm{d}3}^2\, d_4 & R_4\, r_{4\mathrm{d}3}\, d_4 \\ 0 & 0 & R_4\, r_{4\mathrm{d}3}\, d_4 & R_4^2\, d_4 \end{pmatrix} \tag{3.107}$$

This yields a compact representation for the joint side

$${}^{\mathrm{j}}\boldsymbol{\tau}_{\mathrm{e}} = {}^{\mathrm{j}}\boldsymbol{K}_{\mathrm{e}}({}^{j}\boldsymbol{\theta} - \boldsymbol{q}) \;+\; {}^{\mathrm{j}}\boldsymbol{D}_{\mathrm{e}}({}^{j}\dot{\boldsymbol{\theta}} - \dot{\boldsymbol{q}}) \tag{3.108}$$

Similarly, the motor equation

Table 3.4.: Examples for the state transformation between the state spaces.

State	Motor	Actuator Output	Joint
Motor torque	$\boldsymbol{\tau}_\mathrm{m} = \boldsymbol{J}_\mathrm{g}\, {}^\mathrm{e}\boldsymbol{\tau}_\mathrm{m}$ $= \boldsymbol{J}_\mathrm{g}\boldsymbol{J}_\mathrm{t}^\top\, {}^\mathrm{j}\boldsymbol{\tau}_\mathrm{m}$	${}^\mathrm{e}\boldsymbol{\tau}_\mathrm{m} = \boldsymbol{J}_\mathrm{g}^{-1}\, \boldsymbol{\tau}_\mathrm{m}$ $= \boldsymbol{J}_\mathrm{t}^\top\, {}^\mathrm{j}\boldsymbol{\tau}_\mathrm{m}$	${}^\mathrm{j}\boldsymbol{\tau}_\mathrm{m} = \boldsymbol{J}_\mathrm{t}^{-\top}\, {}^\mathrm{e}\boldsymbol{\tau}_\mathrm{m}$ $= \boldsymbol{J}_\mathrm{t}^{-\top}\boldsymbol{J}_g^{-1}\, \boldsymbol{\tau}_\mathrm{m}$
Motor position	$\boldsymbol{\theta} = \boldsymbol{J}_\mathrm{g}^{-1}\, {}^\mathrm{e}\boldsymbol{\theta}$ $= \boldsymbol{J}_\mathrm{g}^{-1}\boldsymbol{J}_\mathrm{t}^{-1}\, {}^\mathrm{j}\boldsymbol{\theta}$	${}^\mathrm{e}\boldsymbol{\theta} = \boldsymbol{J}_\mathrm{g}\, \boldsymbol{\theta}$ $= \boldsymbol{J}_\mathrm{t}^{-1}\, {}^\mathrm{j}\boldsymbol{\theta}$	${}^\mathrm{j}\boldsymbol{\theta} = \boldsymbol{J}_\mathrm{t}\, {}^\mathrm{e}\boldsymbol{\theta}$ $= \boldsymbol{J}_\mathrm{t}\boldsymbol{J}_\mathrm{g}\, \boldsymbol{\theta}$

$$\boldsymbol{I}_\mathrm{m}\ddot{\boldsymbol{\theta}} + \boldsymbol{D}_\mathrm{m}\dot{\boldsymbol{\theta}} + {}^\mathrm{m}\boldsymbol{\tau}_\mathrm{e} = \boldsymbol{\tau}_\mathrm{m} \tag{3.109}$$

with diagonal rotor and gearbox inertia matrix $\boldsymbol{I}_\mathrm{m}$ consisting of the motor rotor inertias I_{r_i} with respect to the rotor rotating axis, diagonal viscous motor damping matrix $\boldsymbol{D}_\mathrm{m}$, and external torque ${}^\mathrm{m}\boldsymbol{\tau}_\mathrm{e} = \boldsymbol{J}_\mathrm{g}^\top\, \boldsymbol{\tau}_\mathrm{e}$, can, by defining a diagonal matrix $\boldsymbol{J}_\mathrm{g}$ containing the gearbox ratios

$${}^\mathrm{e}\boldsymbol{\theta} = \boldsymbol{J}_\mathrm{g}\, \boldsymbol{\theta} = \mathrm{diag}\left(\tfrac{1}{n_{g_1}} \quad \cdots \quad \tfrac{1}{n_{g_N}}\right) \boldsymbol{\theta}\ , \tag{3.110}$$

be transformed to the joint side

$${}^\mathrm{j}\boldsymbol{I}_\mathrm{m}\,{}^\mathrm{j}\ddot{\boldsymbol{\theta}} + {}^\mathrm{j}\boldsymbol{D}_\mathrm{m}\,{}^\mathrm{j}\dot{\boldsymbol{\theta}} + {}^\mathrm{j}\boldsymbol{\tau}_\mathrm{e} = {}^\mathrm{j}\boldsymbol{\tau}_\mathrm{m} \tag{3.111}$$

yielding

$${}^\mathrm{j}\boldsymbol{I}_\mathrm{m} = \boldsymbol{J}_\mathrm{t}^{-\top}\boldsymbol{J}_\mathrm{g}^{-\top}\boldsymbol{I}_\mathrm{m}\boldsymbol{J}_\mathrm{g}^{-1}\boldsymbol{J}_\mathrm{t}^{-1} \tag{3.112}$$

$${}^\mathrm{j}\boldsymbol{D}_\mathrm{m} = \boldsymbol{J}_\mathrm{t}^{-\top}\boldsymbol{J}_\mathrm{g}^{-\top}\boldsymbol{D}_\mathrm{m}\boldsymbol{J}_\mathrm{g}^{-1}\boldsymbol{J}_\mathrm{t}^{-1} \tag{3.113}$$

for reflected motor parameters.

3.4.2 Complete Mechanical Dynamics Model

In this section, the dynamics model of the BioRob arm with coupled elastic tendon actuators, as shown in Figure 3.19, is formulated with respect to the joint state space. It is assumed that the mass of the tendons and springs is small and that the kinetic energy of these elements can be neglected compared to the kinetic energy of the other mechanical robot arm parts.

The mass of each motor can be added to the link it is connected to. The transmission ratios of the gearbox and the cable and pulley elements can be multiplied. All variables can then be calculated as reflected variables with respect to the joint side, as described in the former section.

The MBS dynamics of the robot arm and the motors can be described by using the reduced model of elastic joint robots. For formal derivation of these equations see [59, 61].

Because the motors are mounted on the first and second joint and therefore moving with lower kinetic energy, and because of the large reduction ratios (the overall reduction ratios $z_i = z_{\mathrm{g}_i} z_{\mathrm{p}_i}$ have a magnitude of 100 to 150), it is possible to neglect the effects of the inertial

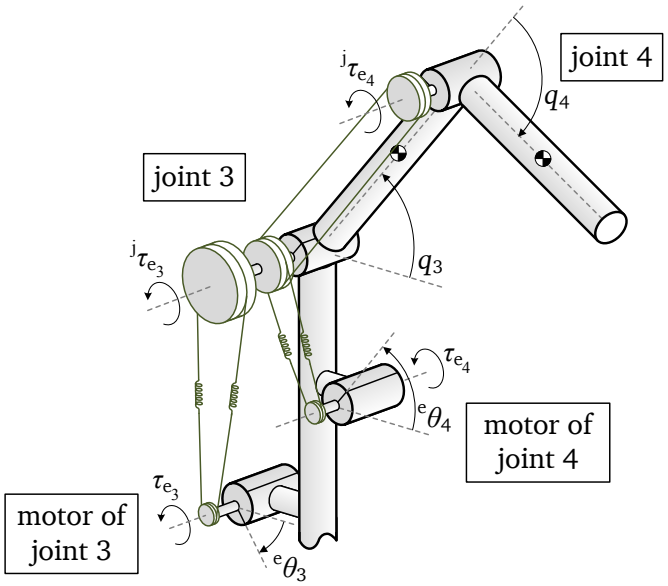

Figure 3.19.: Elastic tendon actuation model of joint 3 and 4. The tendons, pulleys, and springs are colored green.

couplings between the motors and the links. Thus the reduced model can be used, as stated in [59]. Otherwise, a more general model would have to be used [60]. Also, the fact that the motors are not located in the joints but mounted on the links, would have to be considered and modeled [46].

By using the reflected motor and actuation parameters and states , the dynamics equations are transformed to the joint side , obtaining a similar structure as the equations of elastic joint manipulators [59]

$$ {}^{\mathrm{j}}\boldsymbol{I}_{\mathrm{m}}\,{}^{\mathrm{j}}\ddot{\boldsymbol{\theta}} + {}^{\mathrm{j}}\boldsymbol{D}_{\mathrm{m}}\,{}^{\mathrm{j}}\dot{\boldsymbol{\theta}} + {}^{\mathrm{j}}\boldsymbol{\tau}_{\mathrm{e}} = {}^{\mathrm{j}}\boldsymbol{\tau}_{\mathrm{m}} \tag{3.114} $$

$$ \boldsymbol{M}(\boldsymbol{q})\ddot{\boldsymbol{q}} + \boldsymbol{C}(\boldsymbol{q},\dot{\boldsymbol{q}})\dot{\boldsymbol{q}} + \boldsymbol{D}\dot{\boldsymbol{q}} + \boldsymbol{g}(\boldsymbol{q}) = {}^{\mathrm{j}}\boldsymbol{\tau}_{\mathrm{e}} \tag{3.115} $$

$$ {}^{\mathrm{j}}\boldsymbol{K}_{\mathrm{e}}({}^{j}\boldsymbol{\theta} - \boldsymbol{q}) + {}^{\mathrm{j}}\boldsymbol{D}_{\mathrm{e}}({}^{j}\dot{\boldsymbol{\theta}} - \dot{\boldsymbol{q}}) = {}^{\mathrm{j}}\boldsymbol{\tau}_{\mathrm{e}} \tag{3.116} $$

Equation (3.115) describes the dynamics of the rigid structure with mass matrix $\boldsymbol{M}$, Coriolis matrix $\boldsymbol{C}$, and gravity torque vector $\boldsymbol{g}$. Equation (3.114) describes the dynamics of the motor rotors with the diagonal motor rotor inertia matrix $\boldsymbol{I}_{\mathrm{m}}$ and motor torque $\boldsymbol{\tau}_{\mathrm{m}}$. The mass matrix $\boldsymbol{M}$ consists of the inertia and mass of the links, including the motor masses, which are added to the links where they are mounted, cf. Figure 3.1. The mass of the cables and mechanical elasticity is neglectable. The diagonal matrix $\boldsymbol{I}_{\mathrm{m}}$ consists of the motor rotor inertias $I_{\mathrm{m}_{i_{zz}}}$ with respect to the rotor rotating axis. These are the reflected motor inertia values as stated in Section Section 3.2.5. Important parameters are listed in Table 3.7. All actuator parameters are given with respect to the joint.

3.5 Simulation Concept and Implementation

A simulation model was developed for analysis of the dynamic behavior, safety, and controller design. Because of the model complexity of the robot arm with elastic tendon actuation, to enable

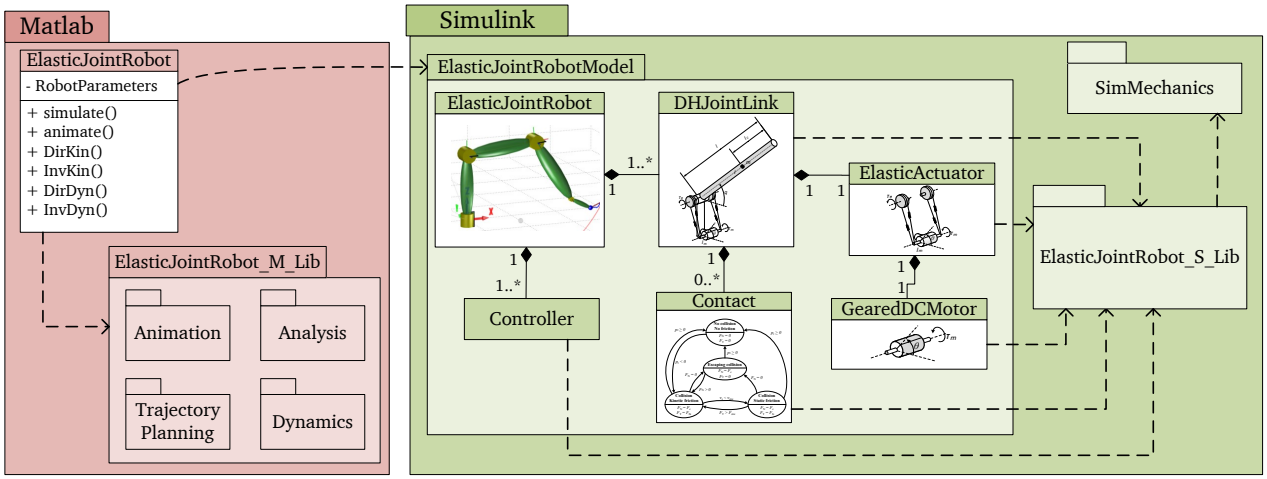

Figure 3.20.: Architecture of the developed toolbox including the Matlab and Simulink libaries for simulation of elastic joint robots.

simulation of robotic arms with combinations of different actuators, and to be able to investigate highly transient impact situations, a modular simulation library for the presented model parts was developed. The development was necessary because at the beginning of this thesis, no adequate open source simulation framework was available meeting these requirements. using technical computing software, a combination of model-based programming for the complex physical models and a class-based programming for data and parameter storage was chosen.

To maintain consistency between the class-based parameter and data structure (cf. Figure 3.20 "“Matlab"” package) and the model-based representation of the robot arm hardware (cf. Figure 3.20 "“Simulink"” package), the simulation framework allows to automatically generate models from a given robot object. This creation process takes into consideration the class structure of the robot object, for example the actuator types used in the robot, and the presence of contact models. Additionally, the robot object parameter values are used to create a corresponding model with the desired granularity. For example, motor armature inductances are only modeled in case the inductance of the corresponding actuator is not equal to zero. Finally, several additional global parameters for the control of the model creation process are available. The resulting model can be manually edited and reviewed. For debugging purposes, modules can be isolated and simulated individually.

The class structure of a robotic arm in the simulation framework is displayed in Figure A.1.

3.6 Model Identification and Validation

This section describes the experimental validation of the derived dynamics models. In a first step, the unknown dynamics parameters are identified. Because of the special, non-modular structure of the robot arm, identification of disassembled parts or single links is not feasible. Instead, the identification must be performed using the full robot arm. For this, a trajectory with single joint excitation starting from the last joint was used.

In the second step, the validity of the identified dynamics model was tested using experimental measurements from different trajectories, namely a pick-and-place trajectory and a random high-

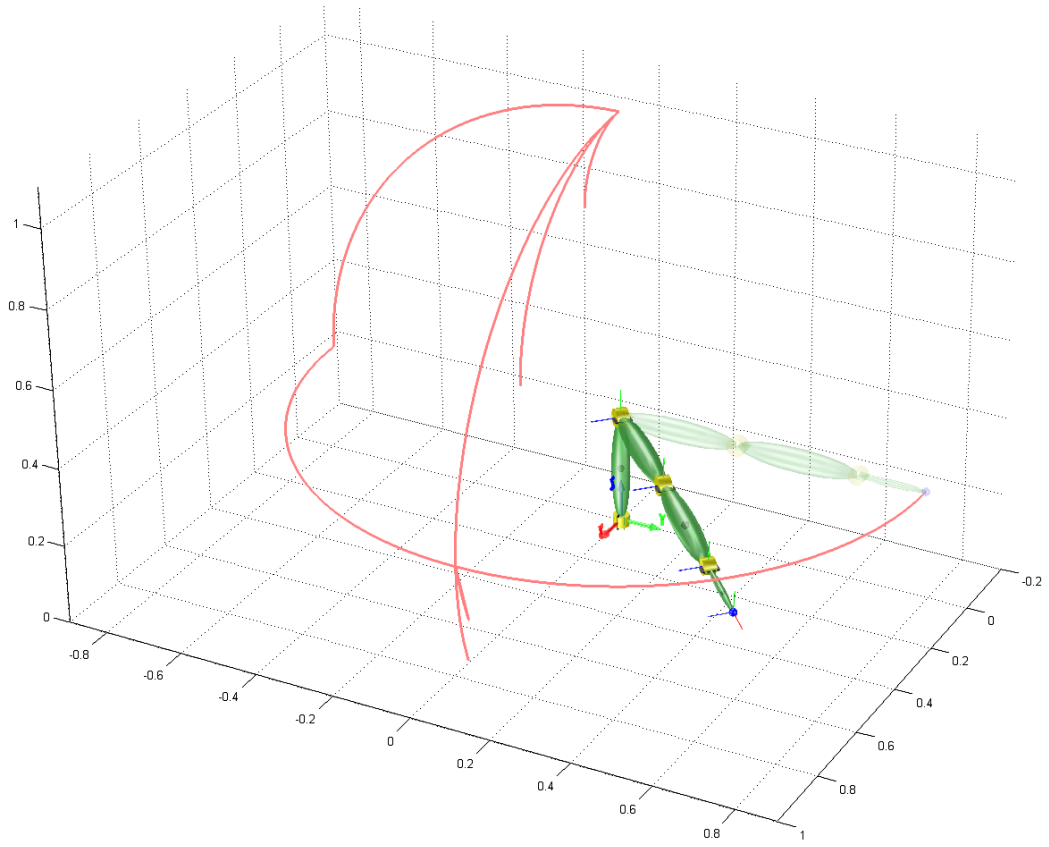

Figure 3.21.: Trajectory with undamped single joint excitation used for experimental parameter identification.

speed trajectory with end-effector velocities up to 6 m/s. In this step, all electrical and mechanical actuator and joint states were compared.

3.6.1 Parameter Identification

For identification of the unknown dynamics parameters, the trajectory shown in Figure 3.21 was used. It consists of successive fast joint motions for single joint excitation. For the excitation trajectory, only the motor state ${}^{\mathrm{j}}\boldsymbol{\theta}$ and its velocity were used for control in order to achieve a highly undamped behavior on the joint side

The joint velocity is obtained by numerical differentiation of the joint position sensor readings. This introduces a lot of numerical noise, as can be for example seen in the angular velocity plot of Figure 3.22. In simulation, the joint velocity values are directly obtained from the multi-body dynamics model and therefore, these values do not show numerical noise. In Section 4.1.2, an observer is discussed which estimates the joint velocity to avoid the noise introduced by numerical differentiation.

Figures 3.22 to 3.24 provide a comparison between the dynamics model with the identified parameters and experimental measurements for joint two to four.

The results are quite reasonable. The largest errors occur in case of steady state motor position and joint position oscillations, where the motor torque ${}^{\mathrm{j}}\tau_{\mathrm{m}}$ displays more response to joint oscillations in simulation compared to the experiment (cf. motor and joint torque in Figure 3.22).

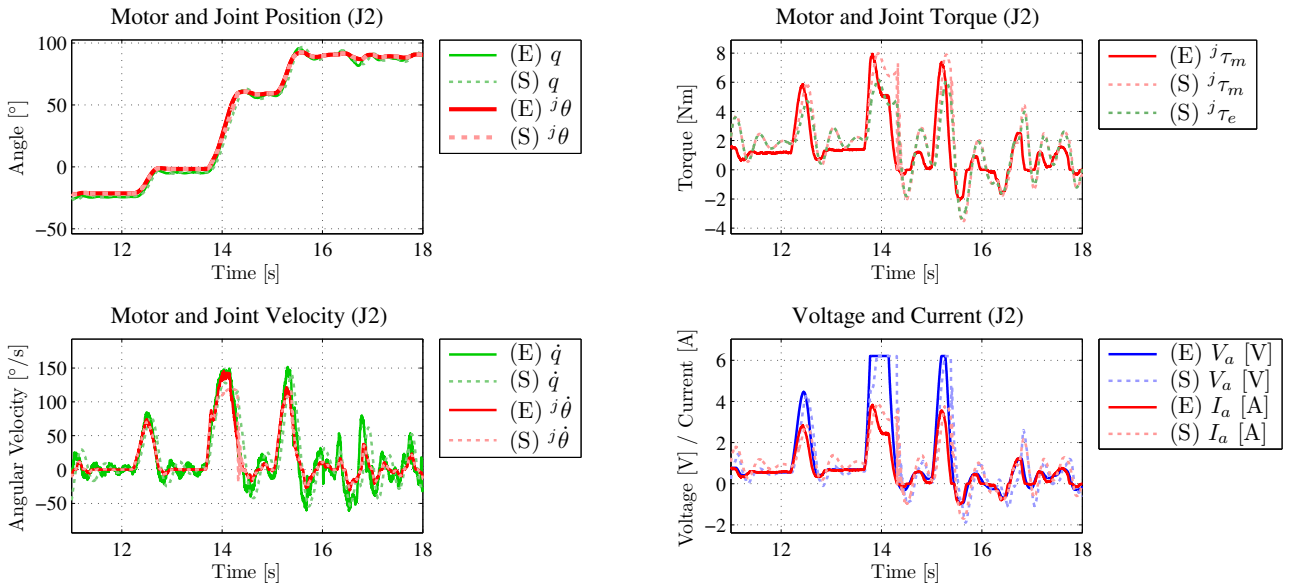

Figure 3.22.: Comparison between the experimental measurements (E) of the undamped joint excitation trajectory used for identification and the simulated dynamics model with the identified parameters (S) for joint two.

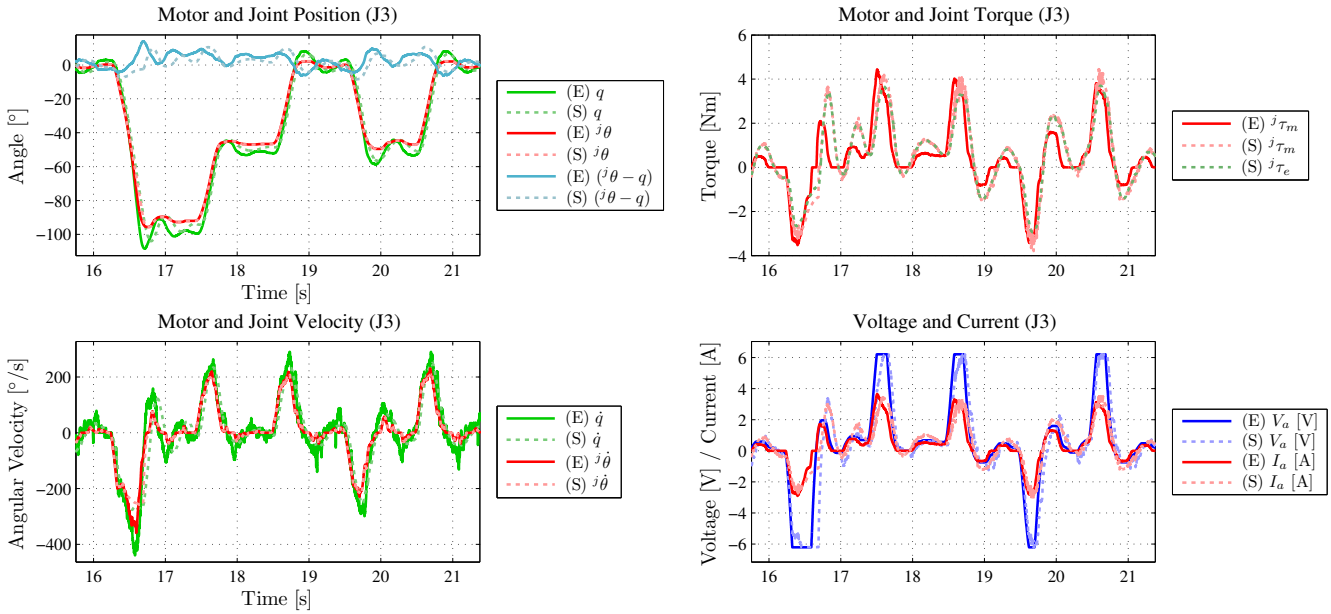

Figure 3.23.: Comparison between the experimental measurements (E) of the undamped joint excitation trajectory used for identification and the simulated dynamics model with the identified parameters (S) for joint three.

Table 3.5.: Important scalar and vectorial model parameters of the BioRob-X4 arm including gripper. Note that, because other springs were used, the values from the actuator in joint three differ from the values used in Section 3.2.

Link	**1**	**2**	**3**	**4**
DH (d, a, α)	$(0.276, 0, \frac{\pi}{2})$	$(0, 0.307, 0)$	$(0, 0.310, 0)$	$(0, 0.10, 0)$
r_c [m]	$(0, -0.138, 0)$	$(-0.317, 0, 0)$	$(-0.155, 0, 0)$	$(-0.080, 0, 0)$
m [kg]	2.350	1.530	0.160	0.055
I_z [kgm^2]	$11.8 \cdot 10^{-3}$	$12.0 \cdot 10^{-3}$	$1.28 \cdot 10^{-3}$	$45.8 \cdot 10^{-6}$
d [Nm/rad]	0.25	1.5	0.5	0.05
q_{res} [-]	4096	4096	4096	4096
Elastic Tendon Actuator	**1**	**2**	**3**	**4**
${}^j k_e$ [Nm/rad]	40.1	45.1	19.05	6.3
${}^j d_e$ [Nms/rad]	0.05	0.05	0.05	0.05
$\frac{r_{id(i-1)}}{r_i}$ [−]	-	-	-	0.5
R_i [cm]	2.40	4.0	3.0	2.5
r_i [cm]	0.75	1.15	1.15	0.90
$z_p = \frac{R_i}{r_i}$ [−]	3.20	3.48	2.61	2.78
$z_g\, z_p$ [−]	73.6	80.0	47.0	52.8
DC Motor	**1**	**2**	**3**	**4**
${}^j I_m$ [kgm^2]	$18.5 \cdot 10^{-3}$	$21.8 \cdot 10^{-3}$	$7.52 \cdot 10^{-3}$	$2.92 \cdot 10^{-3}$
d_m [Nms/rad]	$1.5 \cdot 10^{-4}$	$1.5 \cdot 10^{-4}$	$0.5 \cdot 10^{-4}$	$1.5 \cdot 10^{-4}$
${}^j d_m$ [Nms/rad]	0.813	0.960	0.110	0.418
${}^j \tau_{m,max}$ [Nm]	9.5	10.4	6.1	6.2
z_g [−]	23.0	23.0	18.0	19.0
R_a [Ω]	0.611	0.611	0.611	2.19
k_t [Nm/A]	0.0259	0.0259	0.0259	0.0235
k_v [Vs/rad]	0.0259	0.0259	0.0259	0.0235
L_a [Vs/rad]	$1.19 \cdot 10^{-4}$	$1.19 \cdot 10^{-4}$	$1.19 \cdot 10^{-4}$	$2.38 \cdot 10^{-4}$

Table 3.6.: Important joint level matrix model parameters of the BioRob-X4 arm including gripper: link inertia matrix with respect to center of link mass.

Link	**1**	**2**
$\boldsymbol{I}_{\mathrm{r_{c_i}}}$	$\begin{pmatrix} 0.0149 & 0 & 0 \\ 0 & 0.0149 & 0 \\ 0 & 0 & 0.0118 \end{pmatrix}$	$\begin{pmatrix} 0.0007 & 0 & 0 \\ 0 & 0.0120 & 0 \\ 0 & 0 & 0.0120 \end{pmatrix}$
	3	**4**
	$\begin{pmatrix} 3.2 \cdot 10^{-5} & 0 & 0 \\ 0 & 1.28 \cdot 10^{-3} & 0 \\ 0 & 0 & 1.28 \cdot 10^{-3} \end{pmatrix}$	$\begin{pmatrix} 1.10 \cdot 10^{-5} & 0 & 0 \\ 0 & 4.58 \cdot 10^{-5} & 0 \\ 0 & 0 & 4.58 \cdot 10^{-5} \end{pmatrix}$

Table 3.7.: Important global matrix model parameters of the BioRob-X4 arm including gripper: transmission stiffness $\boldsymbol{K}_{\mathrm{e}}$, gearbox transmission matrix $\boldsymbol{J}_{g}$, and tendon coupling matrix including pulley transmission $\boldsymbol{J}_{\mathrm{t}}$.

Global Matrix Parameters			
$\boldsymbol{K}_{\mathrm{e}}$	$\begin{pmatrix} 3.92 & 0 & 0 & 0 \\ 0 & 3.734 & 0 & 0 \\ 0 & 0 & 2.80 & 0 \\ 0 & 0 & 0 & 0.810 \end{pmatrix}$	${}^{\mathrm{j}}\boldsymbol{K}_{\mathrm{e}}$	$\begin{pmatrix} 40.1 & 0 & 0 & 0 \\ 0 & 45.1 & 0 & 0 \\ 0 & 0 & 20.6 & 3.13 \\ 0 & 0 & 3.13 & 6.3 \end{pmatrix}$
$\boldsymbol{J}_{\mathrm{g}}$	$\begin{pmatrix} 0.0435 & 0 & 0 & 0 \\ 0 & 0.0435 & 0 & 0 \\ 0 & 0 & 0.0556 & 0 \\ 0 & 0 & 0 & 0.0526 \end{pmatrix}$	$\boldsymbol{J}_{\mathrm{t}}$	$\begin{pmatrix} 0.3125 & 0 & 0 & 0 \\ 0 & 0.2875 & 0 & 0 \\ 0 & 0 & 0.3833 & 0 \\ 0 & 0 & -0.1917 & 0.3600 \end{pmatrix}$

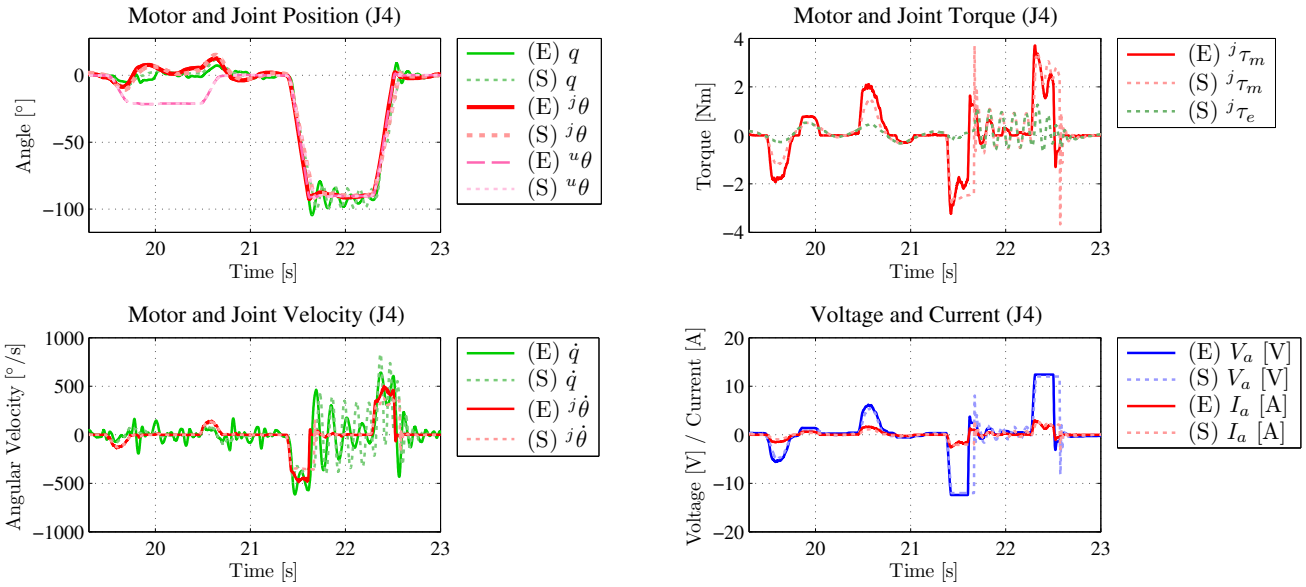

Figure 3.24.: Comparison of experimental (E) and simulation (S) data of joint four of the undamped excitation trajectory. The upper plot compares the joint position q with the reflected motor position ${}^{j}\theta$ with respects to the joint space, which represent the joint equilibrium position. State ${}^{u}\theta$ represents the virtually reflected real motor position without the kinematic coupling, also with respect to the joint side. From $t = 16\,\mathrm{s}$ to $21\,\mathrm{s}$ the joint equilibrium position ${}^{j}\theta$ is held relatively constant, while the motion of the real motor trajectory ${}^{u}\theta$ is necessary to compensate for the movement of the third joint. The lower plot compares the input states of the system, the motor armature current i_a and voltage u_a.

This is caused by the static motor friction in the hardware that cancels out motor torque response to small load oscillations. Because medium and high speed trajectories show good matching, as described in the following section, it can be stated that the deviation in motor torque occurs mostly in the case of steady motor state and the model shows good results in other cases.

3.6.2 Validation of the Identified Model

To rule out overfitting with the single joint exciting trajectory in the identification process in Figure 3.6.1, the identified model of the robot arm is validated against a medium speed pick-and-place trajectory as shown in Figure 3.25 and a randomly generated high speed trajectory with Cartesian end-effector velocities of up to $6\,\mathrm{m/s}$ as shown in Figure 3.28.

The comparison of simulation and experimental measurements of the states of the second joint are plotted in Figure 3.26 and 3.28. For the pick-and-place trajectory, a full state space controller on joint level with gravity compensation was used [36]. The high speed trajectory was fully feedforward controlled.

Table 3.8 lists the standard deviation of the simulated model errors compared to the experimental data for both validation trajectories. Simulation and experiment show good agreement. The comparison shows that no overfitting with the identification trajectory occurred and that the identified model shows good overall matching of the robot arm and actuators hardware.

Table 3.8.: Standard model error deviation of the validation trajectories.

Joint	1	2	3	4
	Pick-and-Place Trajectory			
σ_q [°]	1.6	1.2	3.4	1.7
σ_{u_a} [V]	0.58	0.28	0.35	0.89
σ_{i_a} [A]	0.35	0.21	0.19	0.40
	Undamped Excitation Trajectory			
σ_q [°]	2.3	2.1	2.9	2.7
σ_{u_a} [V]	0.53	0.78	0.74	1.2
σ_{i_a} [A]	0.28	0.65	0.50	0.47

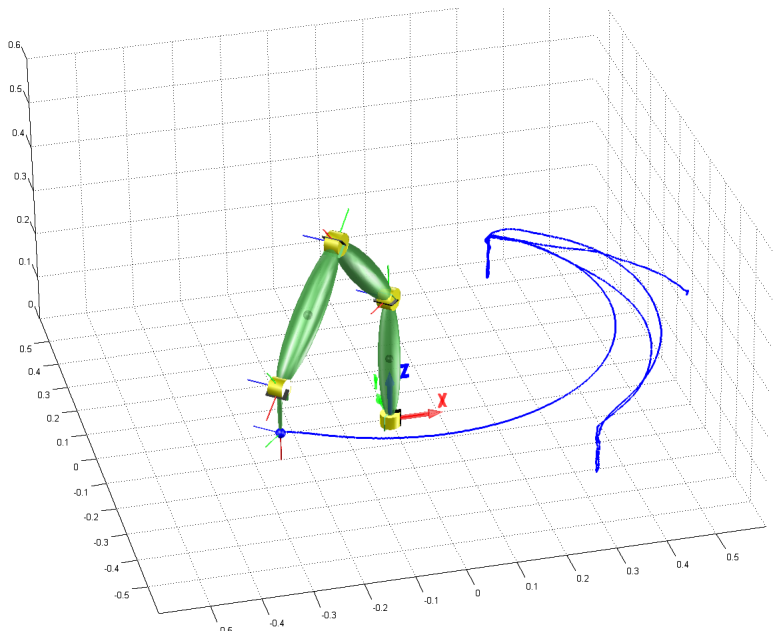

Figure 3.25.: Pick-and-place trajectory used for validation of the identification results. The trajectory data shown is experimental data generated on the BioRob-X4 robot hardware.

Some deviations occur in case of a steady state motor position and joint oscillations, where the motor torque ${}^{\mathrm{j}}\tau_{\mathrm{m}}$ displays more oscillations response in simulation than in experiment. For example, the simulation output deviates from the hardware measurements in the pick-and-place trajectory where the negative voltage values from simulation are higher than the measured voltage values, as can be seen in the voltage and current plot in Figure 3.26. This is not the case for the high speed trajectory, as can be seen in the voltage and current plot in Figure 3.28. The reason for this deviation is the friction model not taking tendon and static friction into consideration. The behavior is caused by the static motor friction in the hardware that cancels

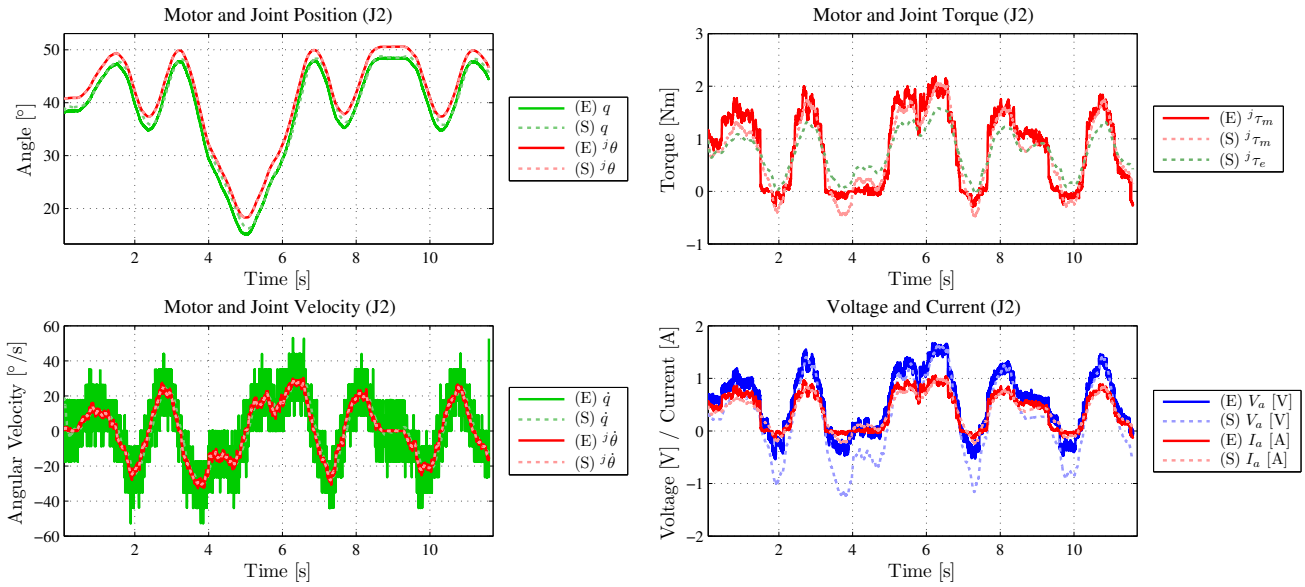

Figure 3.26.: Validation of the states of the second joint of the identified model using a pick-and-place trajectory.

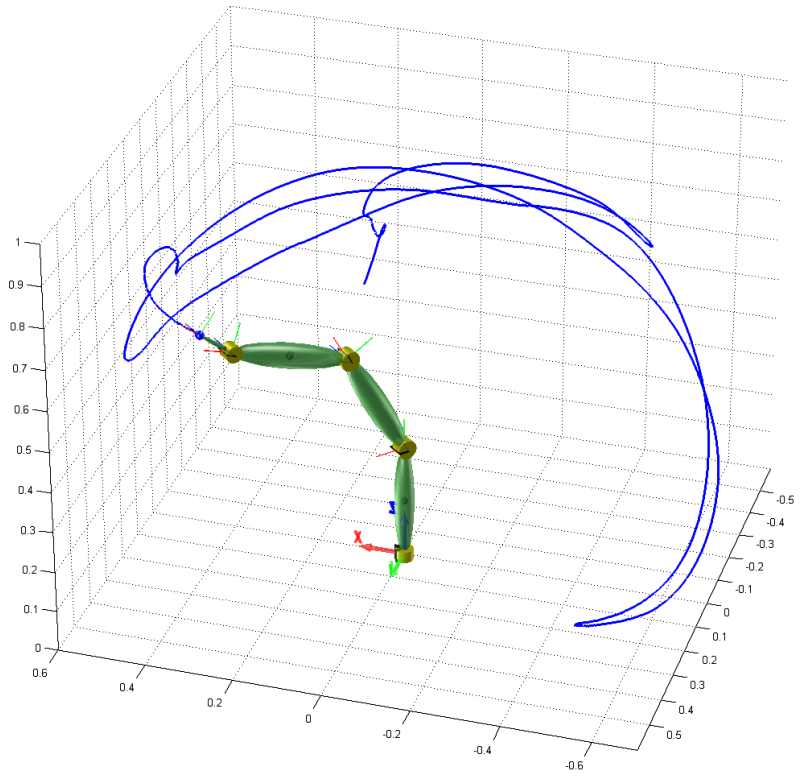

Figure 3.27.: Fast, random trajectory with end-effector velocities of up to 6 m/s used for validation of the identification results. The trajectory data shown is experimental data generated on the BioRob-X4 robot hardware.

out motor torque response to small load oscillations. Using a more complex motor and gearbox friction model could therefore further improve the model quality.

Similar to the effects of the basic friction model as mentioned in Section 3.6.1, where the motor torque is exaggerated by simulation in case of a steady motor position and joint oscillations, here

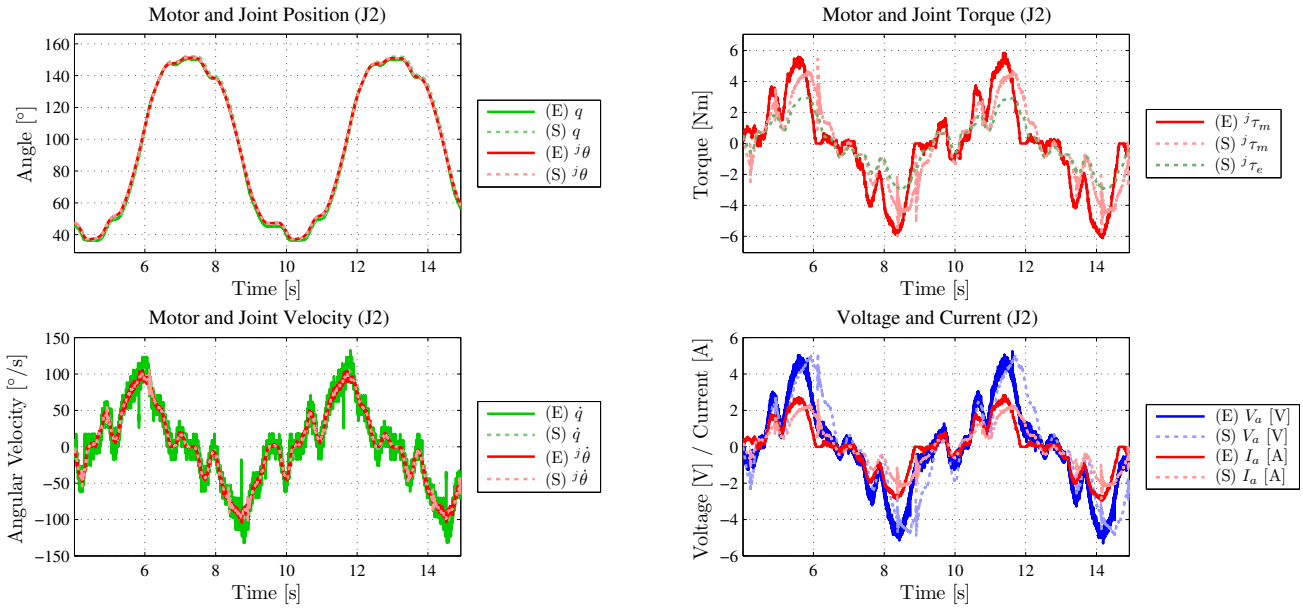

Figure 3.28.: Validation of the states of the second joint of the identified model using a fast, random trajectory with end-effector velocities of up to 6 m/s.

the voltage values are exaggerated by simulation in case of zero motor torque. Apart for the mentioned exceptions, the simulation model matches the experimental data of the robot arm very well in both the mechanical as well as in the electrical states.

4 Dynamic Analysis and Control

A preliminary version of Sections 4.3.1 to 4.3.3 was published in: Proceedings of the 41st International Symposium on Robotics / 6th German Conference on Robotics 2010 [35], and in: Simulation, Modeling, and Programming for Autonomous Robots, ser. Lecture Notes in Artificial Intelligence 2010 [36].

4.1 Observers and Sensor Data Filtering

4.1.1 Joint Position Calibration

The quality of the measured joint position is essential for all model-based methods. To enhance the sensor readings for the compact, custom-tailored joint sensor, a calibration method was developed based on velocity-based separation of zero-gravity measurement data to take the hysteresis effects into account. The separated sets are then filtered with local polynomial regression. With this calibration method, smooth joint measurement without hysteresis effects are obtained.

Because the sensors can become decalibrated in the assembled robot arm, an online calibration method is required. The underlying idea is to use the readings ${}^{\mathrm{j}}\boldsymbol{\theta}$ from the reliable motor sensors reflected to the joint side to determine the errors $\boldsymbol{q}_{\mathrm{error}}$ of the joint position sensor readings $\boldsymbol{q}_{\mathrm{S}}$

$$\boldsymbol{q}_{\mathrm{error}} = {}^{\mathrm{j}}\boldsymbol{\theta} - \boldsymbol{q}_{\mathrm{S}} \tag{4.1}$$

This approach is only valid if all external torques can be compensated. In order to cancel out gravitational effects, the measurements are made under zero-gravity conditions. Figure 4.1 shows the horizontal mounting of the robot arm for calibration measurements for joints two to

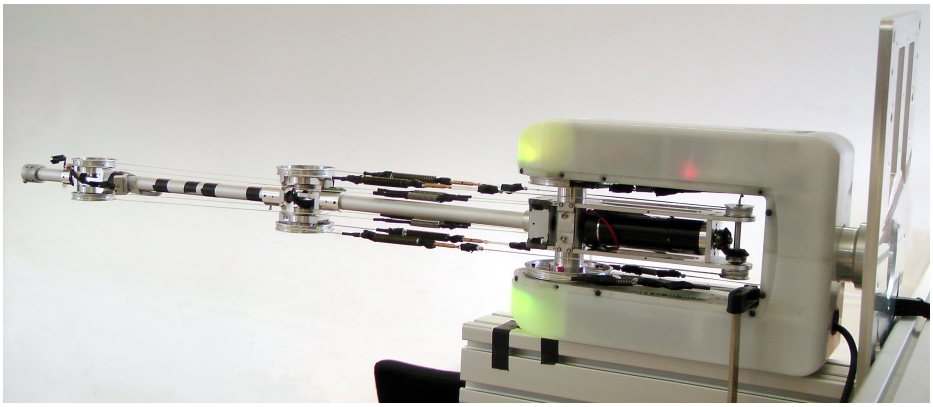

Figure 4.1.: Horizontal mounting of the robot arm for zero gravity measurements used for the calibration of the joint sensors of joint two to four.

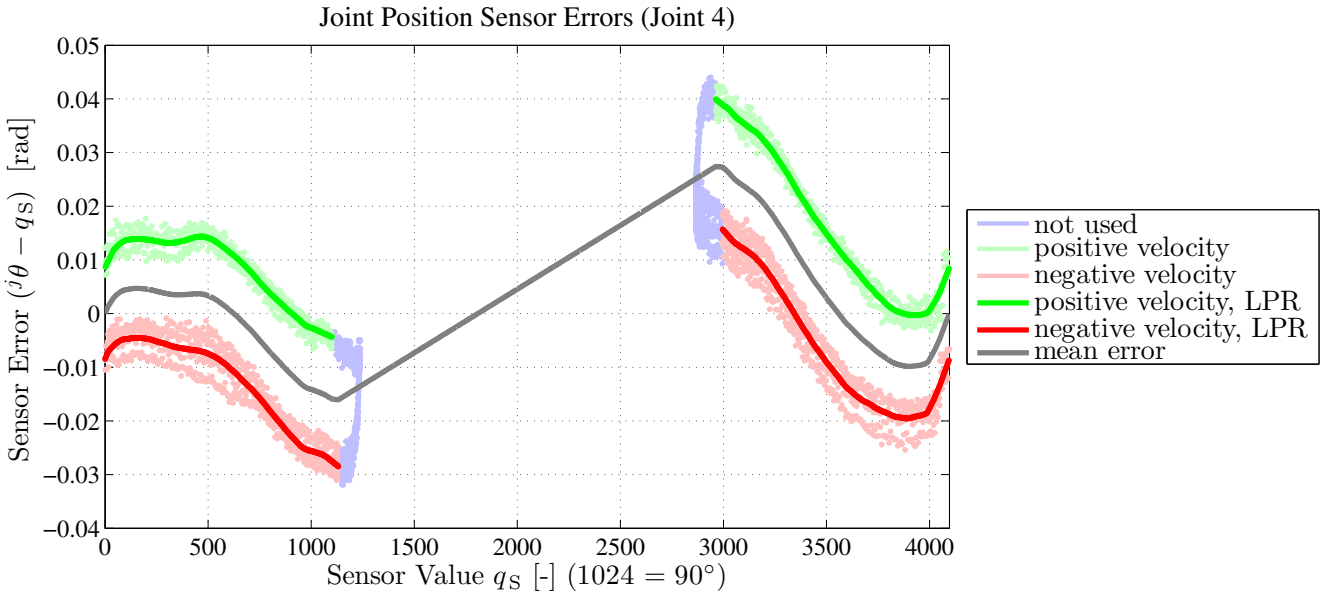

Figure 4.2.: Calibration data for the joint sensor of the fourth joint. The sensor values q_S are stored as unsigned values between 0 and 4096. Data for positive (green) and negative (red) joint velocity direction is treated separately and filtered with a two-sided local polynomial regression (LPR) filter. Values measured at very low velocities are of low confidence and not used (light blue). The calibration data (grey) is calculated as the mean value of the positive and negative direction data.

four. To avoid inertial and kinetic frictional effects, the calibration measurements are made for each joint separately over the entire joint range.

Most difficult to cope with are effects caused by static friction, such as hystereses. These are especially dominant if the velocity of the joint calibration measurements is too low, in which case stick-slip effects and joint oscillations can occur. To avoid this, a calibration trajectory with a constant velocity above the critical stick-slip joint velocity is defined, which can be determined by experiment. By this, a constant tension in the tendon built-in elasticity is achieved. The result is a hysteresis, as displayed in Figure 4.2.

The measurements of both hysteresis branches can be separated by defining positive (green point cloud in Figure 4.2) and negative (red point cloud) joint velocity measurements. These point clouds are then filtered with a local polynomial regression (LPR) and combined by calculating the mean value (grey line) of the interpolated, LPR filtered data.

The presented method cancels out all gravitational, inertial, and static and dynamic frictional effects and yields suitable calibration data for the joint sensors. Experimental validation of this calibration method showed that the absolute end-effector accuracy could be increased by more than 1 cm. Certainly, this value depends on the calibration state of the joint sensors.

4.1.2 Joint Velocity Filtering

In case of the investigated BioRob-X4 robot arm, very high joint velocities can occur. The first reason is the lightweight link design enabling high acceleration. The second reason is the decoupling of motor and joint by the elastic tendon actuators.

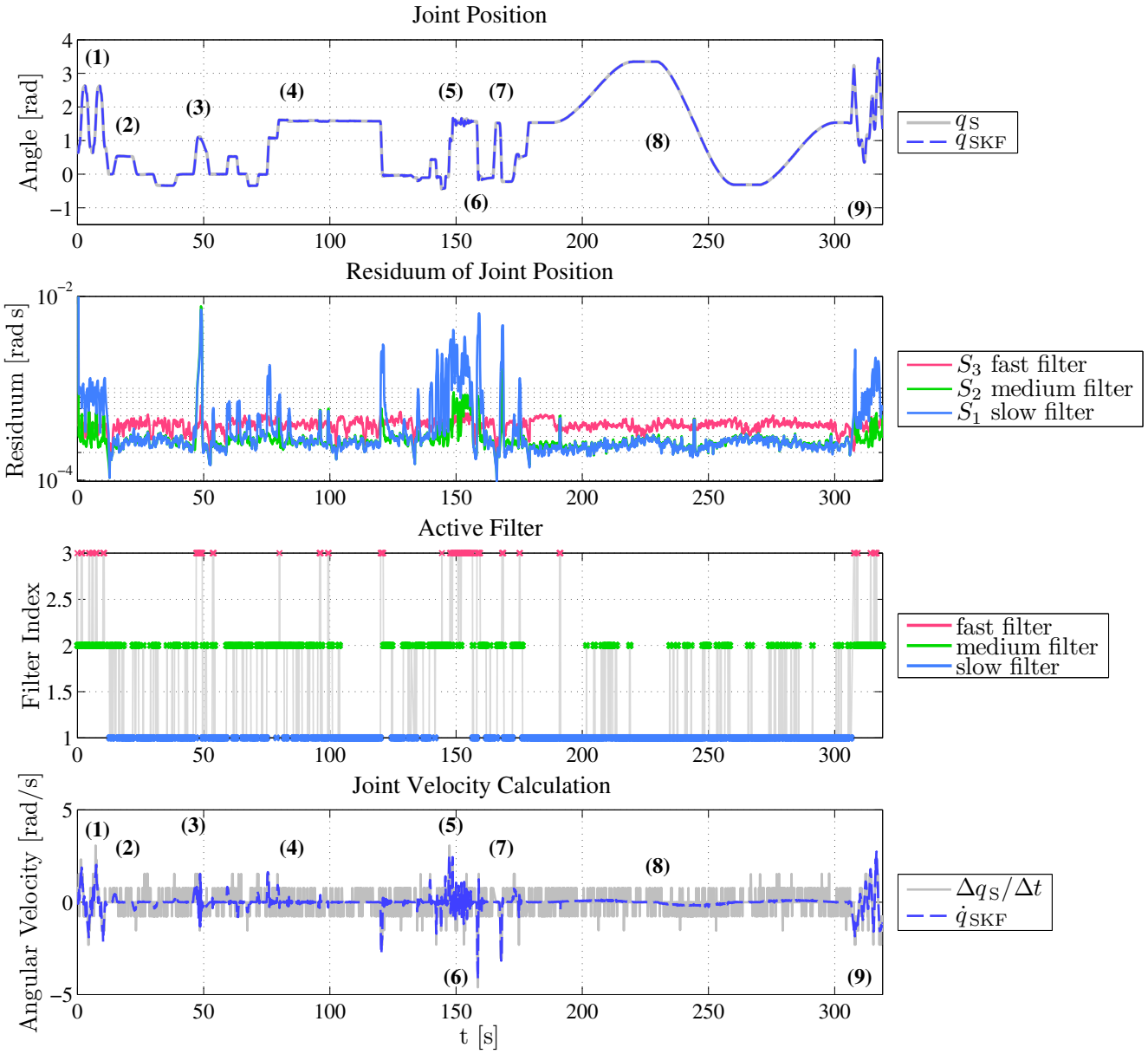

Figure 4.3.: Composed reference trajectories for validation of joint velocity filtering using a switching Kalman filter with three parallel filters: $n = 1$ optimized for steady state, $n = 2$ for medium and $n = 3$ for fast velocities. The quadratic residuum sums S_n are calculated using the last $N = 500$ measurements with sampling time $T = 10^{-3}$ s. The numerical differentiation of the joint sensor values yields a velocity signal with a very high noise level, as can be seen in the lowest plot (grey). Notable trajectory segments are (1) high speed trajectory with 2 rad/s, (2) fast slopes followed by constant segments, (3) fast slope with 1 rad/s and following destabilized high frequency oscillations, (4) externally excited natural frequency oscillations, (5) strong oscillations, (6-7) high speed collision trajectory with up to 4 rad/s impact velocity, (8) low velocity trajectory with 0.7 rad/s, and (9) high speed trajectory with 2.5 rad/s.

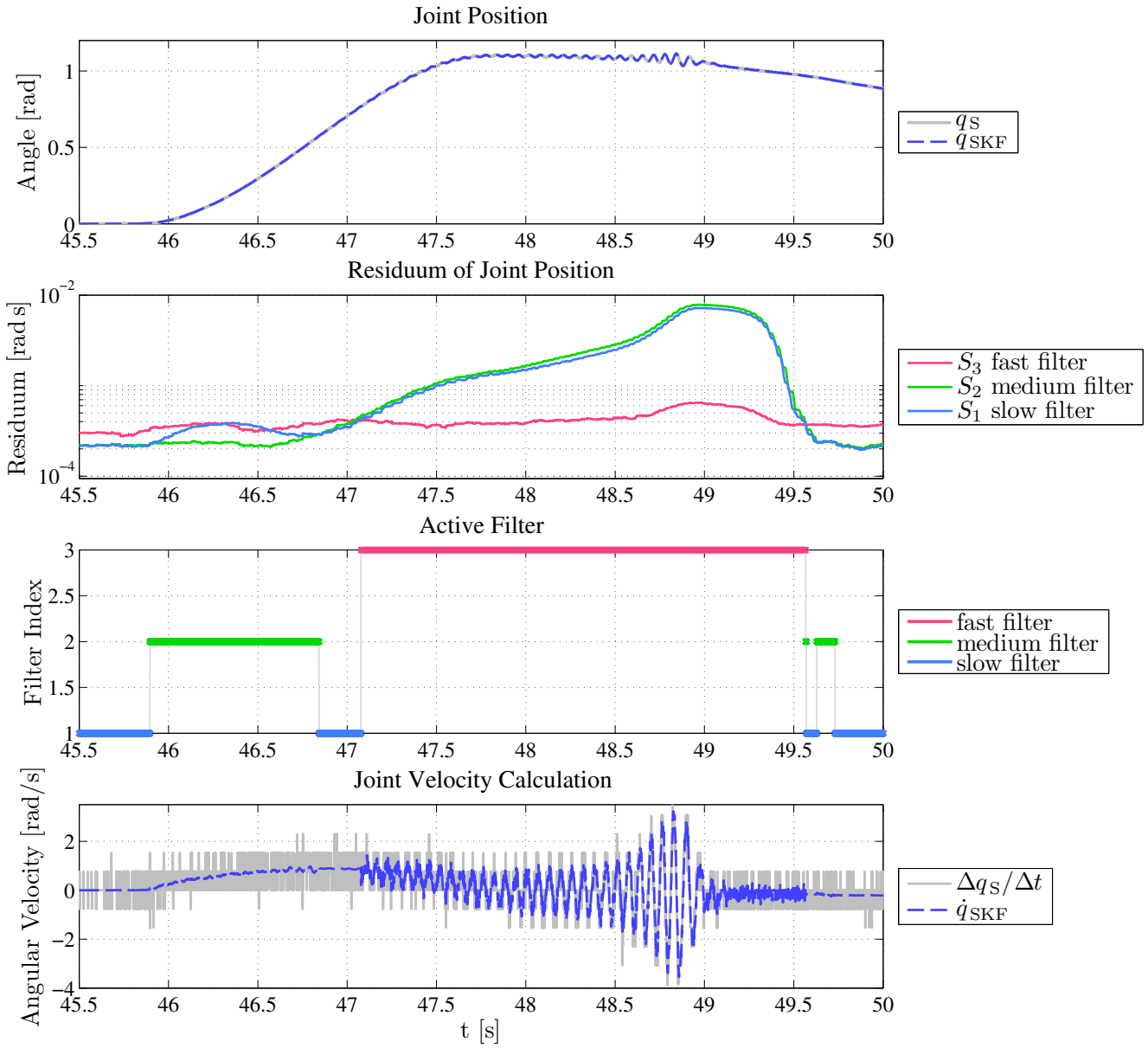

Figure 4.4.: Joint velocity filtering using a switching Kalman filter. Zoom on area (3) of Figure 4.3 with deliberately destabilized controller to test fast oscillation filter response.

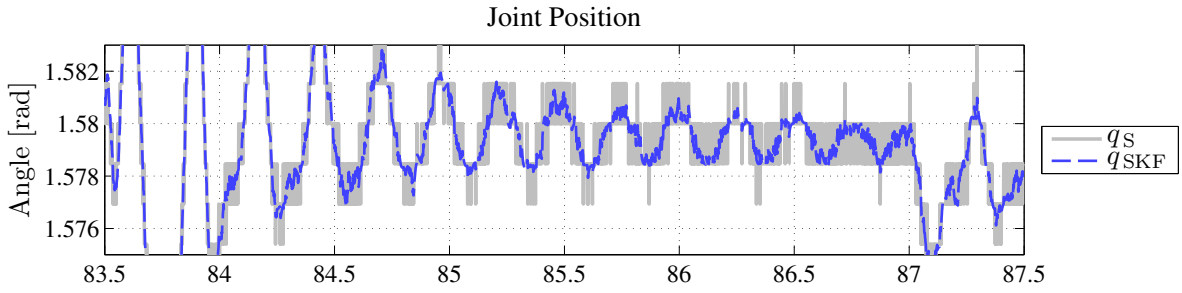

Figure 4.5.: Joint velocity filtering using a switching Kalman filter. Zoom on area (4) of Figure 4.3 with a decaying oscillation with a maximum angular velocity of about $0.01\,^{\mathrm{rad}}/_{\mathrm{s}}$ at $t = 86\,\mathrm{s}$. Without filtering, the velocity resolution is $0.767\,^{\mathrm{rad}}/_{\mathrm{s}}$. With filtering, oscillations with an angular velocity of $10^{-3}\,^{\mathrm{rad}}/_{\mathrm{s}}$ can be detected.

Because of the gearbox and transmission reduction ratios the motor velocity can be calculated from the motor position sensor readings by simple numeric differentiation with optional low pass filter smoothing with a small time constant. In contrast, the joint velocity calculation by numerical differentiation introduces a large amount of noise (cf. angular velocity plot in Figure 4.3, grey signal), rendering the joint velocity unusable for control.

When using a single filter, such as a low pass filter or a Kalman filter, for the joint velocity signal, the filter must not introduce a delay that can destabilize the controller. Therefore, a single filter must be optimized to work with high velocity oscillations. The result is a poor smoothing and noise reduction performance.

For this reason, a switching filter is proposed, compromised of several filters optimized for different velocities. The switching condition for activating the appropriate filter is based on the minimal error of the estimated position of each filter compared to the measured position over a finite horizon. The output of the filter with the lowest quadratic sum S_n of the position residual r_n of filter n over the latest N measurements is chosen

$$\min_n \Big(S_n = \sum_{i=k-N}^{k} r_n(i)^2 \left(t(i) - t(i-1) \right)^2 \Big), \tag{4.2}$$

with residual r_n being the difference between the measured joint position q_S and the position estimation of Kalman filter n

$$r_n = q_\mathrm{S} - q_{\mathrm{KF}_n} \tag{4.3}$$

A switching filter with three parallel Kalman filters was designed. The filters were optimized for steady state, medium and fast velocities. For validation, a reference trajectory was composed consisting of several measurements. Figure 4.3 shows the entire reference trajectory. A close-up of areas (5) and (6) is provided in Figure 4.5.

4.2 Review of Control Methods for Elastic Joint Robots in Joint Space

As a nonlinear flat system, the dynamics equations of a an elastic joint can be linearized by feedback control. By defining the state space variables

$$\boldsymbol{x} = \begin{bmatrix} \theta \\ \dot{\theta} \\ q \\ \dot{q} \end{bmatrix}; \qquad \dot{\boldsymbol{x}} = \begin{bmatrix} \dot{\theta} \\ \ddot{\theta} \\ \dot{q} \\ \ddot{q} \end{bmatrix}; \qquad y = q \tag{4.4}$$

the following state space model is obtained

$$\begin{aligned} \dot{\boldsymbol{x}} &= \begin{bmatrix} \dot{\theta} \\ -\frac{k}{J_m}(\theta - q) \\ \dot{q} \\ \frac{k}{J}(\theta - q) - \frac{b}{J}\dot{q} - \frac{mgl}{J}\cos(q) \end{bmatrix} + \begin{bmatrix} 0 \\ \frac{1}{J_m} \\ 0 \\ 0 \end{bmatrix} \tau_m \\ y &= \begin{bmatrix} 0 & 0 & 1 & 0 \end{bmatrix} \boldsymbol{x} \end{aligned} \tag{4.5}$$

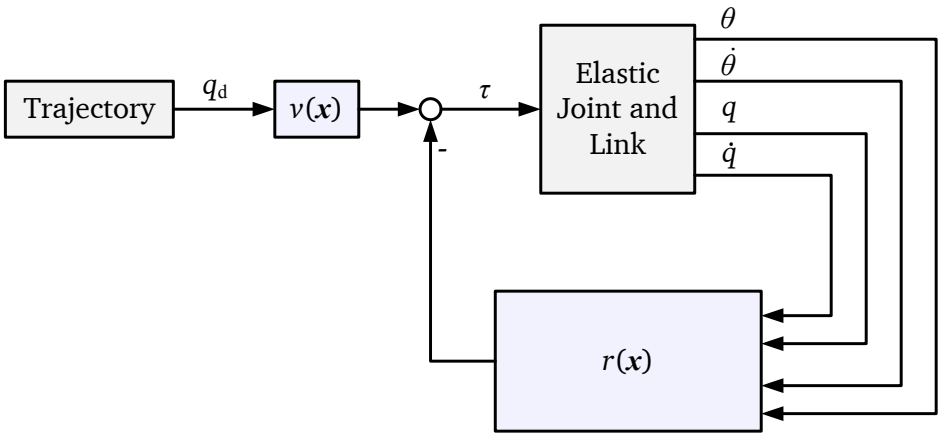

Figure 4.6.: Linearization control structure of an elastic joint.

The resulting model is a single input single output (SISO) system that is nonlinear in $\boldsymbol{x}$, but linear in u:

$$\begin{aligned} \dot{\boldsymbol{x}} &= \boldsymbol{a}(\boldsymbol{x}) + \boldsymbol{b}(\boldsymbol{x})\, u \\ y &= c(\boldsymbol{x}) \end{aligned} \tag{4.6}$$

with

$$\boldsymbol{a}(\boldsymbol{x}) = \begin{bmatrix} \dot{\theta} \\ -\frac{k}{J_m}(\theta - q) \\ \dot{q} \\ \frac{k}{J}(\theta - q) - \frac{b}{J}\dot{q} - \frac{mgl}{J}\cos(q) \end{bmatrix}; \qquad \boldsymbol{b}(\boldsymbol{x}) = \begin{bmatrix} 0 \\ \frac{1}{J_m} \\ 0 \\ 0 \end{bmatrix} \tag{4.7}$$

$$c(\boldsymbol{x}) = q$$

The resulting control structure is depicted in Figure 4.6 with the feedback control law

$$r(\boldsymbol{x}) = \frac{L_a^4 c(\boldsymbol{x}) + a_3 L_a^3 c(\boldsymbol{x}) + a_2 L_a^2 c(\boldsymbol{x}) + a_1 L_a^1 c(\boldsymbol{x}) + L_a^0 c(\boldsymbol{x})}{L_b L_a^{\delta-1} c(\boldsymbol{x})} \tag{4.8}$$

and the prefilter

$$v(\boldsymbol{x}) = \frac{J\, J_m\, a_0}{k} \tag{4.9}$$

Using the feedback linearization controller, the system is transformed into a time-delayed system of order four

$$G(s) = \frac{a_0}{s^4 + a_3 s^3 + a_2 s^2 + a_1 s + a_0}\,, \tag{4.10}$$

which parameters a_i can be chosen using pole placement.

The advantage of this controller is the systematic approach to obtain the controller equation. For higher order systems, however, the procedure can result in a rather complex control law. Also, the controller has to be recalculated for each change in the dynamics model.

For elastic joint robot arms, a general solution was derived [11], assuming differentiability of the joint side dynamics equations, including the joint friction.

Disadvantageous properties of the feedback linearization are low robustness with respect to model errors and the difficulty to consider constraints such as limitation or saturation of inner state variables.

4.3 Inverse Dynamics Model Control in Joint Space

4.3.1 Inverse Dynamics Model

For sufficiently high (but still finite) joint stiffness K_e, a singular perturbation model can be used [43]. The controller design consist of a cascade of fast joint level controllers that virtually make the joints stiff, and a slow upper controller for the dynamics.

The joint stiffness of the BioRob manipulator, however, is too low for this approach. A single joint cascade control would lead to a vast decrease in control performance and to a very slow tracking controlled system, as the singular perturbation controller relies on the joint level controllers to virtually remove the joint elasticity. In addition, for contact applications it is not desirable to remove the joint elasticity by cascaded controllers.

Instead, the inverse model is used to derive the control law. Because of hardware limitations concerning torque control, the control approach for the BioRob arm aims at model-based calculation of the desired motor trajectories $\boldsymbol{\theta}_\mathrm{d}$. In addition to the inverse model of elastic joint robots [10], the kinematic tendon coupling has to be considered for the investigated robot arm.

The calculation of computed torque for a given trajectory $\boldsymbol{q}_\mathrm{d}(t)$ is more difficult for elastic joints, because the motor trajectories $\boldsymbol{\theta}(t)$ are not known. With the desired link trajectory $\boldsymbol{q}(t)$ the desired joint torques $\boldsymbol{\tau}_\mathrm{d}$ can be calculated using computed torque for the rigid link structure

$$^{\mathrm{j}}\boldsymbol{\tau}_{\mathrm{e,d}} = \boldsymbol{M}(\boldsymbol{q}_\mathrm{d})\,\ddot{\boldsymbol{q}}_\mathrm{d} + \boldsymbol{C}(\boldsymbol{q}_\mathrm{d}, \dot{\boldsymbol{q}}_\mathrm{d})\,\dot{\boldsymbol{q}}_\mathrm{d} + \boldsymbol{D}\,\dot{\boldsymbol{q}}_\mathrm{d} + \boldsymbol{g}(\boldsymbol{q}_\mathrm{d}) \tag{4.11}$$

The desired elastic actuator torques are obtained by transforming the desired joint torques $\boldsymbol{\tau}_\mathrm{d}$ to the elastic actuator output state space

$$\boldsymbol{\tau}_{\mathrm{e,d}} = \boldsymbol{J}_\mathrm{t}^{\top\,\mathrm{j}}\boldsymbol{\tau}_{\mathrm{e,d}} \tag{4.12}$$

In case of the BioRob-X4 arm without tendon sliding and therefore moderate tendon friction, the damping terms in the equation of the elastic actuator torques

$$\boldsymbol{K}_\mathrm{e}\,(^{\mathrm{e}}\boldsymbol{\theta}_\mathrm{d} - {}^{\mathrm{e}}\boldsymbol{q}_\mathrm{d}) \;+\; \boldsymbol{D}_\mathrm{e}\,(^{\mathrm{e}}\dot{\boldsymbol{\theta}}_\mathrm{d} - {}^{\mathrm{e}}\dot{\boldsymbol{q}}_\mathrm{d}) \;=\; \boldsymbol{\tau}_{\mathrm{e,d}} \tag{4.13}$$

can be neglected. From this, the desired motor trajectory can be calculated as

$$^{\mathrm{e}}\boldsymbol{\theta}_\mathrm{d} = \boldsymbol{K}_\mathrm{e}^{-1}\,\boldsymbol{\tau}_{\mathrm{e,d}} + {}^{\mathrm{e}}\boldsymbol{q}_\mathrm{d}\,, \tag{4.14}$$

and transformation of the computed torque $\boldsymbol{\tau}_{\mathrm{e,d}}$ and the desired joint trajectory $\boldsymbol{q}_d$ to joint state space and transformation of the motor trajectory $\boldsymbol{\theta}$ to the motor state space yields

$$\boldsymbol{\theta}_{\mathrm{d}} = \boldsymbol{J}_{\mathrm{g}}^{-1}\,\boldsymbol{K}_{\mathrm{e}}^{-1}\,\boldsymbol{J}_{\mathrm{t}}^{\top\,\mathrm{j}}\boldsymbol{\tau}_{\mathrm{e,d}} + \boldsymbol{J}_{\mathrm{g}}^{-1}\,\boldsymbol{J}_{\mathrm{t}}^{-1}\,\boldsymbol{q}_{\mathrm{d}} \tag{4.15}$$

and with the computed torque from (4.11)

$$\boldsymbol{\theta}_{\mathrm{d}} = \boldsymbol{J}_{\mathrm{g}}^{-1}\,\boldsymbol{K}_{\mathrm{e}}^{-1}\,\boldsymbol{J}_{\mathrm{t}}^{\top}\left(\boldsymbol{M}(\boldsymbol{q}_{\mathrm{d}})\,\ddot{\boldsymbol{q}}_{\mathrm{d}} + \boldsymbol{C}(\boldsymbol{q}_{\mathrm{d}},\dot{\boldsymbol{q}}_{\mathrm{d}})\,\dot{\boldsymbol{q}}_{\mathrm{d}} + \boldsymbol{D}\,\dot{\boldsymbol{q}}_{\mathrm{d}} + \boldsymbol{g}(\boldsymbol{q}_{\mathrm{d}})\right) + \boldsymbol{J}_{\mathrm{g}}^{-1}\,\boldsymbol{J}_{\mathrm{t}}^{-1}\,\boldsymbol{q}_{\mathrm{d}} \tag{4.16}$$

The desired motor torques $\boldsymbol{\tau}_m$ can then be calculated using the mechanical motor dynamics equation (3.114):

$$\boldsymbol{\tau}_{\mathrm{m,d}} = \boldsymbol{I}_{\mathrm{m}}\,\ddot{\boldsymbol{\theta}}_{\mathrm{d}} + \boldsymbol{D}_{\mathrm{m}}\,\dot{\boldsymbol{\theta}}_{\mathrm{d}} + \boldsymbol{J}_{\mathrm{g}}\,\boldsymbol{\tau}_{\mathrm{e,d}}\,, \tag{4.17}$$

and with (4.12)

$$\boldsymbol{\tau}_{\mathrm{m,d}} = \boldsymbol{I}_{\mathrm{m}}\,\ddot{\boldsymbol{\theta}}_{\mathrm{d}} + \boldsymbol{D}_{\mathrm{m}}\,\dot{\boldsymbol{\theta}}_{\mathrm{d}} + \boldsymbol{J}_{\mathrm{g}}\boldsymbol{J}_{\mathrm{t}}^{\top}\left(\boldsymbol{M}(\boldsymbol{q}_{\mathrm{d}})\,\ddot{\boldsymbol{q}}_{\mathrm{d}} + \boldsymbol{C}(\boldsymbol{q}_{\mathrm{d}},\dot{\boldsymbol{q}}_{\mathrm{d}})\,\dot{\boldsymbol{q}}_{\mathrm{d}} + \boldsymbol{D}\,\dot{\boldsymbol{q}}_{\mathrm{d}} + \boldsymbol{g}(\boldsymbol{q}_{\mathrm{d}})\right) \tag{4.18}$$

This result shows that the computed motor torque $\boldsymbol{\tau}_{\mathrm{m,d}}$ requires the desired motor acceleration $\ddot{\boldsymbol{\theta}}_{\mathrm{d}}$, which in turn uses the desired joint acceleration $\ddot{\boldsymbol{q}}_{\mathrm{d}}$, cf. (4.21). The computed motor torque therefore uses the fourth derivative of the desired joint trajectory.

4.3.2 Controller with Tendon Decoupling and Gravity Compensation

The desired link trajectory $\boldsymbol{q}_{\mathrm{d}}$ and the desired motor trajectory $\boldsymbol{\theta}_{\mathrm{d}}$ (4.21) can be used for a full state space feedback controller as shown in Figure 4.7. Each elastic joint can be described by an ordinary differential equation of order four, so the complete state space controller needs the feedback of a state space vector of length four. The BioRob arm sensor system measures motor θ_i and joint q_i positions, so that following state space variables are chosen

$$\boldsymbol{x}^{\top} = \begin{pmatrix}\boldsymbol{q} & \dot{\boldsymbol{q}} & \boldsymbol{\theta} & \dot{\boldsymbol{\theta}}\end{pmatrix} \tag{4.19}$$

This representation has the advantage that only the first derivative of the joint and motor position is required, which can be obtained by numerical differentiation. The controller can also be implemented in joint space, rather than in motor space. In this case, the joint state space variables are used

$${}^{j}\boldsymbol{x}^{\top} = \begin{pmatrix}\boldsymbol{q} & \dot{\boldsymbol{q}} & {}^{\mathrm{j}}\boldsymbol{\theta} & {}^{\mathrm{j}}\dot{\boldsymbol{\theta}}\end{pmatrix} \tag{4.20}$$

A controller with tendon decoupling and gravity compensation can be obtained when using the gravity compensation torque of the link structure in (4.18) resulting in desired motor trajectory with respect to the motor state space

$$\boldsymbol{\theta}_{\mathrm{d}} = \boldsymbol{J}_{\mathrm{g}}^{-1}\,\boldsymbol{K}_{\mathrm{e}}^{-1}\,\boldsymbol{J}_{\mathrm{t}}^{\top}\,\boldsymbol{g}(\boldsymbol{q}_{\mathrm{d}}) + \boldsymbol{J}_{\mathrm{g}}^{-1}\,\boldsymbol{J}_{\mathrm{t}}^{-1}\,\boldsymbol{q}_{\mathrm{d}} \tag{4.21}$$

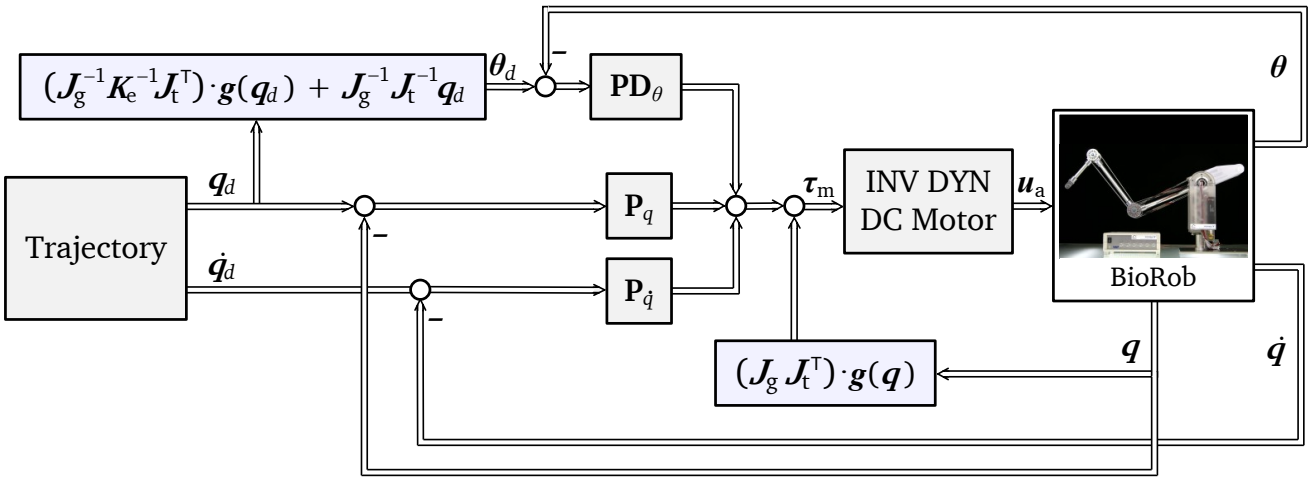

Figure 4.7.: Control structure using the inverse dynamics model with joint state vector $\boldsymbol{q}$. The inverse dynamics of the DC motor (INV DYN DC Motor) are given by (3.65).

In addition to the state space controller an approximation of a global gravitational compensation $\boldsymbol{g}(\boldsymbol{q})$ is used, which is exact in steady state. The feedforward motor torque therefore yields

$$\boldsymbol{\tau}_{\mathrm{m,d}} = \boldsymbol{I}_{\mathrm{m}}\,\ddot{\boldsymbol{\theta}}_{\mathrm{d}} + \boldsymbol{D}_{\mathrm{m}}\,\dot{\boldsymbol{\theta}}_{\mathrm{d}} + \boldsymbol{J}_{\mathrm{g}}\boldsymbol{J}_{\mathrm{t}}^{\top}\,\boldsymbol{g}(\boldsymbol{q}) \tag{4.22}$$

The desired motor velocity $\dot{\boldsymbol{\theta}}_{\mathrm{d}}$ and acceleration $\ddot{\boldsymbol{\theta}}_{\mathrm{d}}$ can be obtained from (4.21)

$$\dot{\boldsymbol{\theta}}_{\mathrm{d}} = \boldsymbol{J}_{\mathrm{g}}^{-1}\,\boldsymbol{K}_{\mathrm{e}}^{-1}\,\boldsymbol{J}_{\mathrm{t}}^{\top}\,\dot{\boldsymbol{g}}(\boldsymbol{q}_{\mathrm{d}},\dot{\boldsymbol{q}}_{\mathrm{d}}) + \boldsymbol{J}_{\mathrm{g}}^{-1}\,\boldsymbol{J}_{\mathrm{t}}^{-1}\,\dot{\boldsymbol{q}}_{\mathrm{d}} \tag{4.23}$$

$$\ddot{\boldsymbol{\theta}}_{\mathrm{d}} = \boldsymbol{J}_{\mathrm{g}}^{-1}\,\boldsymbol{K}_{\mathrm{e}}^{-1}\,\boldsymbol{J}_{\mathrm{t}}^{\top}\,\ddot{\boldsymbol{g}}(\boldsymbol{q}_{\mathrm{d}},\dot{\boldsymbol{q}}_{\mathrm{d}},\ddot{\boldsymbol{q}}_{\mathrm{d}}) + \boldsymbol{J}_{\mathrm{g}}^{-1}\,\boldsymbol{J}_{\mathrm{t}}^{-1}\,\ddot{\boldsymbol{q}}_{\mathrm{d}} \tag{4.24}$$

The first and second derivative $\dot{\boldsymbol{g}}$ and $\ddot{\boldsymbol{g}}$ of the gravitational torque vector can be calculated using technical computing software. It can be useful to express these derivatives with respect to the joint position state vector $\boldsymbol{q}$ instead of time. This can be done using the Jacobian $\boldsymbol{J}(\boldsymbol{g})(\boldsymbol{q})$ and the Hessian matrix $\boldsymbol{H}(g_1)(\boldsymbol{q})$ of the gravitational torque vector $\boldsymbol{g}$ and its scalar functions g_i, respectively, yielding

$$\dot{\boldsymbol{g}}(\boldsymbol{q}_{\mathrm{d}},\dot{\boldsymbol{q}}_{\mathrm{d}}) = \boldsymbol{J}(\boldsymbol{g})(\boldsymbol{q})\,\dot{\boldsymbol{q}} \tag{4.25}$$

$$\ddot{\boldsymbol{g}}(\boldsymbol{q}_{\mathrm{d}},\dot{\boldsymbol{q}}_{\mathrm{d}},\ddot{\boldsymbol{q}}_{\mathrm{d}}) = \begin{pmatrix} \dot{\boldsymbol{q}}^{\top}\boldsymbol{H}(g_1)(\boldsymbol{q})\,\dot{\boldsymbol{q}} \\ \vdots \\ \dot{\boldsymbol{q}}^{\top}\boldsymbol{H}(g_n)(\boldsymbol{q})\,\dot{\boldsymbol{q}} \end{pmatrix} + \boldsymbol{J}(\boldsymbol{g})(\boldsymbol{q})\,\ddot{\boldsymbol{q}} \tag{4.26}$$

Figure 4.7 shows the resulting controller structure. A system with torque input is assumed. Therefore, a fast inner control loop sensing the motor current (3.60) and controlling the desired torque by feeding the motors with voltage u has to be implemented. Optionally, the inverse motor model from Equation (3.59) and (3.60) can be used.

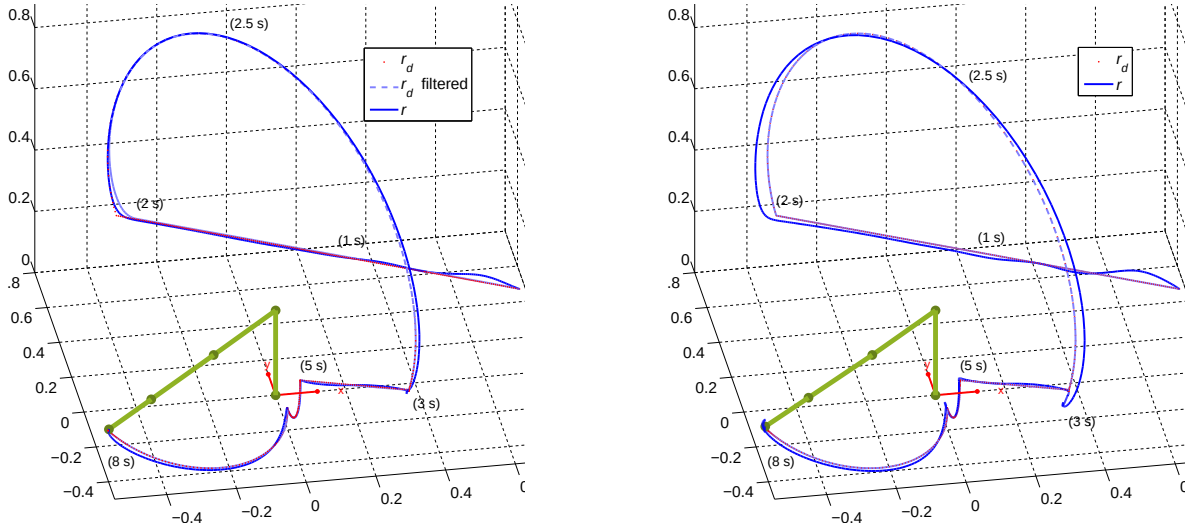

(a) Low pass filtering of the joint trajectory with $T_1 = T_2 = 0.05\,\mathrm{s}$

(b) Without trajectory filtering

Figure 4.8.: Effect of the joint trajectory low pass filtering.

4.3.3 Simulation Results

The trajectory used for evaluation of the controller is taken from a typical pick-and-place application as shown in Figure 4.11 and additionally consists of segments of linear motion in Cartesian space. The desired joint trajectories q_d were generated by cubic interpolation of joint trajectories calculated by inverse kinematics. These trajectories were then low pass filtered to receive trajectories that are four times derivable. Figure 4.8 shows the increased performance when using slight filtering. Critical trajectory points are smoothed ($t = 2\,\mathrm{s}$), whereas stationary points are preserved ($t = 3\,\mathrm{s}$).

Figure 4.9 shows how the joint sensor information is used for damping the oscillations caused by the joint elasticity. As can be seen in Figure 4.9a, good steady state accuracy can be obtained even if no joint information is available, provided an accurate steady state model.

To evaluate the robustness of the controller design with respect to modeling errors and external disturbances, model parameters of the simulation model were altered. Figure 4.10a shows the dynamic behavior of the robot arm with the same controller model parameters as in Figure 4.8, but an increase of end-effector mass and joint and motor friction by factor two. Apparently, the overall tracking control performance degrades, especially the damping behavior after the fast motion at $t = 3\,\mathrm{s}$. The controller is not able to prevent overshoot at high accelerations, but the overall performance is still robust. In Figure 4.10b, external forces were applied to the robot arm. The plot shows the desired compliant behavior of the robot arm in contact situations.

4.3.4 Experimental Results

The controller with gravity compensation described in Section 4.3.2 was implemented and experimentally evaluated on the BioRob-X4 robot arm. As a practical evaluation scenario, a pick-and-place application for handling of small aluminum parts was set up as described in

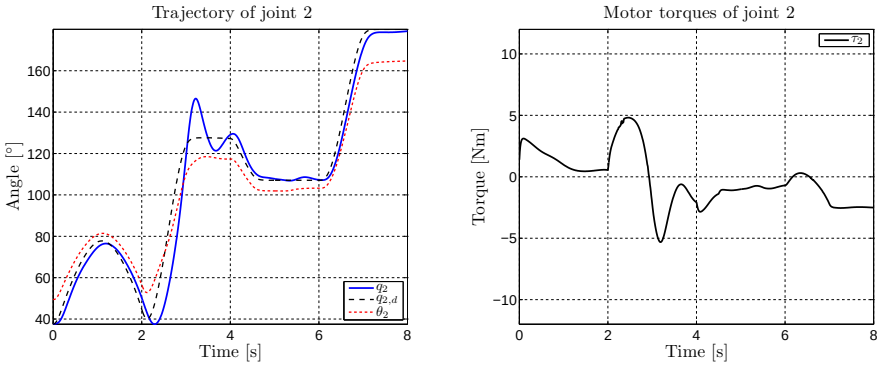

(a) Motor trajectory control without joint velocity damping.

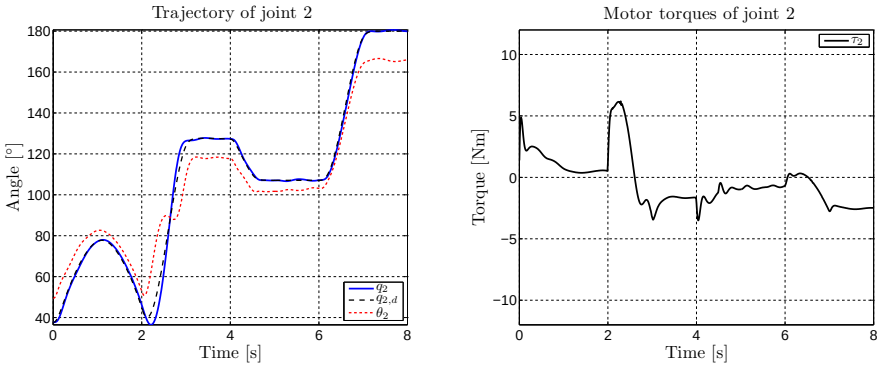

(b) Full state space control

Figure 4.9.: Comparison of the performance of (b) the full state space controller and (a) a reduced controller only using motor sensor information. The joint position is displayed in blue, the motor position in red.

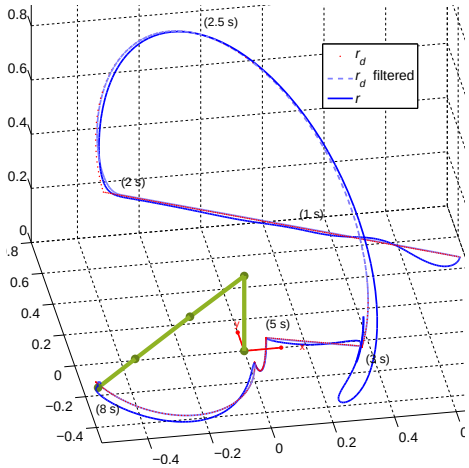

(a) Parameter changes: fourth link weight (doubled), joint and motor friction (doubled).

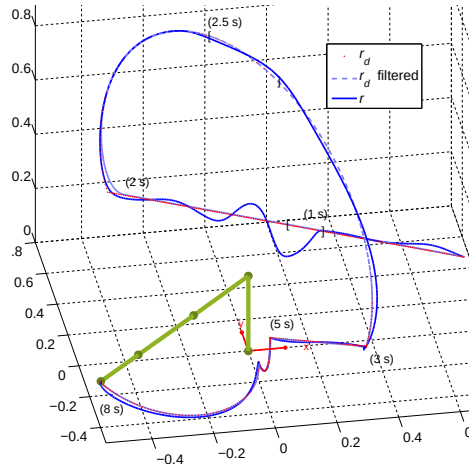

(b) External forces (marked with square brackets): 5 Nm applied on the second joint from 0.9 to 1.1 s and the on first joint from 2.5 to 2.6 s.

Figure 4.10.: Effect of modeling errors and disturbances on the control performance.

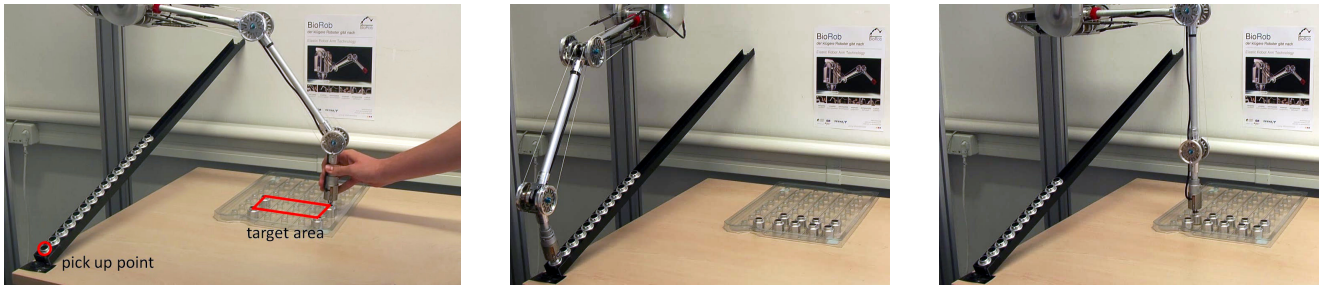

Figure 4.11.: Pick-and-place application using programming by demonstration with the BioRob robot arm. After teaching important points in task space (left) the control software can automatically generate trajectories to perform the pick-and-place task (middle and right) [35].

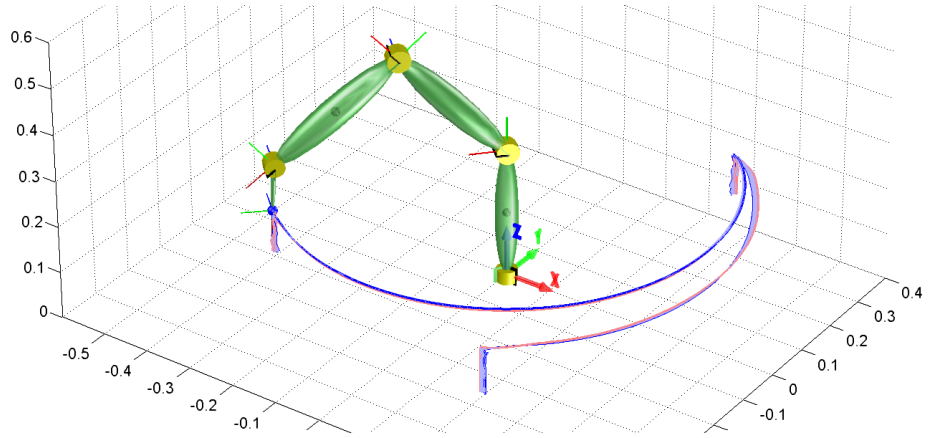

Figure 4.12.: Visualization of the experimental measurements of a pick-and-place trajectory with three picking and placing positions at $t_1 = 5\,\mathrm{s}$, $t_2 = 7.5\,\mathrm{s}$, and $t_3 = 10.25\,\mathrm{s}$. The red line is the desired Cartesian trajectory, the dark blue line the real robot end-effector trajectory. The error between both trajectories is marked in light blue.

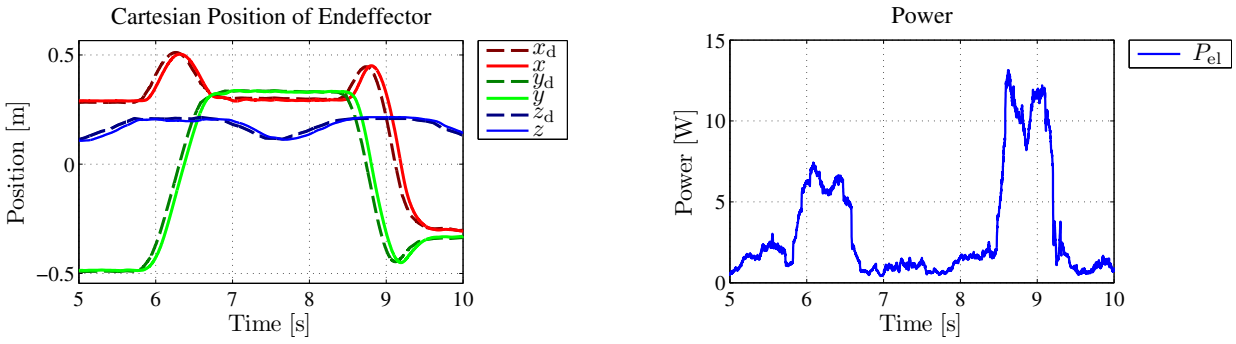

Figure 4.13.: Experimentally measured Cartesian end-effector trajectory (left) and the overall power consumption (right). At the second position at $t_2 = 7.5\,\mathrm{s}$ the remaining Cartesian error is $\|\boldsymbol{r}(t_2) - \boldsymbol{r}_\mathrm{d}(t_2)\| = 8.5\,\mathrm{mm}$. The maximum end-effector trajectory velocity $\dot{r}_4 = 1.97\,\mathrm{m/s}$ is reached at $t = 9.16\,\mathrm{s}$.

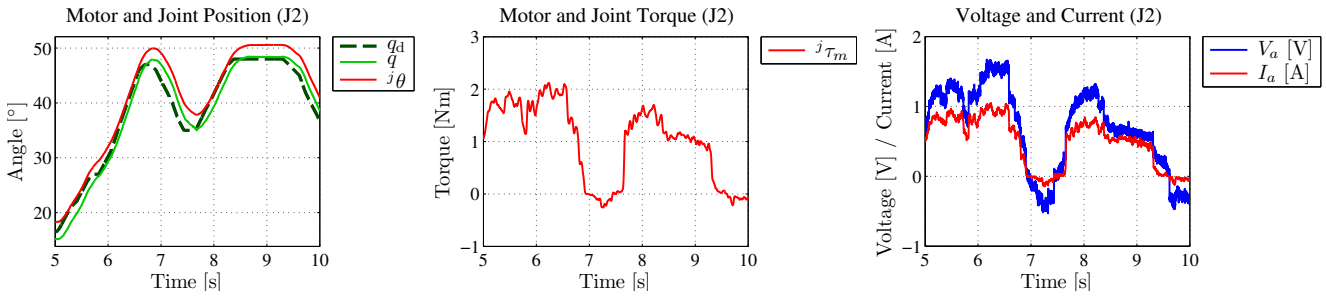

Figure 4.14.: Experimentally measured joint q and motor position θ (left), motor torque ${}^{\mathrm{j}}\tau_{\mathrm{m}}$ with respect to the joint side (middle), and motor current I_{a} and voltage V_{a} of the second joint.

Figure 4.11. For this pick and place application, the robot is operated in a suspended position, very much like a human arm attached to the shoulder. This results in a more human-like workspace and is possible because of the low arm weight.

The evaluated trajectory starts at the position at $t_1 = 5\,\mathrm{s}$, proceeds to the second position at $t_2 = 7.5\,\mathrm{s}$, and then reaches the final position at $t_3 = 10.25\,\mathrm{s}$. At each of these positions, the robot arm end-effector is lowered to pick or place a part. A visualization of the measured trajectory sensor data is given in Figure 4.13.

Figure 4.13 displays the Cartesian end-effector positions measurements of the robot arm under tracking control using the described trajectory. A maximum velocity of about $2\,\mathrm{m/s}$ is reached between the second and the third position. At the picking and placing positions a trajectory tracking error of 5 to 9 mm is achieved, which is sufficient for the presented application. The tracking error is higher during the acceleration and deceleration phases. The overall power consumption is very low. A peak power consumption of 13 W is reached during the acceleration phase. Figure 4.14 plots the states of the second joint.

5 Investigation of Safety in pHRI for Lightweight Robot Arms

5.1 Realistic Impact Modeling

The work presented in this Section was carried out in collaboration with Katayon Radkhah and was published in: Proceedings of the 15th International Conference on Advanced Robotics 2011 [37].

5.1.1 Introduction

Modeling dynamic contacts is a still quite challenging problem. A major contribution of this section is therefore the description of the newly developed contact model.

"A contact model should characterize both the forces that can be transmitted through the contact as well as the allowed relative motions of the contacting bodies. These characteristics are determined by the geometry of the contacting surfaces and the material properties of the parts which dictate friction and possible contact deformation" [27].

We consider point contacts, because plane contacts can be treated as multiple point contacts at the corners of the contact area. A point contact is described as a state machine that switches between normal force, kinetic and static friction. It can be attached to any point of a body. Figure 5.1a depicts the considered point contact model. For a realistic modeling of the dynamic properties, a finite surface A has to be assumed. L stands for the measured thickness of the contact layer. Collision forces, that are generated along the surface normal, are denoted as F_N. Tangential forces, that are caused by kinetic and static friction during a collision, are denoted as F_T.

Contact dynamics can be modeled by either penalty-based or analytical methods. Most analytical methods use optimization techniques to satisfy contact model conditions and produce relatively stable results even with large sampling time. However, optimization problems are often time-consuming and require simplification. In systems, where bouncing occurs more frequently than stick contacts, impulse-based methods are computationally more efficient than optimization problems. Based on the assumption of inelastic collisions, an iterative trial-and-error method is used in [70] to increase computational efficiency during stick contacts. Despite workarounds, a general disadvantage of analytical methods is that realistic impact and friction forces are difficult to predict. Also, it is possible that no solution or multiple solutions are found, and energy conservation principles may be violated in frictional impacts [67]. In contrast to analytical methods, penalty-based methods generate forces at the point contacts based on the elastic and viscous properties of the material [24, 42, 17]. They incorporate deformations and losses of energy and can easily be enhanced by friction models. The coupling of the colliding objects with a virtual spring damper system possibly results in a stiff system of ordinary differential equations, which requires smaller simulation step sizes. This, however, is necessary anyway, when analyzing not only the motions, but also the impact and friction forces and their effect on the joint torques of the system.

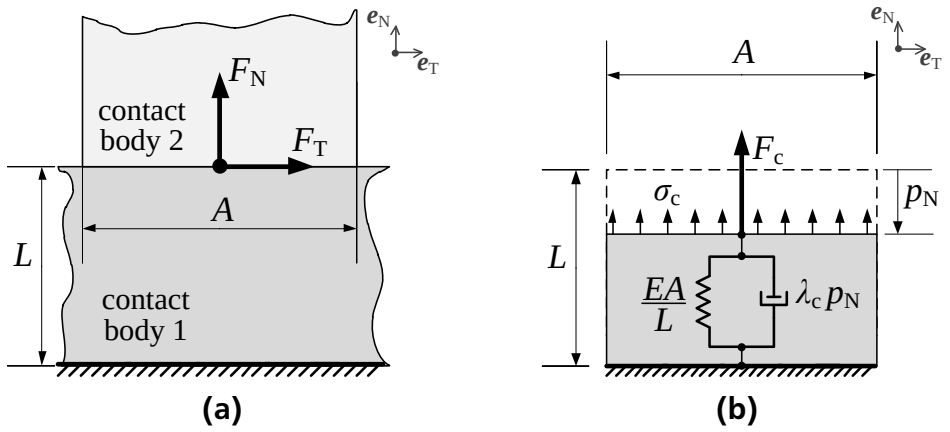

Figure 5.1.: Finite single point contact (a) and collision (b) model.

In this section, we explain how to model contacts that are able to predict realistic contact forces including kinetic and static friction by using a state machine. In addition, we elucidate how the parameters of this model can be calculated from the material properties of the colliding bodies. Note, that this model can be used in any MBS dynamics simulation tool that allows to introduce forces into a body and measure the position and velocity of a body.

5.1.2 Collision

Fig. 5.1a displays two contacting bodies in a relaxed state and the normal and tangential forces, F_N and F_T, respectively. Fig. 5.1b illustrates the collision model. The collision counterforce F_c is computed depending on the penetration p_N along the surface normal vector $\boldsymbol{e}_N$. As mentioned earlier, the contact body 1 is assumed to have a smooth contact surface of size A with an infinite extension (ground, wall, etc.), so that a geometric collision detection can be reduced to:

$$p_N = \boldsymbol{p}\boldsymbol{e}_N \,, \tag{5.1}$$

where p_N is the relative distance between the colliding objects and negative during collision, $p_N < 0$.

For small deformations the stiffness of the contact material can be described by a linear stress-strain curve with Young's modulus E of the contact material and the average normal stress σ_N. The normal strain ϵ_N can be approximated by the ratio of penetration p_N and total layer thickness L:

$$\sigma_N = E\,\epsilon_N = -E\,\frac{p_N}{L}\,. \tag{5.2}$$

Using the average stress, the compression force F_c is calculated as a function of compression and material stiffness k_c:

$$F_c = A\,\sigma_N = -k_{c1}\,p_N \quad \text{with} \quad k_{c1} = \frac{E\,A}{L}\,. \tag{5.3}$$

The stiffness of both colliding bodies, k_{c1} and k_{c2}, are merged into a single collision stiffness k_c:

$$k_c = \left(\frac{1}{k_{c1}} + \frac{1}{k_{c2}} \right)^{-1} . \tag{5.4}$$

Aside from the above description of the stiffness of the materials and the strain, it is also important to formulate the dynamic properties, i.e. elasticity of the collision. It is also referred to as coefficient restitution or bounciness of the collision [42]. The elasticity of a collision depends on the amount of dissipative energy lost during the impact. The most basic way is to model the contact surface as a visco-elastic Kelvin-Voigt material [15]. But, this model has several limitations, such as discontinuity of the contact force at the moment of impact, dependence of the coefficient of restitution on the mass of the impacting bodies and the lack of dependence on the impact velocity [42]. We therefore use the Hunt-Crossley model to extend (5.3) by a nonlinear damping component, which is comprised of the damping constant λ_c and the compression velocity $\dot{p}_N$, scaled by the penetration p_N [24]:

$$F_c = (\lambda_c \, p_N) \, \dot{p}_N - k_c \, p_N \, . \tag{5.5}$$

For the computation of the parameter λ_c, given certain prerequisites, please refer to [42]. An important property of the Hunt-Crossley model is that the contact forces are continuous upon impact, in contrast to the linear viscous damping model. Attracting forces ($F_c < 0$) only occur if the bodies are separated quickly by external forces. This can be interpreted such that the bodies lose contact because the relaxing speed of the compressed material is lower than the relative velocity of the bodies. For negative values of F_c, we therefore saturate $F_c = 0$:

$$\boldsymbol{F}_c = \begin{cases} \mathbf{0} & : \quad \dot{p}_N \geq \frac{k_c}{\lambda_c} \\ ((\lambda_c \, p_N) \, \dot{p}_N - k_c \, p_N) \boldsymbol{e}_N & : \quad \dot{p}_N < \frac{k_c}{\lambda_c} \end{cases} \tag{5.6}$$

5.1.3 Kinetic Friction

The direction of the friction force is the opposite of $\boldsymbol{e}_T$, which represents the direction of the relative contact velocity component perpendicular to the contact surface normal $\boldsymbol{e}_N$

$$\boldsymbol{e}_T = \frac{(\dot{\boldsymbol{p}} - (\dot{\boldsymbol{p}} \boldsymbol{e}_N) \boldsymbol{e}_N)}{\| (\dot{\boldsymbol{p}} - (\dot{\boldsymbol{p}} \boldsymbol{e}_N) \boldsymbol{e}_N) \|} \, . \tag{5.7}$$

The friction force in the tangential plane depends on the normal force, e. g., the collision force:

$$\boldsymbol{F}_{fk} = -\mu_{fk} F_c \boldsymbol{e}_T \, , \tag{5.8}$$

where μ_{fk} denotes the sliding friction coefficient, which depends on the materials of the colliding objects.

The friction force is directed opposite to the direction of the tangential velocity $\dot{p}_T$ (cf. Fig. 5.2a). If $\dot{p}_T$ is decreased below a minimum velocity v_{stic}, the kinematic friction changes to static friction.

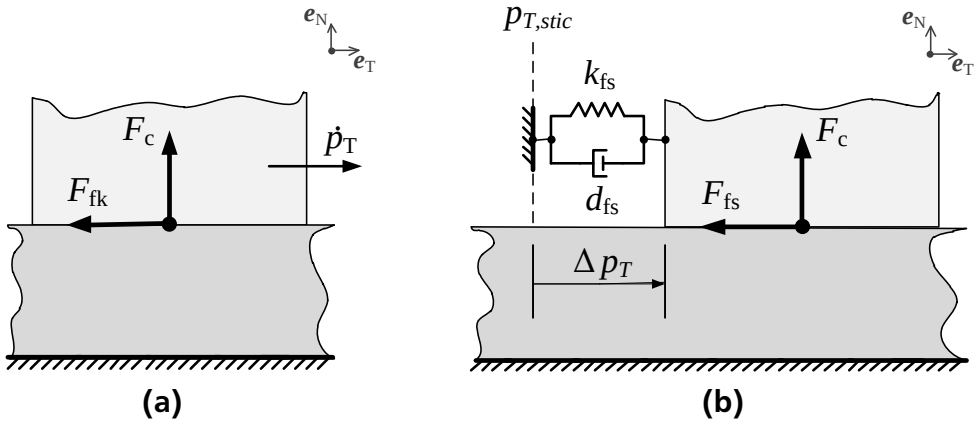

Figure 5.2.: Friction (a) and stiction (b) model.

5.1.4 Static Friction

Static friction is depicted in Fig. 5.2b. The object sticks to the current position and reacts to external forces as a visco-elastic material. We assume the following Kelvin-Voigt model for the computation of the stiction force:

$$\boldsymbol{F}_{\mathrm{fs}} = (-k_{\mathrm{fs}}\Delta p_{\mathrm{T}} - d_{\mathrm{fs}}\dot{p}_{\mathrm{T}})\boldsymbol{e}_{\mathrm{T}} \tag{5.9}$$

$$\text{with} \quad \Delta p_{\mathrm{T}} = p_{\mathrm{T}} - p_{\mathrm{T,stic}}\,. \tag{5.10}$$

$p_{\mathrm{T,stic}}$ denotes the position at which the transition from friction to stiction occurs (cf. Fig. 5.2b). The transition to kinetic friction is triggered for static friction forces F_{fs} that exceed a defined maximum static friction F_{stic} which depends on the current normal force and the static friction coefficient μ_{fs} (cf. Fig. 5.3):

$$F_{\mathrm{stic}} = \mu_{\mathrm{fs}} F_{\mathrm{c}}, \quad \mu_{\mathrm{fs}} \geq \mu_{\mathrm{fk}}\,. \tag{5.11}$$

Standard mechanics literature can be referred to for appropriate values of μ_{fs} and μ_{fk}. The values for k_{fs} and d_{fs}, however, are a bit more difficult to determine and require some tuning. Depending on the application and the material properties, usually a high stiffness is chosen for k_{fs} based on which d_{fs} is assigned an appropriate value.

5.1.5 Collision and Friction State Machine

Fig. 5.3 illustrates the computation process for modeling collisions, captured by the aforementioned equations, in form of states and triggering transition conditions.

5.1.6 Simulation Example

Simulation results of a bouncing contact of a metal object on a soft rubber surface are displayed in Fig. 5.4. The parameters used in the simulation example are listed in Table 5.1. The elastic

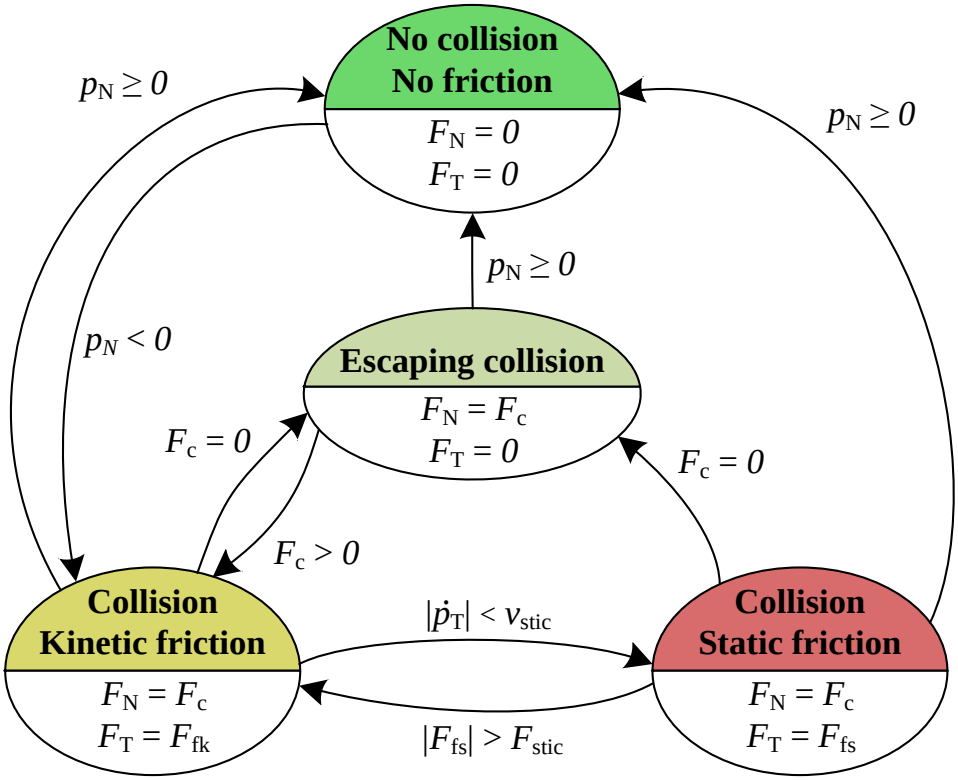

Figure 5.3.: State diagram of contact model.

modulus $E = 0.01 \cdot 10^9\,\mathrm{N/m^2}$ for soft rubber is given in standard mechanics literature. With a thickness $L = 10\,\mathrm{cm}$ and a contact area of $A = 1\,\mathrm{cm}^2$, the resulting stiffness of the rubber layer is:

$$k_c = \frac{EA}{L} = 10^4\,\mathrm{N/m} \tag{5.12}$$

The elastic modulus of the metal object has no significant effect on the combined contact stiffness (cf. (5.4)).

5.1.7 Experimental Validation

We validated the presented contact model by comparing experimental measurements from a ball dropped on a force plate with the corresponding simulation results. Fig. 5.5 describes the experimental setup and results. The simulation results show a very good agreement with the ball motion and the contact forces at the first four bounces, later bounces in the experiment seem to be more damped. This is presumably due to energy dissipation at low velocities not considered in our model. Both peak values and shape of the highly transient contact situation forces are closely approximated by the simulation, as a close-up of one of the peak forces shows.

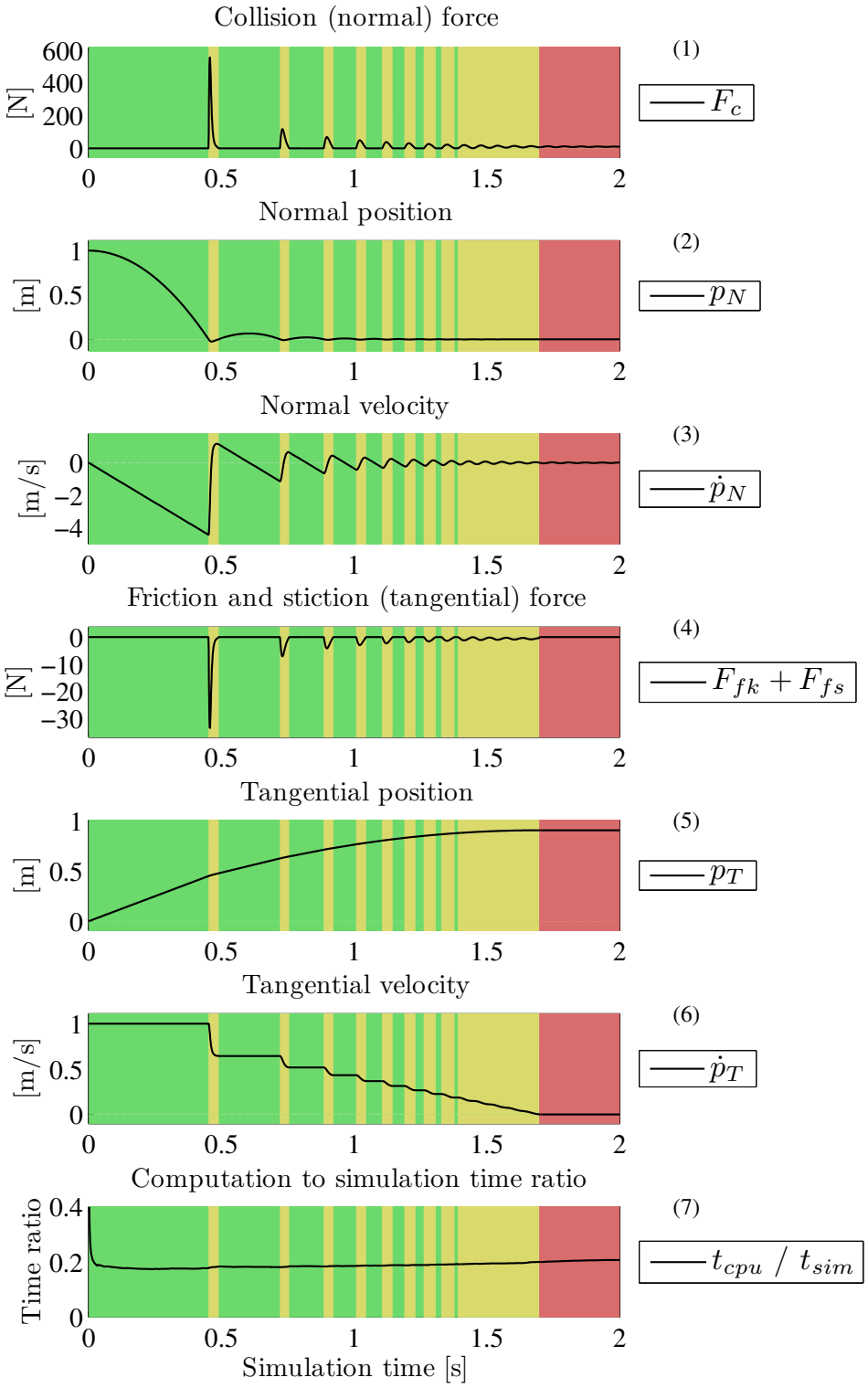

Figure 5.4.: Contact model simulation results for a bouncing point mass. Plot 1–3: no collision state (green), collision state (yellow, red), Plot 4–7: no collision state (green), kinetic friction state (yellow), static friction state (red). Solver settings: solver: [ode23 (bogacki-shampine)], relative tolerance: [$10^{(-3)}$], shape preservation: [enable all], number of consecutive minimum steps: [1], maximum simulation step width $\Delta t_{\max} = 1\,\mathrm{ms}$; zero-crossing options: algorithm: [adaptive], number of consecutive zero crossings: [1000]; further available settings: [auto].

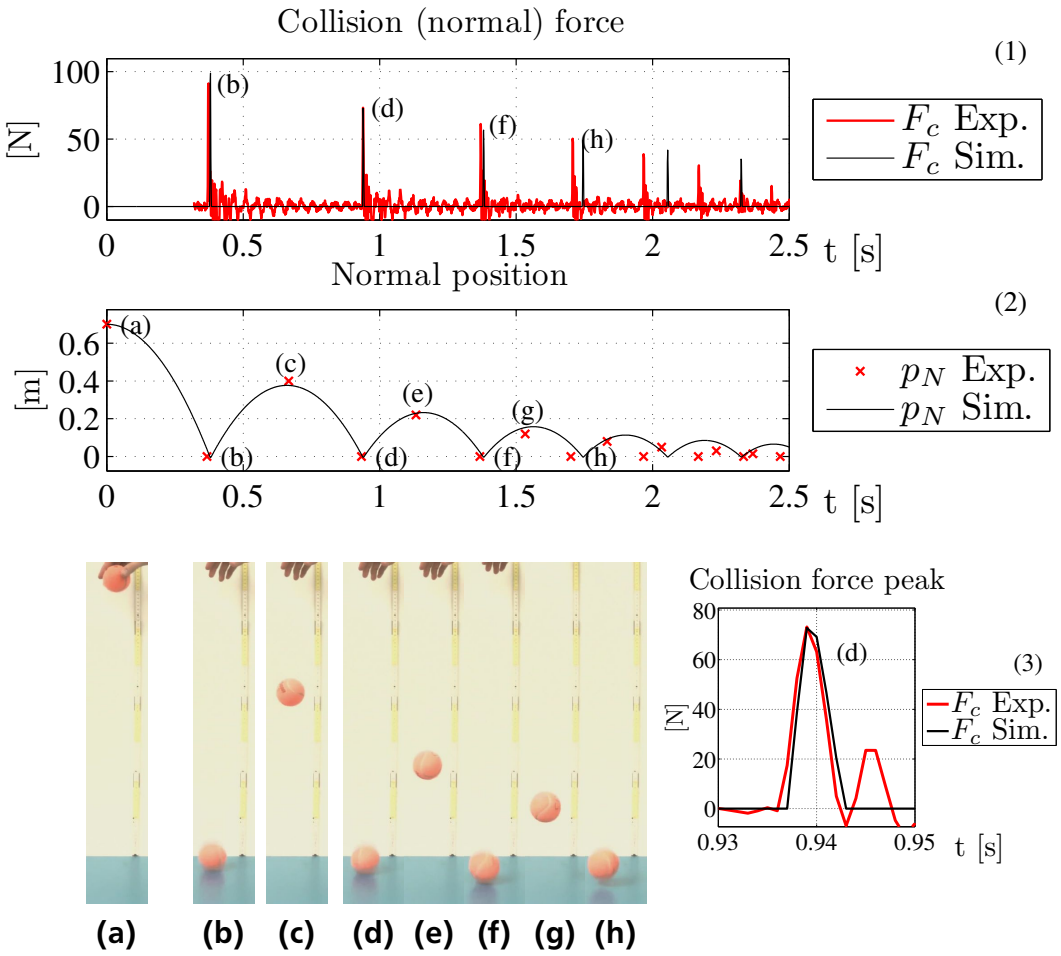

Figure 5.5.: Comparison of simulation and experimental data of a bouncing ball. A tennis ball is dropped on a force plate from a height of 70 cm. Plot (1) compares the simulated collision forces (black) with the measurements (red). Plot (3) displays a close-up from the second collision force peak. Pictures (a) to (h) come from the video recorded during the experiment and show the peak and collision positions of the ball. Plot (2) compares the ball positions read off the pictures with the simulation results. Simulation parameters: $m_{\mathrm{Ball}} = 0.05\,\mathrm{kg}$, $k_{\mathrm{c}} = 1.7 \cdot 10^4\,\mathrm{N/m}$, $\lambda_{\mathrm{c}} = 2.4 \cdot 10^4\,\mathrm{Ns/m^2}$, $p_{\mathrm{N}}(0) = 0.7\,\mathrm{m}$, $\dot{p}_{\mathrm{N}}(0) = 0\,\mathrm{m/s}$, $\dot{p}_{\mathrm{T}}(0) = 0\,\mathrm{m/s}$. The data of the force plate were measured with a rate of 1 kHz.

Table 5.1.: Parameters used in the simulated collision example

Parameter	Value	Parameter	Value
$p_{\mathrm{N}}(0)$	1 m	μ_{fk}	0.06
$\dot{p}_{\mathrm{T}}(0)$	1 m/s	μ_{fs}	0.1
m	1 kg	v_{stic}	0.001 m/s
k_{c}	10^4 N/m	k_{fs}	10^4 N/m
λ_{c}	$7.5 \cdot 10^3$ Ns/m^2	d_{fs}	40 Ns/m

5.2 Safety Estimation

The work presented in this Section was published in: Proceedings of the IEEE/RSJ International Conference on Intelligent Robots and Systems, 2012 [38].

In this section, an upper limit estimation for occurring contact forces depending on joint configuration and velocity is calculated. It is assumed that all kinetic energy of the robot arm is dissipated or transformed into potential energy of the elastic contact during the collision by deformation of the contact area. This is true for clamping situations and collisions with objects with a considerably higher mass compared to the reflected inertia of the robot at the contact point.

5.2.1 Dynamic Impact

Methods for estimation of contact force and stress were presented in [68] and [51]. We extend these methods for robotic arms with joint elasticity by considering the potential energy stored in the springs. In addition, the static clamping case is considered. The reflected inertia at the end effector is given by the operational space inertia matrix $\mathbf{\Lambda}_{\mathrm{c}}$ [28]

$$\mathbf{\Lambda}_{\mathrm{c}}(\boldsymbol{q}) = \left(\boldsymbol{J}(\boldsymbol{q})\, \boldsymbol{M}(\boldsymbol{q})^{-1} \boldsymbol{J}(\boldsymbol{q})^{\top} \right)^{-1} , \tag{5.13}$$

where $\boldsymbol{J}$ is the Jacobian and $\boldsymbol{M}$ the inertia matrix of the manipulator. The mass matrix $\boldsymbol{M}$ incorporates the additional mass of a load at the end effector, if present.

Assuming an elastic collision, the impact is modeled as a spring, where the kinetic energy of the robot arm is stored as potential energy. Regarding a constrained impact, it is assumed that during the impact all kinetic energy from the robot arm is transferred into potential energy of the elastic contact

$$\frac{1}{2}\, l_{\mathrm{c}}^2\, k_{\mathrm{c}} = E_{\mathrm{kin}} = \frac{1}{2} \mathbf{v}_{\mathrm{c}}^{\top} \mathbf{\Lambda}_{\mathrm{c}} \mathbf{v}_{\mathrm{c}} , \tag{5.14}$$

with spatial velocity $\mathbf{v}_{\mathrm{c}}$, collision stiffness k_{c}, and collision compression l_{c}.

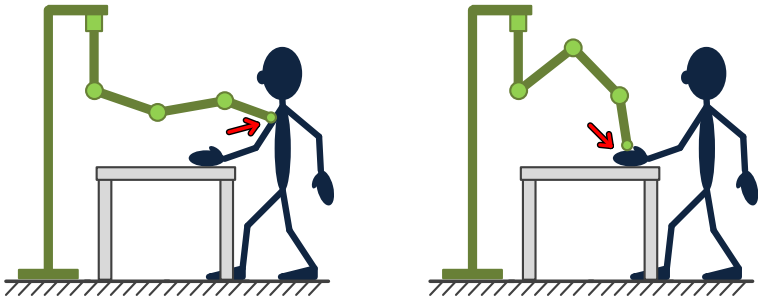

Figure 5.6.: Unconstrained (left) and constrained (right) collision (cf. [22]) in a typical pick-and-place scenario of a lightweight, mobile robot arm.

$$\mathbf{v}_{\mathrm{d}} = \begin{pmatrix} v_O \\ \boldsymbol{\omega} \end{pmatrix} \tag{5.15}$$

When calculating the operational space inertia matrix for systems with $n < 6$ DOF, the Jacobian has to be reduced to contain only independent rows. Therefore, it is more convenient to calculate the kinetic energy in joint space

$$l_{\mathrm{c}} = \sqrt{\frac{\dot{\boldsymbol{q}}^{\top} \boldsymbol{M}(\boldsymbol{q}) \dot{\boldsymbol{q}}}{k_{\mathrm{c}}}} \,, \tag{5.16}$$

with $\dot{\boldsymbol{q}}$ denoting the joint velocities. By this means, it is possible to use the maximum spring force in the elastically deformed contact area to estimate an upper bound for the peak collision force:

$$f_{\mathrm{c}} = k_{\mathrm{c}}\, l_{\mathrm{c}} = \sqrt{k_{\mathrm{c}}\, \dot{\boldsymbol{q}}^{\top} \boldsymbol{M}(\boldsymbol{q})\, \dot{\boldsymbol{q}}} \,. \tag{5.17}$$

By modeling the contact area and cushioning the robot as a layer of thickness L with elastic modulus E and contact surface A,

$$f_{\mathrm{c}} = \sqrt{\frac{EA}{L}\, \dot{\boldsymbol{q}}^{\top} \boldsymbol{M}(\boldsymbol{q})\, \dot{\boldsymbol{q}}} \,, \tag{5.18}$$

the medium normal pressure σ_{c} on this contact surface A can be formulated, as described in [37], as:

$$\sigma_{\mathrm{c}} = \frac{f_{\mathrm{c}}}{A} = \sqrt{\frac{E}{AL}\, \dot{\boldsymbol{q}}^{\top} \boldsymbol{M}(\boldsymbol{q})\, \dot{\boldsymbol{q}}} \,. \tag{5.19}$$

In case of insufficient decoupling of link and motor, the reflected inertia of the motors,

$${}^{\mathrm{j}}\boldsymbol{I}_{\mathrm{m}} = \mathrm{diag}\left({}^{\mathrm{j}}\boldsymbol{I}_{\mathrm{m}_1}, \ldots, {}^{\mathrm{j}}\boldsymbol{I}_{\mathrm{m}_n}\right) \,, \tag{5.20}$$

with rotor inertia $I_{\mathrm{r}i}$ and combined transmission ratio z_i of joint i (the product of the gearbox ratio z_{g_i} and the pulley transmission ratio z_{p_i}), needs to be taken into account as well. Here, $\boldsymbol{M}$ and $\boldsymbol{B}$ can be added because of the stiff coupling $\dot{\boldsymbol{q}} \approx \dot{\boldsymbol{\theta}}$ of motor and joint.

$$E_{\mathrm{kin}} \approx \dot{\boldsymbol{q}}^{\top}\left(\boldsymbol{M}(\boldsymbol{q}) + {}^{\mathrm{j}}\boldsymbol{I}_{\mathrm{m}}\right)\dot{\boldsymbol{q}} \tag{5.21}$$

For a weak coupling between motor and joint, however, joint and motor velocities strongly differ and the effective kinetic energy is smaller than the sum of the kinematic link and kinematic motor energies

$$\dot{\boldsymbol{q}}^{\top}\boldsymbol{M}(\boldsymbol{q})\dot{\boldsymbol{q}} \; + \; {}^{\mathrm{j}}\dot{\boldsymbol{\theta}}^{\top}\,{}^{\mathrm{j}}\boldsymbol{I}_{\mathrm{m}}\,{}^{\mathrm{j}}\dot{\boldsymbol{\theta}} \; > \; E_{\mathrm{kin,eff}} \; > \; \dot{\boldsymbol{q}}^{\top}\boldsymbol{M}(\boldsymbol{q})\dot{\boldsymbol{q}} \tag{5.22}$$

Summarizing, the dynamic impact pressure can be reduced by

- low joint and Cartesian velocities,
- low reflected inertia mass at the collision point,
- large contact area, and
- thick and soft cushioning.

5.2.2 Static Clamping

The static clamping force can be derived by transforming the joint actuator torques $\boldsymbol{\tau}_{\mathrm{m}}$ and gravitational torques $\boldsymbol{\tau}_{\mathrm{g}} = -\boldsymbol{g}(\boldsymbol{q})$ to Cartesian space using the Jacobian pseudoinverse:

$$\boldsymbol{f}_{\mathrm{s}} = \left(\boldsymbol{J}_{v}^{\top}(\boldsymbol{q})\right)^{+}\left({}^{\mathrm{j}}\boldsymbol{\tau}_{\mathrm{m}} - \boldsymbol{g}(\boldsymbol{q})\right). \tag{5.23}$$

The maximum normal stress produced by this force on the contact surface A can be given as:

$$\sigma_{\mathrm{s}} = \frac{1}{A}\left\|\left(\boldsymbol{J}_{v}^{\top}(\boldsymbol{q})\right)^{+}\left({}^{\mathrm{j}}\boldsymbol{\tau}_{\mathrm{m,max}} - \boldsymbol{g}(\boldsymbol{q})\right)\right\|. \tag{5.24}$$

A reduction of the maximum clamping pressure can therefore be achieved by

- low masses,
- low maximum motor torques, and
- large contact area (e.g. using soft cushioning).

In addition, almost all available robot arms use high reduction ratios, reflecting the motor friction with the transmission ratio z to the joints. This leads to hardly backdrivable systems. Furthermore, many systems activate joint brakes in case of a collision to compensate for the gravitational forces of the robot structure. However, this also makes it impossible to push the robot away from the collision. In such case, the upper bound of the static clamping forces drastically increases and can go up to the values of the dynamic clamping forces.

As pointed out in [18], quasi-static clamping can lead to extremely high contact forces. This is the case in near-singular positions, where the Jacobian $\boldsymbol{J}$ becomes singular. For lightweight robot arms, this problem can be mitigated to a certain extent by the use of low-power motors, highly backdrivable joints, and soft cushioning, reducing the clamping stress σ_{s}. The only really safe solution, however, is to avoid near-singular configurations.

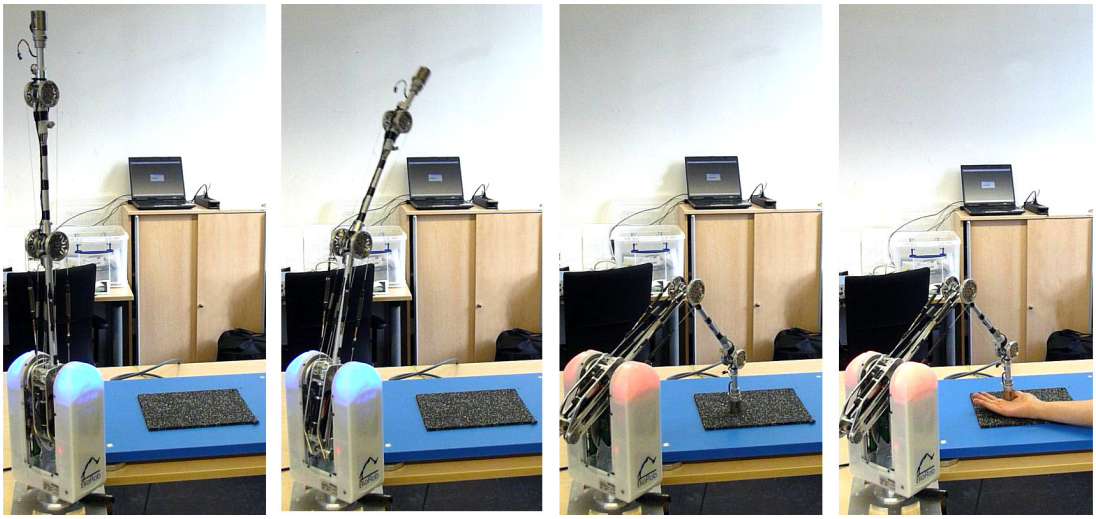

Figure 5.7.: Collision experiments without (frame 1–3) and with clamping a human hand (frame 4) using a force plate.

5.2.3 Potential Energy

In clamping situations, a high amount of potential energy can be stored in the springs:

$$E_{\mathrm{pot,e}} = \frac{1}{2} \left({}^{\mathrm{j}}\boldsymbol{\theta} - \boldsymbol{q}\right)^{\top} {}^{\mathrm{j}}\boldsymbol{K}_{\mathrm{e}} \left({}^{\mathrm{j}}\boldsymbol{\theta} - \boldsymbol{q}\right) \tag{5.25}$$

If this potential energy is suddenly released by breaking away from the collision, it can pose a danger.

5.2.4 Simulation and Experimental Results

To validate the presented approach, collisions were conducted in simulation and experiment with a typical trajectory of pick-and-place application where constrained clamping can occur (cf. Figure 5.6). The force measurement was performed with a force plate, as shown in Figure 5.7. The desired end effector position of the robot arm was placed below the force plate, in order to generate a colliding trajectory with static clamping characteristics (Figure 5.8). No collision detection and reaction strategy was activated.

The contact stiffness was determined by using estimated values for the contact area A, the layer thickness L and Young's Modulus E. Calibration measurements and comparison with the simulated contact model then yielded a refined value of $k_{\mathrm{c}} = 50\,\mathrm{kN/m}$, which was used in the simulation.

Dynamic Impact

As depicted in Fig. 5.8 and 5.9, the impact occurs at $t_{\mathrm{c}} = 0.96\,\mathrm{s}$. The joint velocity before the impact amounts to

$$\dot{\boldsymbol{q}}(t_{\mathrm{c}}) = \begin{pmatrix} 0 & -1.3741 & -1.8019 & -0.9496 \end{pmatrix}^{\top} \mathrm{rad/s} \tag{5.26}$$

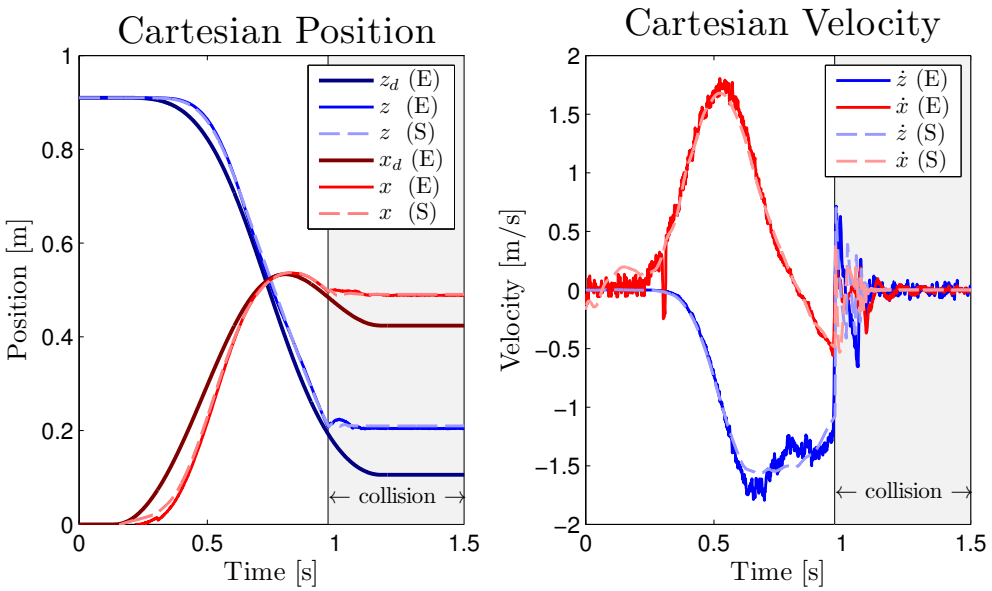

Figure 5.8.: Cartesian trajectory comparison of collision simulation (S) and experiment (E) with contact at $z_c = 0.205\,\mathrm{m}$ and $t_c = 0.96\,\mathrm{s}$.

The effective kinetic energy at impact for a weak motor-link coupling can be approximated as (5.22)

$$E_{\mathrm{kin}}(t_c) = \frac{1}{2}\,\dot{\boldsymbol{q}}^{\top}\boldsymbol{M}(\boldsymbol{q})\,\dot{\boldsymbol{q}} = 0.2826\,\mathrm{J}\,, \tag{5.27}$$

and according to (5.18), this yields an estimate for the maximum contact area compression l_c and impact force peak f_c:

$$f_c = \sqrt{2k_c E_{\mathrm{kin}}} = 168.1\,\mathrm{N}\,. \tag{5.28}$$

This calculated value for the impact force peak matches the results of the simulation and experimental measurements, $f_{c,\mathrm{real}} = 178.5\,\mathrm{N}$ (cf. Fig. 5.10), quite well. The collision occurred with $v = 1.23\,\mathrm{m/s}$ and a duration of approximately 7 ms for the first impact peak.

The reflected inertias of the robot arm at time of collision are listed in Table 5.3. These values are at least one magnitude lower than the properties of comparable robot arms where the motors are directly located in the joints.

Static Clamping

As depicted in Fig. 5.11, no collision detection is active. After the impact, beginning at $t_s = 1.5\,\mathrm{s}$, the robot arm pushes with constant motor torques $\boldsymbol{\tau}_m$ and gravitational torques $-\boldsymbol{g}(\boldsymbol{q})$ caused by the robot structure. The combined effect of the actuator and gravitational torques leads to a static clamping force of

$$\boldsymbol{f}_s = (\boldsymbol{J}_v^{\top})^{+}\,({}^{j}\boldsymbol{\tau}_m - \boldsymbol{g}) = -\begin{pmatrix}2.386 & 0 & 16.860\end{pmatrix}^{\top}. \tag{5.29}$$

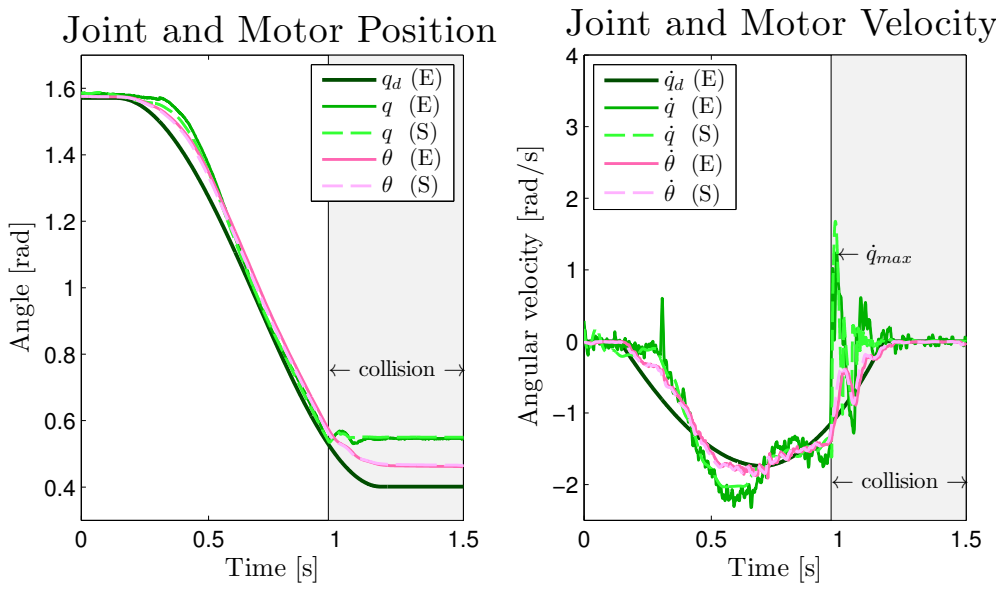

Figure 5.9.: Joint q and motor θ trajectory of joint 2 in collision simulation (S) and experiment (E). On the right, the joint velocity drop caused by the impact is marked with $\dot{q}_{\max}$.

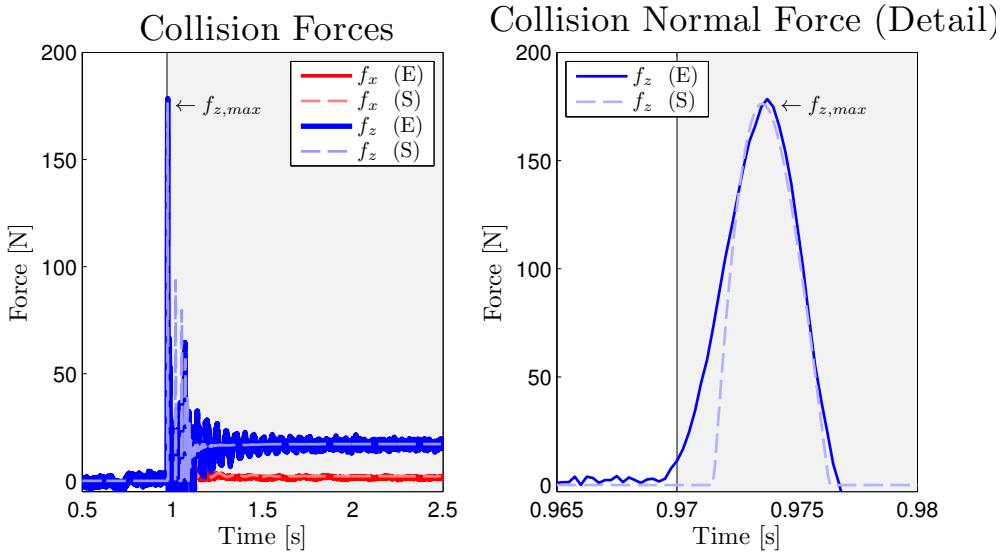

Figure 5.10.: Impact and static clamping forces in simulation (S) and experiment (E). A close-up of the first impact peak is displayed on the right, showing a peak width of 7 ms.

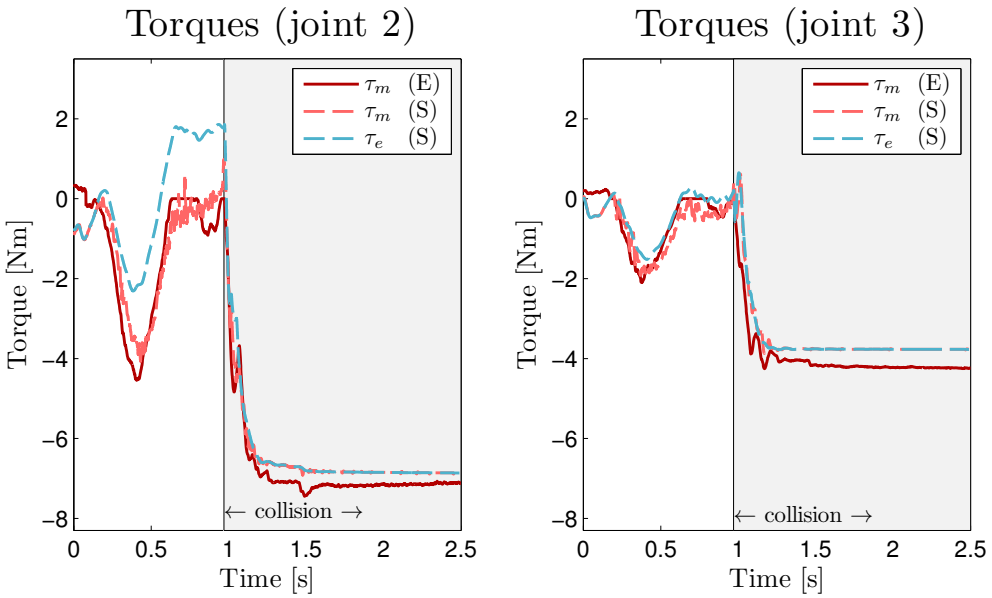

Figure 5.11.: Torques of joint 2 and 3 in collision simulation (S) and experiment (E). In contrast to the motor torque τ_{m}, the joint torque produced by the series elastic elements τ_{e} can not be directly measured during the experiment.

For comparison, the real values from the experiments and simulation amount to

$$\boldsymbol{f}_{\mathrm{s}} = \begin{pmatrix} 2.000 & 0 & 16.975 \end{pmatrix}^{\top}. \tag{5.30}$$

More of interest for safety evaluation, however, is the maximum clamping force that the actuators and robot arm weight can produce

$$\boldsymbol{f}_{\mathrm{s,max}} = \left(\boldsymbol{J}_{v}^{\top}\right)^{+} \left({}^{\mathrm{j}}\boldsymbol{\tau}_{\mathrm{m,max}} - \boldsymbol{g}\right), \tag{5.31}$$

yielding

$$f_{\mathrm{s,max}} = \left|\left|\left(\boldsymbol{J}_{v}^{\top}\right)^{+} \left({}^{\mathrm{j}}\boldsymbol{\tau}_{\mathrm{m,max}} - \boldsymbol{g}\right)\right|\right| = 24.7\,\mathrm{N} \tag{5.32}$$

in this configuration.

Another very important measure is the stored potential energy in the springs:

$$E_{\mathrm{pot,e}} = \frac{1}{2}\left({}^{\mathrm{j}}\boldsymbol{\theta} - \boldsymbol{q}\right)^{\top} \boldsymbol{K}_{\mathrm{e}} \left({}^{\mathrm{j}}\boldsymbol{\theta} - \boldsymbol{q}\right) = 2.06\,\mathrm{J} \tag{5.33}$$

If released, this stored energy could, neglecting dissipative effects and assuming full conversion of potential to kinetic energy, produce a worst case impact force of

$$f_{\mathrm{c,pot}} = \sqrt{2\,k_{\mathrm{c}}\,E_{\mathrm{pot,e}}} = 453\,\mathrm{N}. \tag{5.34}$$

Resulting Pressure

The corresponding pressures can be derived from the impact forces:

$$\text{impact pressure:} \quad \sigma_{\mathrm{c}} = \frac{f_{\mathrm{c}}}{A} = 319.5\,\mathrm{kN/m^2}, \tag{5.35}$$

$$\text{clamping pressure:} \quad \sigma_{\mathrm{s}} = \frac{f_{\mathrm{s}}}{A} = 28.5\,\mathrm{kN/m^2}. \tag{5.36}$$

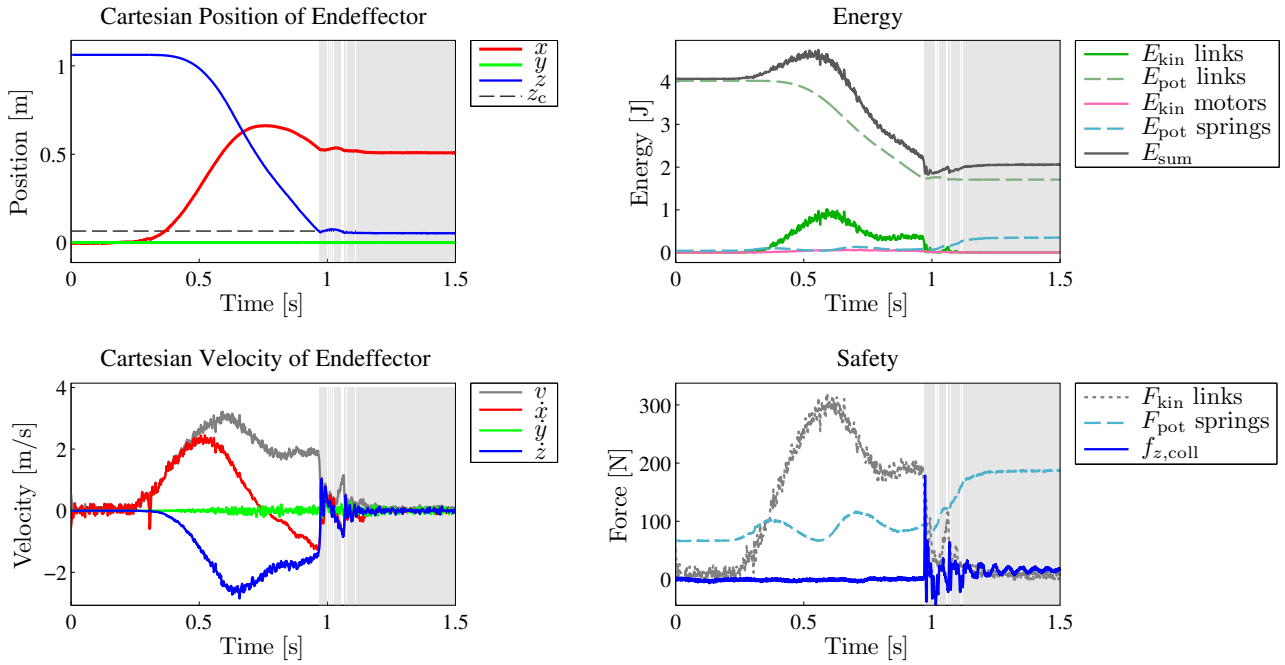

Figure 5.12.: Experimental measurement data with Cartesian states and safety index of an additional high speed collision experiment with the BioRob-X4 arm. The Cartesian impact velocity amounts to 2 m/s (bottom left plot). The kinetic and potential energies (top right plot) are used for on-line calculation of the impact and clamping safety index F_{kin} and the elastic energy storage safety index F_{pot} (bottom right plot). At time of impact $t_c = 0.95\,\text{s}$, indicated by the grey areas, the impact force $f_{z,\text{coll}}$ matches the impact safety index F_{kin} very well. During clamping ($t > t_c$) the elastic energy storage safety index indicates that the potential energy stored in the springs could cause an impact force of $f_{z,\text{coll}} = 200\,\text{N}$ if the robot arm is suddenly released from collision. This potential danger can be dealt with by setting the motor voltages to zero, causing the elastic energy stored in the springs to accelerate the rotor inertias and to be dissipated by the motor friction.

5.2.5 Discussion

The impact force and pressure is highly dependent on the contact area and stiffness. Therefore, covering design is important [51].

For the safety evaluation of the robot arm with series elastic tendon actuation we assumed only a small minimum contact area A and high collision stiffness k_e. Even with these parameters the impact pressure and impact energy are far below the safety limits. The maximum static clamping pressure of 25 N is also far below the requirements of the industrial safety norm and of the defined safety limits in literature.

The energy stored in the springs in a clamping situation can be dangerous, if suddenly released. Therefore, a collision detection method is needed to make the motors compliant in such a case.

Because of the non-locking motors in the proposed robot arm design, the energy stored in the springs is then transferred to the motors, where it dissipates. This is an advantage over the designs with non-backdrivable motors. These, on the other hand, can store energy in the springs more efficiently.

The amount of potential energy stored in the springs during clamping was higher than the kinetic impact energy by factor 7. It is therefore important to observe the amount of potential energy stored in the springs during operation. Nevertheless, even this energy would not cause impact forces exceeding the safety levels.

5.3 Safety Comparison of Actuation Types

The work presented in this Section was published in: Proceedings of the 7th German Conference on Robotics 2012 [34].

Applications with pHRI require a high level of safety even in case of software or hardware failures. This section highlights the advantages of combining tendon actuation with transmission elasticity to maximize safety for robotic arms sharing workspaces with humans. To this end, the collision behavior of combinations of tendon or joint and elastic or stiff actuation with geared electrical motors as reliable actuators is compared using the lightweight BioRob arm as robotic platform in simulation. For the comparison a worst case scenario is assumed in which the robot arm is accelerated with maximum supply voltage over its joint range and collides with maximum end effector velocity. The study shows that the robot arm achieves end effector velocities as high as 6 m/s and that elastic tendon actuation reduces the end effector impact energy and force by up to 90 % compared to stiff joint actuation. A considerable reduction of the gearbox stress is also achieved. In addition, the effect of motor current fuses limiting the motor torques is evaluated. It is shown that for the given high speed scenario, torque limiting devices can be effective to prevent excessive clamping forces in case of failure, but can not reduce the impact peak force without heavily compromising the robot dynamics. The main design criterion for safety should therefore be lightweight link design and compliant actuation, which can be achieved by using elastic tendon actuation. The section concludes with the comparison of safety properties of robotic arms in research and industry.

The BioRob arm combines tendons and elasticity in the drivetrain to achieve both lightweight design and compliant actuation [35]. This section compares the collision behavior and safety properties of the elastic tendon actuation as used in the BioRob arm to other actuation designs. A worst case collision scenario is defined in Section 5.3.1. After introducing all possible combinations of elastic or stiff, and tendon or joint actuation in Section 5.3.2, the impact behavior of the actuation designs is evaluated in Section 5.3.3 with respect to impact energy, force and joint torques using the worst case scenario. In addition, the effect of fuses limiting the motor currents on the impact properties of the robot arm is examined to clarify if additional safety is obtained by these components.

The section concludes with a comparison of the effective operational space masses of the evaluated actuation designs when used in the BioRob arm and of effective mass values reported in literature for several robotic arms.

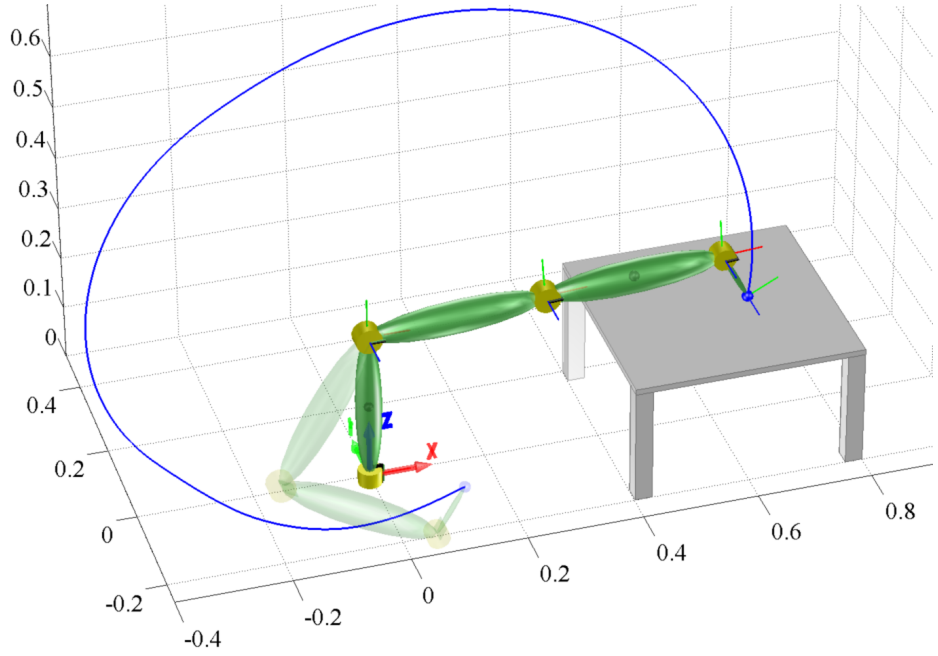

Figure 5.13.: Simulated collision trajectory of the BioRob arm, shown in initial configuration (transparent rendering) and configuration just before impact with the grey object (solid rendering). Axis dimensions are given in meters.

5.3.1 Collision Trajectory

In the worst case a software or hardware failure can cause the motor input voltages to be permanently set to the maximum supply voltage. The trajectory chosen for collision evaluation is depicted in Figure 5.13 and Figure 5.14. The robot arm starts in a configuration near the mechanical joint limits to have a maximum acceleration distance and accelerates to the opposing joint limits with the maximum voltage, where the end-effector collides with the object marked in grey. The maximum motor input voltage of the BioRob arm is $U_{\mathrm{a,max}} = 12\,\mathrm{V}$.

The highest end-effector velocities and lever arms are achieved in the outstretched configuration. The last link does not significantly contribute to the end-effector velocity because of its short length. In case of elastic actuation it has the potential to decouple the rest of the robot arm from the collision during the first impact phase, causing a significant decrease of the impact force peak.

Higher impact forces can therefore be expected when reducing the effective collision force lever arm of the last link by pointing the link towards the collision surface normal. The chosen impact configuration is shown is Figure 5.13.

The activation of the maximum motor voltages is timed separately in each motor in order to reach the described impact configuration. The motor of the second joint is accelerated from the beginning of the trajectory, whereas the motors of the third and fourth joint are accelerated at a later stage of the trajectory.

As can be recognized from Figure 5.14, the end-effector velocity at time of impact $v_{\mathrm{c}} = 6.33\,\mathrm{m/s}$ is slightly lower than the maximum trajectory velocity of $v = 6.64\,\mathrm{m/s}$, which is in turn lower than the maximum achievable end-effector velocity in the outstretched configuration of $v =$

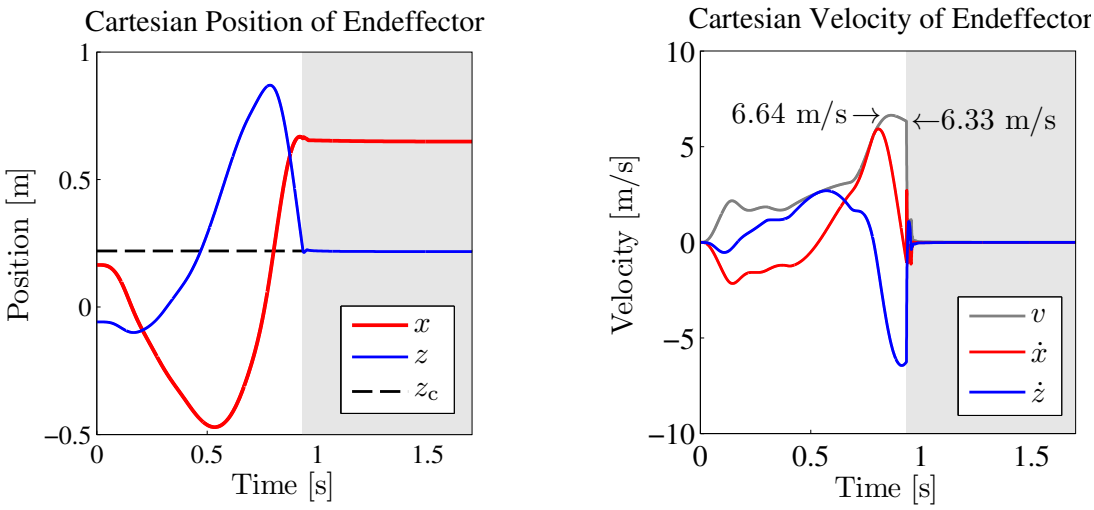

Figure 5.14.: Collision trajectory: end-effector trajectory in Cartesian space. The collision occurs at $z_c = 0.22\,\mathrm{m}$. The collision phase is marked in grey.

$7.4\,\mathrm{m/s}$. Nevertheless, for the stated reasons, the highest impact forces can be expected with the described configuration, as was validated in simulation.

When using elastic actuation, the joint velocity can be significantly higher than the motor velocity. These effects are discussed in the next sections.

5.3.2 Evaluated Actuation Designs

For the comparative simulation several different actuation designs are to be defined (cf. Fig. 5.15). All designs are based on the parameters of the BioRob-X4 arm, as listed in Table 5.2, and combine tendon or joint with elastic or stiff actuation.

The first group of actuation designs uses *Elastic Tendon Actuation* (ETA) with various stiffness settings:

(a) ETA with low tendon stiffness k_e and damping d_e as used in the BioRob-X4 arm (cf. Table 3.7),

(b) ETA with medium stiffness $8\,k_e$ and damping $8\,d_e$,

(c) ETA with high stiffness $80\,k_e$ and damping $80\,d_e$.

In the case of infinite stiffness and damping, the ETA transforms into *Stiff Tendon Actuation* (STA), which is not practically implementable because of the inherent elasticity of tendons and belts, but nevertheless interesting from a theoretical point of view to determine the upper bound behavior of ETA with high stiffness:

(d) STA with stiff coupling between motor and joint.

The last two defined actuation designs used for comparison have the motors placed in the joints instead of using tendon actuation. The first design uses a series elastic transmission element between motor and joint, the *Elastic Joint Actuation* (EJA):

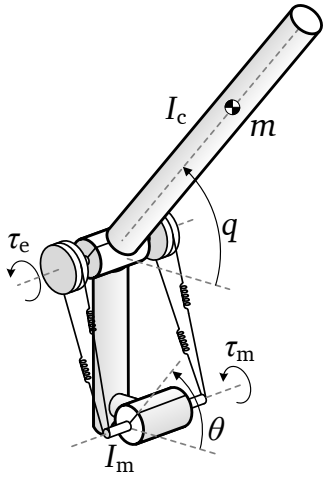

(a) Joint with elastic tendon actuation (ETA)

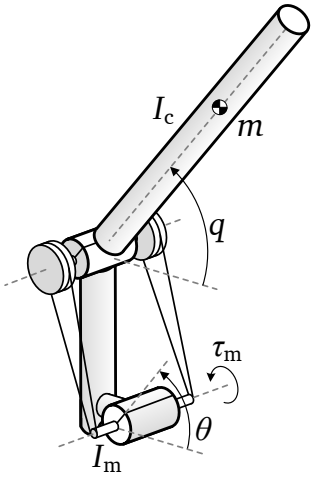

(d) Joint with stiff tendon actuation (STA)

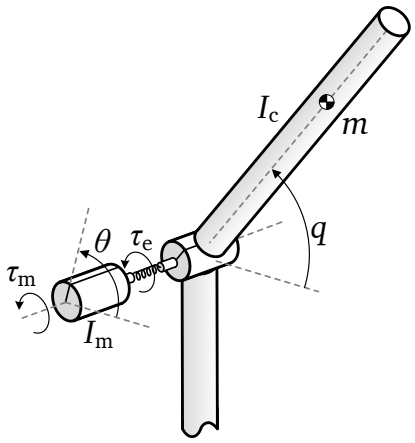

(e) Joint with elastic joint actuation (EJA)

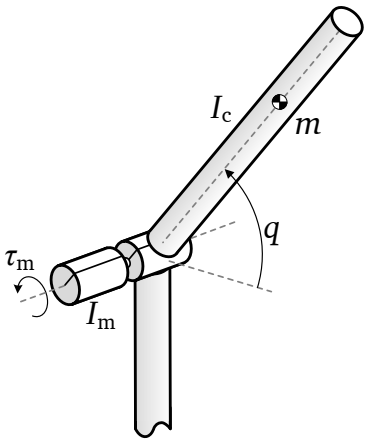

(f) Joint with stiff joint actuation (SJA)

Figure 5.15.: Evaluated actuation designs.

(e) EJA with motors placed in the joints.

The second design, *Stiff Joint Actuation* (SJA), exhibits stiff coupling between motor and joint:

(f) SJA with stiff coupling of motors and links.

To achieve realistic results, the collision area is modeled with the stiffness of the human neck, which represents one of the safety-critical areas of the human body. The contact is modeled as Hunt-Crossley material with a combined contact stiffness of $k_{\text{coll}} = 10^4\,\text{N/m}$, the stiffness of the human neck area as given in [3], and a nonlinear damping parameter of $\lambda_{\text{coll}} = 5 \cdot 10^3\,\text{Ns/m}^2$. The details of the contact model were given in Section 5.1.

Table 5.2.: Model parameters of the BioRob-X4 arm without gripper: Denavit-Hartenberg parameters DH, link center of mass position r_c with respect to the coordinate system in the subsequent joint, link mass m, combined transmission ratio z, rotor inertia I_r, and transmission stiffness k_e and damping d_e, both with respect to the joint.

Joint	1	2	3	4
DH (d, a, α)	$(0.276, 0, \frac{\pi}{2})$	$(0, 0.307, 0)$	$(0, 0.310, 0)$	$(0, 0.17, 0)$
r_c [m]	$(0, -0.14, 0)$	$(-0.32, 0, 0)$	$(-0.16, 0, 0)$	$(-0.07, 0, 0)$
m [kg]	2.350	1.530	0.160	0.055
z [−]	73.6	80.0	47.0	52.8
I_r [kgm^2]	$3.33 \cdot 10^{-6}$	$3.33 \cdot 10^{-6}$	$3.33 \cdot 10^{-6}$	$1 \cdot 10^{-6}$
k_e [Nm/rad]	100	80	35	6
d_e [Nms/rad]	0.05	0.05	0.05	0.05

5.3.3 Impact Evaluation

Impact without Current Limitation

The resulting end-effector collision forces are displayed in Figure 5.16 and range from a peak force of 179 N for the BioRob-X4 arm using ETA with the lowest stiffness to 822 N for the same robot arm structure with SJA instead of elastic cable actuation, i.e. with the motors located in the joints and rigidly connected to the links.

The static clamping forces after the first impact peak are generated by the maximum actuator torques and the gravitational torques of the robot structure and depend on the current robot configuration. For the designs (a)–(d) with cable actuation, the static clamping force is about 80 N, for the designs (e)–(f) with joint actuation the additional gravitational forces by placing the motors in the joints amount to a higher static clamping force of 90 N.

As can be seen in Figure 5.17, designs (a)–(d) have roughly the same kinetic energy

$$E_{kin} = E_{kin,links} + E_{kin,motors} \tag{5.37}$$

at impact time. The designs with lower actuation stiffness, however, posses a less strong coupling between motors and links, which acts as low pass filter on shocks from the links to the motors. For that reason the actuators with low stiffness coupling exhibit a higher decay time constant of the kinetic energy of the motors, as can be seen in Figure 5.17, causing a decrease of peak impact force from (d) 334 N in case of stiff coupling to (a) 179 N in case of low stiffness coupling (cf. Figure 5.16).

Placing the motors in the joints, as in designs (e) and (f) with joint actuation, results in a shift of masses towards the end-effector increasing the inertia and therefore also the kinetic energy of the robot arm from about 2 J to 24 J for stiff transmission and 30 J for series elastic transmission. The increase in kinetic energy of these designs leads to significantly higher impact forces. The impact kinetic energy with elastic transmission (e) is higher than with stiff transmission (f)

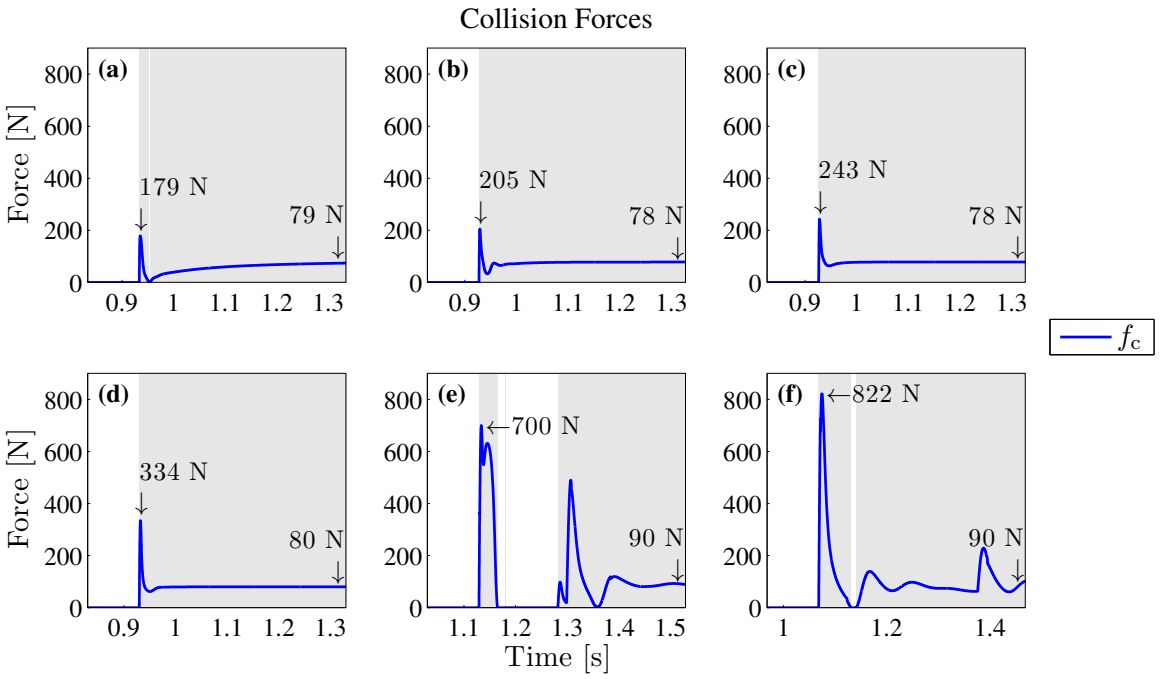

Figure 5.16.: Actuator comparison: end-effector collision forces for **(a)**–**(c)** ETA, **(d)** STA, **(e)** EJA, and **(f)** SJA (cf. Section 5.3.2).

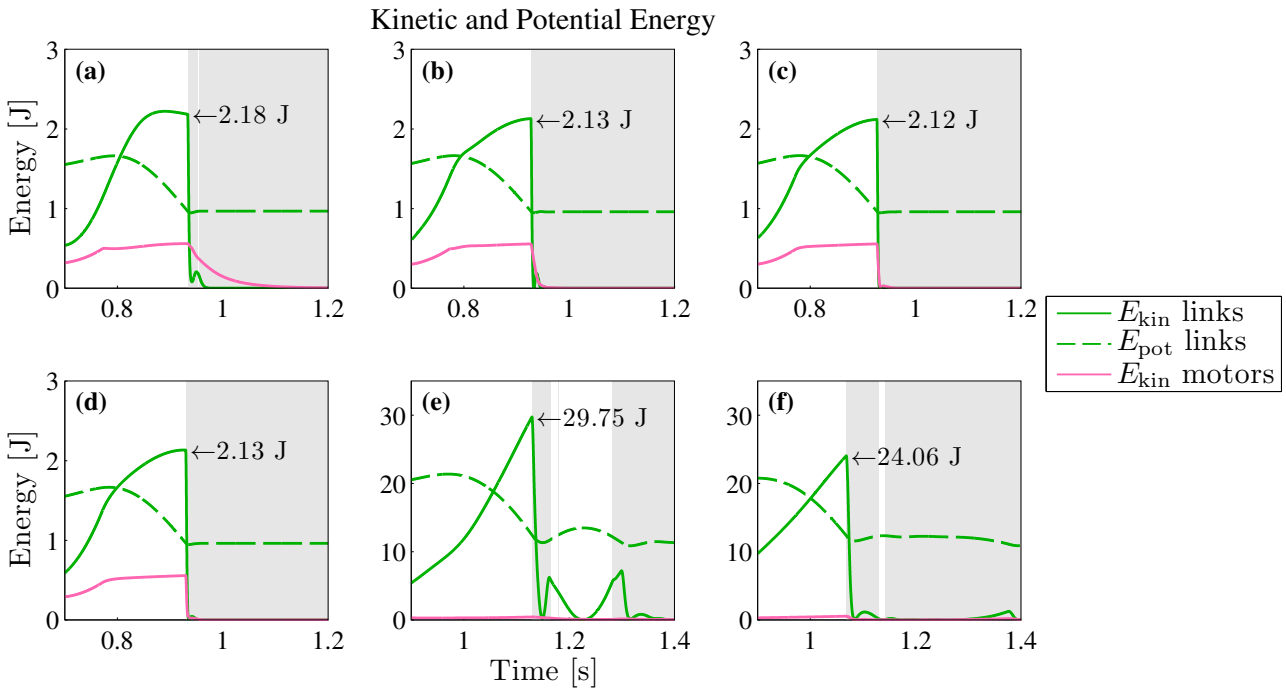

Figure 5.17.: Actuator comparison: kinetic and potential energies for **(a)**–**(c)** ETA, **(d)** STA, **(e)** EJA, and **(f)** SJA (cf. Section 5.3.2).

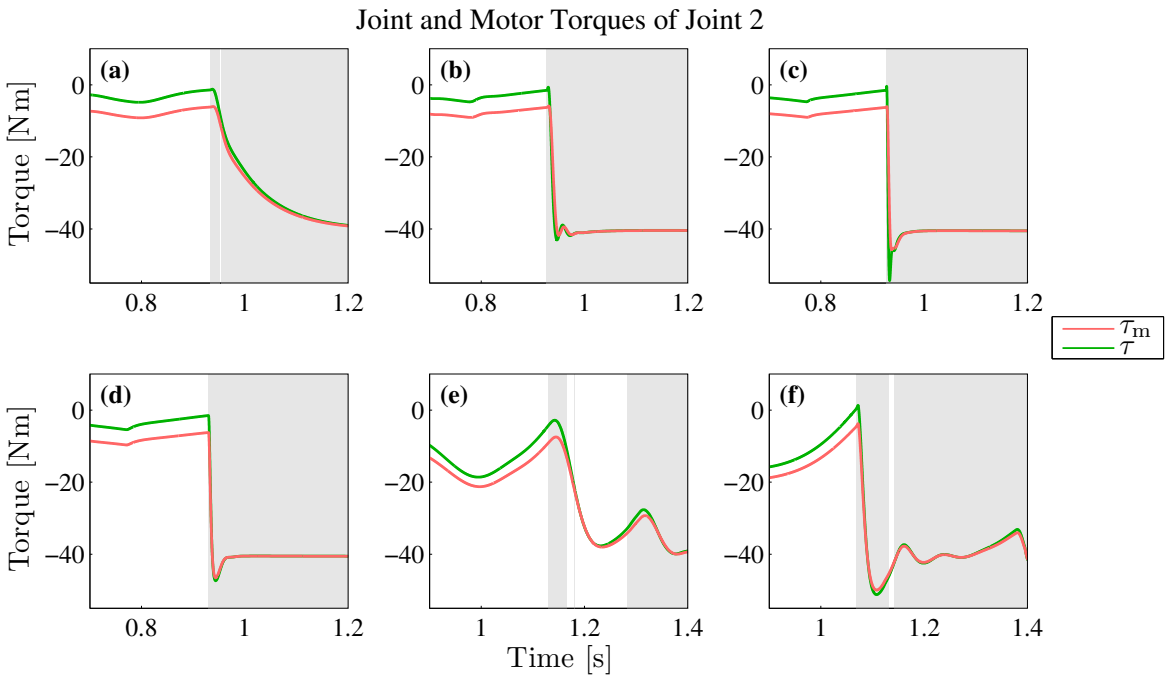

Figure 5.18.: Actuator comparison: torques of joint two for **(a)**–**(c)** ETA, **(d)** STA, **(e)** EJA, and **(f)** SJA (cf. Section 5.3.2).

because the elastic decoupling of motors and joints enables independent joint dynamics with much higher joint velocities. This effect is also visible when comparing the kinetic energy of elastic tendon (2.18 J) and stiff tendon actuation (2.13 J), although less distinct because of the lower link masses.

In contrast to the impact forces and energies the dominant factor on the joint torques is the transmission elasticity (cf. Figure 5.18). Low actuation transmission stiffness, such as for designs ETA (a) and EJA (e), low pass filter the collision shock on the motors and gearboxes.

Impact with Current Limiting Fuses

This section examines if the effects of the collision scenario presented in the previous sections can be attenuated by limiting the joint torques using robust hardware safety shut-off devices. For the given lightweight arm, a decoupling of those joints for which the maximum joint torque is exceeded without using brakes is feasible without compromising safety. This can be realized using a clutch-like device on joint level or motor fuses limiting the motor currents.

A comparison of the effects of the fuses on the collision forces and joint torques for elastic and stiff tendon actuation is shown in Figure 5.19. Ideal fuses with the lowest possible shut-off current of 6.3 A were chosen. Lower shut-off currents would overly restrict the dynamics of the robot arm and are therefore not suitable.

The fuse in the second joint blows at 23 ms for the elastic tendon actuation and at 3.6 ms for the stiff tendon actuation. In neither cases a reduction of the impact peak force is achieved. As already mentioned, the fuse switch-off current is at the lowest acceptable level. The switch-off delays therefore cannot be further reduced.

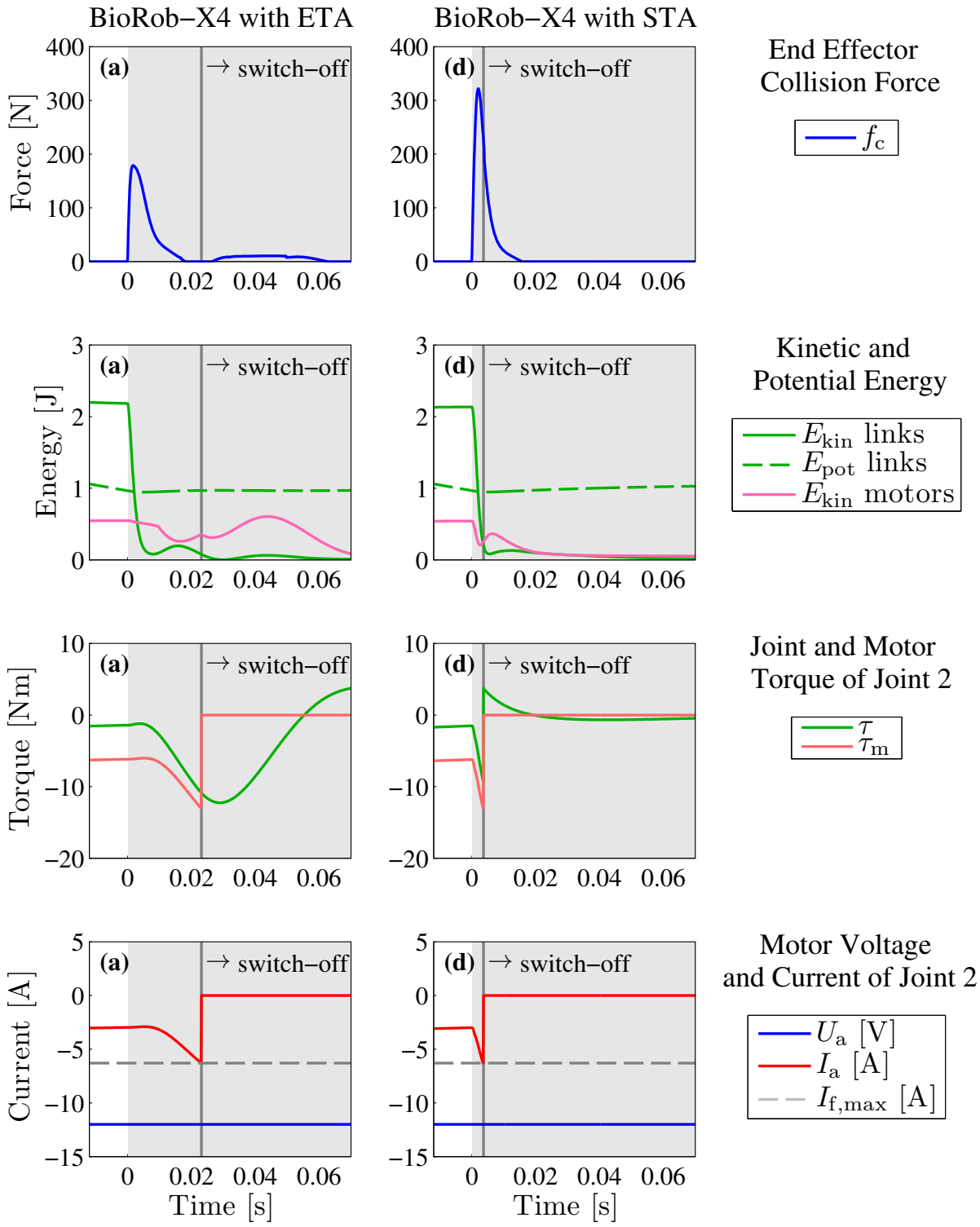

Figure 5.19.: Comparison of the collision behavior of the BioRob-X4 arm with elastic tendon actuation (ETA) **(a)** and stiff tendon actuation (STA) **(b)**, using ideal fuses with switch-off current $I_{f,max} = 6.3\,A$.

However, the joint torque τ and motor torque τ_{m} are bounded (to 13 Nm in the second joint) and the clamping force is reduced to zero. Fuses can therefore be used to prevent clamping in case the control software fails to do so. In normal operation, however, the controller is able to switch off the motors by software. Therefore, hardware based switch-off devices are only needed in the exceptional case of failure. To avoid additional complexity and weight, electrical fuses are therefore more practical for the presented setting than mechanical devices in the joints limiting the joint torques.

5.3.4 Comparison of Effective Mass

All simulated actuation designs used the same collision trajectory and roughly had the same impact velocity and configuration. Therefore, the effective end effector mass in operational space can be an appropriate measure for safety comparison. The effective mass is calculated by transforming the joint level dynamics equations to operational space [29]. Table 5.3 lists the effective end effector mass of all actuation designs at time of impact.

Table 5.3.: Effective end-effector mass $\Lambda_{\mathrm{c},z}$ in normal and $\Lambda_{\mathrm{c},x}$ in tangential collision direction, and maximum effective mass $\Lambda_{\mathrm{c},xz}$ in the trajectory plane at impact time for the 4 DOF BioRob arm with elastic tendon actuation (ETA), stiff tendon actuation (STA), elastic joint actuation (EJA), and stiff joint actuation (SJA).

	ETA	**STA**	**EJA**	**SJA**
$\Lambda_{\mathrm{c},x}\,[\mathrm{kg}]$	0.009	0.239	0.119	0.471
$\Lambda_{\mathrm{c},z}\,[\mathrm{kg}]$	0.023	0.155	0.306	0.755
$\Lambda_{\mathrm{c},xz}\,[\mathrm{kg}]$	0.122	0.521	1.66	1.86

For comparison, effective mass values reported in literature are listed in Tables 5.4 and 5.5. Because the inertia strongly depends on the robot configuration, each table stands for a distinct robot configuration as reported in the respective sources. For better comparability, the normalized effective mass [58] is also listed. For the human arm, a payload for repeated manipulations is assumed.

5.3.5 Discussion

The study shows for the evaluated collision scenario with the BioRob-X4 robot arm that elastic tendon actuation reduces the kinetic impact energy by 90 % to 2 J, the effective end-effector mass by 93 % to 122 g, the dynamic impact force by 80 % and the static clamping force by 10 % compared to stiff joint actuation of the same robot. A reduction of the impact torque shocks acting on the gearboxes is also achieved. These improvements are due to the tendon actuation enabling the motor placement at the first link and at a balancing position in the second link and by the transmission elasticity decoupling the motor from the link inertia.

By this means the robot arm exhibits a high level of safety even at velocities as high as 6 m/s. At the outstretched configuration, the robot arm has an effective mass of only 100 g and remains below 0.5 kg throughout the workspace excluding regions close to singular configurations.

Table 5.4.: Comparison of effective end-effector mass for the configuration shoulder $q_S = 20^\circ$ and elbow $q_E = -90^\circ$ as published in [58]). Values marked with * taken from [58].

	DOF	Reflected Inertia	Payload	Normalized Eff. Mass
BioRob-X4	4	0.344 kg	20 N	0.017 kg/N
Stanford S2ρ	1	0.98 kg *	30.6 N *	0.032 kg/N *
human arm	7	2.11 kg *	62 N *	0.030 kg/N *
Stanford DM^2	3	3.51 kg *	60 N *	0.060 kg/N *
PUMA560	6	24.88 kg *	21.6 N *	1.15 kg/N *

Table 5.5.: Comparison of effective end-effector mass in collision direction for the configuration shoulder $q_S = 0^\circ$, elbow $q_E = 0^\circ$, and wrist joint $q_W = -90^\circ$ (cf. [22]). Values marked with † taken from [22], values with ‡ from [12].

	DOF	Reflected Inertia	Payload	Normalized Eff. Mass
BioRob-X4	4	0.104 kg	20 N	0.005 kg/N
DLR LWR 3	7	4 kg †	147 N ‡	0.027 kg/N

The effective end-effector mass of 1.66 kg for elastic joint actuators compared to 122 g for elastic tendon actuators demonstrates that a major portion of the maximum payload of 20 N is needed to support the robot structure when using elastic actuators with motors placed in the joints. In case of elastic tendon actuators, the weight of the distant links is reduced and counterbalanced, such that only a minimal portion of the maximum payload is required to overcome the gravitational forces.

The evaluation of the effect of motor current limiting fuses showed that the peak impact force can not be reduced without imposing major limitations on the robot arm dynamics. This holds for general joint torque limiting devices when used in the presented scenario and high velocities. However, clamping forces and joint torques can be limited by these devices in order to protect the hardware and environment from excessive stress caused by clamping in case the control software fails. Therefore, motor current fuses are sufficient and even beneficial compared to mechanical joint torque limitation devices by saving weight and complexity. With elastic tendons, the torque shocks after a fuse switch-off are low pass filtered and are not reversed abruptly as in the case of stiff actuation, again being protective for the hardware.

In summary, elastic tendon actuation can enable excellent safety properties for high speed pHRI applications with high safety requirements by reducing the link inertia and decoupling motors and links.

Not covered in detail in this evaluation is the fact that elastic actuation can store energy and can lead to significantly higher joint than motor velocities. The simulation results indicate that

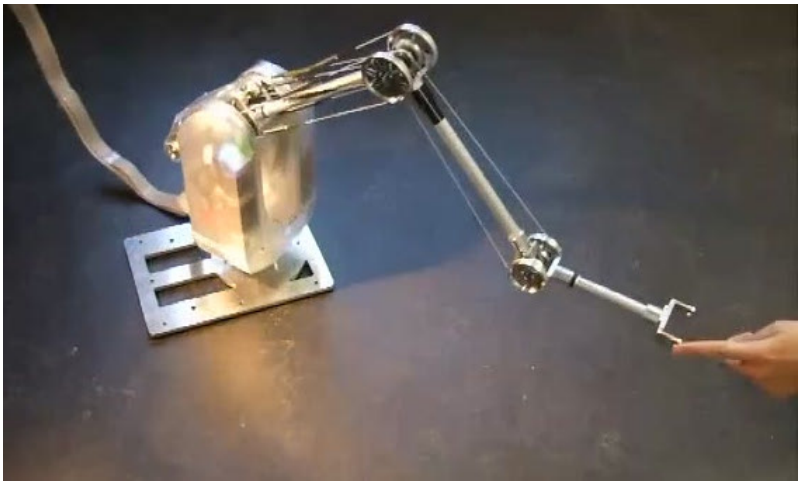

Figure 5.20.: Active collision detection and reaction [35].

the negative effect of elastic actuation on the collision properties is much lower in case of elastic tendon actuation with only a 2 % increase in kinetic energy, compared to elastic joint actuation with an increase of 19 %, at least for the unloaded state.

5.4 Conclusions

This chapter focused on the development of an online, model-based safety evaluation method of the BioRob robot arm. In Section 5.1, a realistic impact model incorporating contact, friction and stiction forces was developed and experimentally validated. The impact model combines a Hunt-Crossley contact model with a finite state machine for friction and stiction simulation.

In Section 5.2, a model-based safety estimation method for the estimation of maximum impact and clamping forces based on the current state of the robot arm was developed. The estimation method was experimentally validated against impact tests using a force plate. In addition, the MBS dynamics model and the contact model from Section 5.1 were used to compare the simulation with the experimental measurements and the analytical estimation method. The comparison between experiment, simulation, and numerical computation yielded very good qualitative and quantitative results. As minor obvious limitations, the proposed method is not capable of predicting an upper limit of the collision force/pressure for collisions with moving objects and manipulation of sharp objects. In these extreme cases, only additional pre-contact safety measures may prove helpful.

After experimental validation of the simulation models and the model-based safety estimation method, the impact safety behavior of four types of actuators, elastic tendon actuation (ETA), stiff tendon actuation (STA), elastic joint actuation (EJA), and stiff joint actuation (SJA), was compared in Section 5.3 by means of simulation and the developed safety evaluation method. The comparison clearly showed that ETA leads to a reduction of up to 90 % of the safety related properties compared to SJA. Reducing the transmission elasticity of the ETA used in the BioRob robot arm leads to higher impact forces, indicating that the rotor and link inertia decoupling is reduced by increasing the transmission stiffness.

The passive safety properties of the robot arm can be improved by collision detection and reaction methods. Because of the compliant and lightweight mechanical design, collision de-

tection of low force impacts is made possible using the joint positions in addition to the motor currents (cf. Figure 5.20) [30, 21]. Collision detection can be used to further reduce impact forces. In combination with pre-collision strategies such as proposed in [23, 33], the impact forces could be limited to very low values with only slight performance reduction.

6 Summary and Conclusions

This thesis aimed at developing and validating mathematical foundations and methods required for the dynamic modeling, control and safety analysis of highly compliant and lightweight robot arms that are targeted at high speed pHRI applications. The BioRob-X4 robot arm characterized by four DOF and highly elastic tendon actuation with kinematic coupling served as experimental robotic platform.

Kinematic and Dynamic Modeling of the BioRob-X4 Robot Arm

An important part of this dissertation is comprised of the modeling of the actuators and of the rigid robot arm body dynamics. In contrast to other robot arm designs, the actuation principle of the BioRob arm is non-modular in order to enable an extreme lightweight and low-inertia design. The use of tendons, stretching over multiple joints, and of extension coil springs, maintaining tendon tension and decoupling link and rotor inertia, introduces kinematic coupling and undesirable joint oscillations, respectively.

These effects had to be modeled accurately to investigate the behavior of the actuators and of the whole arm dynamics in theory, simulation, and experiment. As a main contribution of this work, new detailed mathematical models of the coupled elastic tendon actuators and of the BioRob robot arm dynamics have been developed in Chapter 3. Compared to common elastic joint robot arms, the kinematic coupling introduced by the elastic tendons and the additional pulley transmission required the development of new dynamic models for the investigated robot arm. The main challenge in the modeling process was the development of a systematic approach to deal with the additional complexity introduced by the kinematic tendon coupling, the pulley transmission, and the integrated tendon springs.

In Section 3.2, a detailed mathematical model of a single joint elastic tendon actuator has been presented. The section covered the detailed discussion of the resulting characteristic output stiffness and damping curves divided into a high stiffness area with the combined stiffness of the agonist and the antagonist springs and into two low stiffness areas dominated by the single stiffness of either the agonist or antagonist spring. The conditions for the occurrence of static or dynamic tendon slackening were derived based on the geometric pulley parameters, the coil spring parameters, and the prestretching force. From these findings, design guidelines were presented for setting the prestretching force to maximize the high stiffness area, or to cancel out most of the static friction caused by the tendons in order to obtain an almost linear characteristic stiffness curve in the linear stretching areas of the springs. The section concluded with an overview of the dynamic models of the electrical motors and described how the actuator states and properties can be reflected, i.e. transformed, to the actuator output.

Following the modeling of a single joint actuator, Section 3.3 covered the kinematic model of the whole robot arm including the kinematic coupling introduced by the tendons spanning multiple joints. A tendon coupling matrix was defined which was used to transform positions, velocities and torques across the tendon coupling between the elastic actuator state space and the joint state space. The definition of these state spaces supports the goal of this dissertation regarding the reduction of model complexity by consistent definition of state spaces and transformation matrices.

By means of the different state space definitions, the dynamics model of the robot arm could be formulated in joint space, as described in Section 3.4. For this purpose, the model states and parameters were reflected to joint space. Section 3.4.1 described the reflection of the elastic actuation matrices and torques. Section 3.4.2 offered an overview over the different state spaces that were utilized to divide the robot arm model and the corresponding transformation matrices used to transform position, velocity, and torque vectors between these state spaces. Using the states and parameters transformed to joint space, the complete robot arm dynamics in joint space could be described using the reduced model of elastic joint robots proposed in literature. The generation of these dynamics models can be considered as the important foundation for the development of model-based observer, control, and monitoring methods presented in the following chapters.

Simulation and Experimental Validation

The requirements posed on the simulation environment comprised the accurate solution of highly transient behavior and stiff ordinary differential equations, such as high speed impacts with high collision stiffness. Further, finite state machine models representing static and dynamic friction as well as the simulation of the motor inductance with a time constant of a fraction of a millisecond combined with elastic joints with a characteristic frequency of a tenth of a second to one second played an important role. In this regard, many robotic simulators focus on real-time simulation rather than fidelity of the solution and, further, do not support variable step-width or stiff solvers.

Section 3.5 described the implementation of the presented models in a simulation library and the developed object-oriented simulation framework using a technical computing software package. The focus of the developed simulation package was placed on the analysis of experimental measurement data and high-resolution simulation of collision and impact behavior of different actuator designs. The combination of a model-based programming approach for the dynamics models and a class-based programming approach for the parameter storage proved to be particularly useful in order to deal with the challenging model complexity.

Using the developed simulator and measurement data from experiments with the BioRob-X4 arm, the MBS dynamics model was validated by identification of the essential model parameters in Section 3.6.1. Because of the non-modular actuation design of the robot arm, it was not possible to conduct the parameter identification with single, dismantled actuators or links. Instead, the identification of the model had to be carried out using the complete robot arm. Despite the challenging robot dynamics design, the identification process yielded a sufficiently good agreement of the parametrized model with the real robot platform for the measured experimental data, as shown in Section 3.6.2.

Dynamic Analysis and Control

In Chapter 4, methods for filtering and control of the robot arm were presented. One of the main challenges was to regain a reliable joint position signal from the medium-resolution position sensor measurements. To obtain the highest possible position measurement accuracy, a novel joint position sensor calibration method achieving a major improvement of the joint position measurement data has been developed in Section 4.1.1.

As described in Section 4.1.2, the joint velocity can be obtained by numerical differentiation from the calibrated joint position data. Nevertheless, a special filter was additionally required, because the resulting raw velocity data was rendered useless due the extremely high level of numerical noise. One of the main reasons requiring special filtering effort was the wide velocity range caused by the elastic decoupling of motors and joints which enable much higher joint than motor velocities. A switching Kalman filter with three stages was proposed to obtain high velocity smoothing at low velocities, in order not to excite the highly elastic system at steady state, and fast dynamics at higher velocities, in order to be able to efficiently damp undesired joint oscillations. The filter was successfully implemented and tested on the hardware.

Using the dynamics equation formulation in joint space derived in Chapter 3, a joint space inverse dynamics model control method was proposed in Section 4.3.1. A controller with tendon decoupling and gravity compensation was derived in Section 4.3.2 and evaluated in simulation with respect to trajectory smoothness and robustness in Section 4.3.3 and also in experiment using a realistic pick-and-place scenario in Section 4.3.4.

Safety Evaluation

One of the main requirements of applications with close pHRI is undoubtedly safety. The design of the BioRob robot arm under investigation is completely targeted at minimizing inertia of moving links while maintaining reasonable performance. Chapter 5 therefore concentrated on clarifying the behavior of the robot arm in contact situations and quantifying its safety properties compared to different actuation designs.

An important building block for safety analysis is the modeling of realistic contact and impact behavior. Section 5.1 illustrated the developed contact model in simulation based on Hunt-Crossley material equations from literature. Realistic contact modeling is a complex topic on its own. Thus, a main contribution of this chapter has been the detailed description of its implementation and validation in simulation and experiment using a force plate. The experiment with a bouncing ball with a stiffness comparable to parts of the human body showed high congruence of the bouncing behavior with respect to the timing, impact duration, impact peak force, and impact curve shape between simulation and experimental data.

For using a robot arm in the vicinity of humans, a realistic safety estimation of the current robot state is necessary. Section 5.2 has proposed a new method based on the kinetic and potential robot energy to calculate and estimate the impact and clamping forces occurring in the worst case. The method was validated in impact experiments using a high-resolution force plate. The simulation of these impacts using the impact models developed in the aforementioned sections yielded quite comparable results. The calculated impact peak force using the energy-based method proved to be a fair estimation of the maximum impact peak force. The extension of the safety estimation of highly elastic robotic arms by considering the potential energy stored in the springs and the potential gravitational energy of the links as a source of kinetic energy with impact potential represents the main contribution of this chapter. As could be shown, the potential energy of the robot arm can be significantly higher than its current kinetic energy, especially in contact and clamping situations. A supervising and reaction guideline was proposed to deal with the safety issues of the robot arm's potential energy.

Chapter 5.3 was concerned with the quantification of the safety properties of the robot design under investigation. As comparison, alternative designs without tendon actuation or with varying transmission elasticity were also evaluated in detail. To ensure comparability, the BioRob arm

was chosen as common robotic platform for all the evaluated actuation designs. After the definition of a high-speed worst case trajectory, safety properties such as the collision peak force, joint torque, kinetic and potential energy, and operational space inertia were analyzed. As could be clearly shown, counterbalancing with a specific placement of the motors using tendons and reflected motor inertia decoupling by means of elastic transmission elements can reduce the relevant impact properties by more than 90 %.

Because several torque limiting devices have been presented over the last years in literature, reporting a significant increase of safety properties, Section 5.3.3 also investigated the effect of these devices on the given high-speed scenario. It could be shown that no reduction in impact peak force could be achieved by using joint level devices that decouple the motor and the link in case a specific torque limit is exceeded. Nevertheless, excessive clamping forces could be prevented. It can be concluded that for high-speed applications, only a robot arm design with minimal inertia is sufficient to meet the high safety requirements.

Conclusions

This thesis has laid the foundations for the practical use of the BioRob robot arm for applications with high safety and performance requirements for close pHRI. Novel analytical kinematics and dynamics models of the robot arm and its actuators, a model-based tracking control method, and an on-line collision and clamping safety estimation method based on the dynamics and kinematics model have been developed. The experimental validation has showed that the methods can be used to operate the robot arm in pHRI applications and that, moreover, a high level of both safety and performance is achieved for high speed applications.

The mathematical modeling and analysis of the Elastic Tendon Actuators (ETA) yielded the following highly essential results:

- Setting the spring preloading force allows to shape the characteristic impedance (e. g. stiffness and damping) curve of the actuator. Guidelines have been derived to use this property effectively in order to minimize the effect of Coulomb friction. By using tendons with preloaded springs, play in the transmission and the joint is largely reduced.
- In addition to the springs integrated in the tendons, viscous damping elements can be used in parallel to the springs to reduce undesired oscillations of the joint relative to the motor. Within the scope of this thesis it was found, however, that in case of significant viscous damping dynamic tendon slackening can occur easily, which is generally undesirable because it can cause lateral oscillations of the springs.
- Using springs in the tendons does not only protect the geared motor or the environment in case of a collision by means of low pass filtering the shock. The tendon itself is also protected. The ETA therefore does not suffer from the short life span and abrupt rupture common in cable actuation without built-in springs.
- Tendon-pulley actuation can also relieve the lightweight link structure from bending stress and therefore enable even more lightweight link design. This topic is not covered in detail in this thesis, but more information can be found in [44].

Further, the derivation of the full dynamics model has showed that compared to common elastic joint robot arm dynamics models, the tendon coupling and the additional transmission

ratio of the pulleys lead to increased complexity. The dynamics equations of the BioRob-X4 arm are described by

- 16 state variables (four state variables per joint), whereas rigidly actuated robot arms can be described by only two state variables per joint,
- 133 non-trivial model parameters, 72 controller parameters, 17 joint sensor filter parameters, and
- additional sensor calibration data and characteristic curves.

To handle the model complexity, a systematic state space partitioning approach has been proposed. Parameters and state variables defined in a certain state space can be thereby transformed into another state space. For example, the motor inertia can be reflected to the joint side across the gearbox, the pulleys, and the tendon kinematics by using state space transformation from the motor space to the joint space. The transformation of motor parameters to the joint side is for instance used in the model-based safety evaluation method to evaluate the effective motor inertia that is felt during a collision with the robot arm.

This dissertation has aimed on the one hand at demonstrating that the robot arm remains safe for close pHRI even in high velocity applications, and on the other hand at developing methods that support this behavior. The following main insights regarding high speed collision safety of the BioRob arm have been obtained:

- The presented elastic tendon actuation (ETA) design approach improves safety related properties of the robot arm, such as the impact energy and the effective end-effector mass, by about 90 % compared to a comparable robot arm with stiff joint actuation (SJA) and the same reflected model parameters. Moreover, the comparable robot arm with SJA uses most of its available motor torque for gravity compensation and would in reality also need heavier links to avoid elastic link effects.
- Using ETA instead of SJA therefore boosts the acceleration ability and the maximum velocity (7 ms for the BioRob-X4).
- At these high velocities safety mechanisms are not able to reduce the impact force peak, in contrast to studies presented in literature that were performed at lower velocities. For high speed applications, inherent safety by extreme reduction of the link weights is therefore mandatory.

The development of control methods for the highly compliant robot arm has constituted a great challenge. Based on the inverse model calculation of the desired motor trajectory we have proposed a tracking control law. The calculation of the desired motor trajectory makes use of the developed state space transformation method to transform the desired joint trajectory through the elastic tendon coupling and the pulley and gearbox transmission to the motor side. With the proposed controller and joint velocity sensor filters, a typical pick-and-place scenario was experimentally implemented. The absolute accuracy proved to be sufficient to successfully perform the task with trajectory velocities up to 2 $^{m}/_{s}$.

Bibliography

[1] *ISO 10218-1:2009, Robots for industrial environments - Safety requirements - Part 1: Robot*, Std., 2009.

[2] A. Albu-Schäffer, S. Wolf, O. Eiberger, S. Haddadin, F. Petit, and M. Chalon, "Dynamic modelling and control of variable stiffness actuators," in *Proceedings of the IEEE International Conference on Robotics and Automation*, 2010, pp. 2155 –2162.

[3] (2011, Feb.) BG/BGIA risk assessment recommendations according to machinery directive - design of workplaces with collaborative robots. BGIA – Institute for Occupational Safety and Health of the German Social Accident Insurance. [Online]. Available: http://www.dguv.de/ifa/en/pra/kollaborierende_roboter/index.jsp

[4] A. Bicchi, M. Bavaro, G. Boccadamo, D. De Carli, R. Filippini, G. Grioli, M. Piccigallo, A. Rosi, R. Schiavi, S. Sen, and G. Tonietti, "Physical human-robot interaction: Dependability, safety, and performance," in *Proceedings of the 10th International Workshop on Advanced Motion Control*, 2008, pp. 9 –14.

[5] A. Bicchi, M. A. Peshkin, and J. E. Colgate, *Springer Handbook of Robotics*. Springer-Verlag, 2008, ch. Safety for Physical Human-Robot Interaction, pp. 1335–1348.

[6] A. Bicchi and G. Tonietti, "Fast and "soft-arm" tactics," *IEEE Robotics and Automation Magazine*, vol. 11, no. 2, pp. 22 – 33, 2004.

[7] BioRobAssist project website, http://www.biorobassist.de.

[8] C. Breazeal, A. Takanishi, and T. Kobayashi, *Springer Handbook of Robotics*. Springer-Verlag, 2008, ch. Social Robots that Interact with People, pp. 1349–1369.

[9] H. Buchanan and J. Midgley, "Evaluation of pain threshold using a simple pressure algometer." *Clinical Rheumatology*, vol. 6(4), pp. 510–517, 1987.

[10] A. De Luca, "Feedforward/feedback laws for the control of flexible robots," in *Proceedings of the IEEE International Conference on Robotics and Automation*, vol. 1, 2000, pp. 233–240.

[11] A. De Luca and W. Book, *Springer Handbook of Robotics*. Springer, 2008, ch. Robots with Flexible Elements, pp. 287–319.

[12] DLR Light-Weight Robot LWR III data sheet. DLR. [Online]. Available: http://www.dlr.de/rm/Portaldata/52/Resources/dokumente/light_weight_robot/dlr-lbriii-eng_homepage.pdf

[13] H. Dresig and F. Holzweißig, *Dynamics of Machinery - Theory and Applications*. Springer, 2010.

[14] S. K. Dwivedy and P. Eberhard, "Dynamic analysis of flexible manipulators, a literature review," *Mechanism and Machine Theory*, vol. 41, no. 7, pp. 749 – 777, 2006.

[15] W. Goldsmith, *Impact - The Theory and Physical Behaviour of Colliding Solids*. Dover, 2001.

[16] M. Grebenstein, M. Chalon, W. Friedl, S. Haddadin, T. Wimböck, G. Hirzinger, and R. Siegwart, "The hand of the DLR Hand Arm system: Designed for interaction," *The International Journal of Robotics Research*, vol. 31, no. 13, pp. 1531–1555, 2012.

[17] A. Haddadi and K. Hashtrudi-Zaad, "Real-time identification of Hunt-Crossley dynamic models of contact environments," *IEEE Transactions on Robotics*, vol. PP, no. 99, pp. 1–12, 2012.

[18] S. Haddadin, A. Albu-Schäffer, M. Frommberger, and G. Hirzinger, "The role of the robot mass and velocity in physical human-robot interaction - part ii: Constrained blunt impacts," in *Proceedings of the IEEE International Conference on Robotics and Automation*, 2008, pp. 1339 –1345.

[19] S. Haddadin, A. Albu-Schäffer, F. Haddadin, J. Rosmann, and G. Hirzinger, "Study on soft-tissue injury in robotics," *IEEE Robotics and Automation Magazine*, vol. 18, no. 4, pp. 20 –34, 2011.

[20] S. Haddadin, A. Albu-Schäffer, and G. Hirzinger, "Soft-tissue injury in robotics," in *Proceedings of the IEEE International Conference on Robotics and Automation*, 2010, pp. 3426 –3433.

[21] S. Haddadin, A. Albu-Schäffer, A. De Luca, and G. Hirzinger, "Collision detection and reaction: A contribution to safe physical human-robot interaction," in *Proceedings of the IEEE/RSJ International Conference on Intelligent Robots and Systems*, 2008, pp. 3356–3363.

[22] S. Haddadin, A. Albu-Schäffer, and G. Hirzinger, "Requirements for safe robots: Measurements, analysis and new insights," *The International Journal of Robotics Research*, vol. 28, no. 11-12, pp. 1507–1527, 2009.

[23] J. Heinzmann and A. Zelinsky, "Quantitative safety guarantees for physical human-robot interaction," *The International Journal of Robotics Research*, vol. 22, no. 7-8, pp. 479–504, Jul. 2003.

[24] K. H. Hunt and F. R. E. Crossley, "Coefficient of restitution interpreted as damping in vibroimpact," *Journal of Applied Mechanics*, vol. 42, no. 2, pp. 440–445, 1975.

[25] J. W. Hurst, A. A. Rizzi, and D. Hobbelen, "Series elastic actuation: Potential and pitfalls," in *Proceedings of the 7th International Conference on Climbing and Walking Robots and the Support Technologies for Mobile Machines*. Springer Verlag, 2004.

[26] K. Jensen, H. Andersen, J. Olesen, and U. Lindblom, "Pressure-pain threshold in human temporal region: evaluation of a new pressure algometer." *Pain*, vol. 25(3), pp. 313–323, 1986.

[27] I. Kao, K. Lynch, and J. W. Burdick, *Handbook of Robotics*. Springer, 2008, ch. Contact Modeling and Manipulation, pp. 647 – 669.

[28] O. Khatib, "A unified approach for motion and force control of robot manipulators: The operational space formulation," *IEEE Journal of Robotics and Automation*, vol. 3, no. 1, pp. 43 –53, 1987.

[29] ——, “Inertial properties in robotic manipulation: An object-level framework,” *The International Journal of Robotics Research*, vol. 14, no. 1, pp. 19–36, 1995.

[30] J. Kirchhoff, “Parameter identification for a non-modular elastic joint robot arm for observer-based collision detection,” Master’s thesis, Technische Universität Darmstadt, 2011.

[31] S. Klug, T. Lens, O. von Stryk, B. Möhl, and A. Karguth, “Biologically inspired robot manipulator for new applications in automation engineering,” in *Proceedings of the 5th German Conference on Robotics*, 2008.

[32] H. Kobayashi, K. Hyodo, and D. Ogane, “On tendon-driven robotic mechanisms with redundant tendons,” *The International Journal of Robotics Research*, vol. 17, no. 5, pp. 561–571, 1998.

[33] D. Kulić and E. Croft, “Pre-collision safety strategies for human-robot interaction,” *Autonomous Robots*, vol. 22, pp. 149–164, 2007.

[34] T. Lens, A. Karguth, and O. von Stryk, “Safety properties and collision behavior of robotic arms with elastic tendon actuation,” in *Proceedings of the 7th German Conference on Robotics*, 2012.

[35] T. Lens, J. Kunz, C. Trommer, A. Karguth, and O. von Stryk, “Biorob-arm: A quickly deployable and intrinsically safe, light-weight robot arm for service robotics applications,” in *Proceedings of the 41st International Symposium on Robotics / 6th German Conference on Robotics*, 2010.

[36] T. Lens, J. Kunz, and O. von Stryk, “Dynamic modeling of the 4 DoF BioRob series elastic robot arm for simulation and control,” in *Simulation, Modeling, and Programming for Autonomous Robots*, ser. Lecture Notes in Artificial Intelligence. Springer, 2010, pp. 411–422.

[37] T. Lens, K. Radkhah, and O. von Stryk, “Simulation of dynamics and realistic contact forces for manipulators and legged robots with high joint elasticity,” in *Proceedings of the 15th International Conference on Advanced Robotics*, 2011, pp. 34–41.

[38] T. Lens and O. von Stryk, “Investigation of safety in human-robot-interaction for a series elastic, tendon-driven robot arm,” in *Proceedings of the IEEE/RSJ International Conference on Intelligent Robots and Systems*, 2012, pp. 4309–4314.

[39] ——, “Design and dynamics model of a lightweight series elastic tendon-driven robot arm,” in *Proceedings of the IEEE International Conference on Robotics and Automation*, 2013.

[40] T. Lens, J. Kirchhoff, and O. von Stryk, “Dynamic modeling of elastic tendon actuators with tendon slackening,” in *IEEE-RAS International Conference on Humanoid Robots*, 2012.

[41] S. Ma, H. Yoshinada, and S. Hirose, “CT ARM-I: coupled tendon-driven manipulator model I – design and basic experiments,” in *Proceedings of the IEEE International Conference on Robotics and Automation*, 1992, pp. 2094 –2100 vol.3.

[42] D. Marhefka and D. Orin, "Simulation of contact using a nonlinear damping model," in *Proceedings of the IEEE International Conference on Robotics and Automation*, vol. 2, 1996, pp. 1662 –1668 vol.2.

[43] R. Marino and S. Nicosia, "On the feedback control of industrial robots with elastic joints: A singular perturbation approach," University of Rome, Tech. Rep. R-84.01, 1984.

[44] B. Möhl, "Bionic robot arm with compliant actuators," in *Proceedings of Sensor Fusion and Decentralized Control in Robotic Systems III*, 2000, pp. 82–85.

[45] T. Morita, H. Iwata, and S. Sugano, "Development of human symbiotic robot: Wendy," in *Proceedings of the IEEE International Conference on Robotics and Automation*, vol. 4, 1999, pp. 3183 –3188.

[46] S. Murphy, J. Wen, and G. Saridis, "Simulation and analysis of flexibly jointed manipulators," in *Proceedings of the 29th IEEE Conference on Decision and Control*, 1990, pp. 545 –550 vol.2.

[47] R. M. Murray, Z. Li, and S. S. Sastry, *A Mathematical Introduction to Robotic Manipulation*. CRC, Boca Raton, 1994.

[48] K. Nilsson, R. Johansson, A. Robertsson, R. Bischoff, T. Brogårdh, and M. Hägele, "Productive robots and the SMErobot project," in *Proceedings of the Third Swedish Workshop on Autonomous Robotics*, 2005.

[49] R. Ozawa, K. Hashirii, and H. Kobayashi, "Design and control of underactuated tendon-driven mechanisms," in *Proceedings of the IEEE International Conference on Robotics and Automation*, 2009, pp. 1522 –1527.

[50] G. Palli, G. Borghesan, and C. Melchiorri, "Modeling, identification, and control of tendon-based actuation systems," *IEEE Transactions on Robotics*, vol. 28, no. 2, pp. 277 –290, april 2012.

[51] J. Park, S. Haddadin, J. Song, and A. Albu-Schäffer, "Designing optimally safe robot surface properties for minimizing the stress characteristics of human-robot collisions," in *Proceedings of the IEEE International Conference on Robotics and Automation*, 2011, pp. 5413 –5420.

[52] G. Pratt and M. Williamson, "Series elastic actuators," *Proceedings of the IEEE/RSJ International Conference on Intelligent Robots and Systems*, vol. 1, p. 399, 1995.

[53] G. Prisco and M. Bergamasco, "Dynamic modelling of a class of tendon driven manipulators," in *Proceedings of the International Conference on Advanced Robotics*, 1997, pp. 893 –899.

[54] B. Rooks, "The harmonious robot," *Industrial Robot: An International Journal*, vol. 33, pp. 125–130, 2006.

[55] A. Rost and A. Verl, "The quadhelix-drive - an improved rope actuator for robotic applications," in *Proceedings of the IEEE International Conference on Robotics and Automation*, 2010, pp. 3254 –3259.

[56] K. Salisbury, "Issues in human/computer control of dexterous remote hands," *IEEE Transactions on Aerospace and Electronic Systems*, vol. 24, no. 5, pp. 591 –596, sep 1988.

[57] R. Schiavi, G. Grioli, S. Sen, and A. Bicchi, "VSA-II: a novel prototype of variable stiffness actuator for safe and performing robots interacting with humans," in *Proceedings of the IEEE International Conference on Robotics and Automation*, 2008, pp. 2171–2176.

[58] D. Shin, I. Sardellitti, Y.-L. Park, O. Khatib, and M. Cutkosky, "Design and control of a bio-inspired human-friendly robot," *The International Journal of Robotics Research*, vol. 29, no. 5, pp. 571–584, 2010.

[59] M. W. Spong, "Modeling and control of elastic joint robots," *Journal of Dynamic Systems, Measurement, and Control*, vol. 109, no. 4, pp. 310–318, 1987.

[60] P. Tomei, "An observer for flexible joint robots," *IEEE Transactions on Automatic Control*, vol. 35, no. 6, pp. 739 –743, 1990.

[61] ——, "A simple PD controller for robots with elastic joints," *IEEE Transactions on Automatic Control*, vol. 36, no. 10, pp. 1208–1213, 1991.

[62] M. Van Damme, B. Vanderborght, B. Verrelst, R. Van Ham, F. Daerden, and D. Lefeber, "Proxy-based sliding mode control of a planar pneumatic manipulator," *The International Journal of Robotics Research*, vol. 28, no. 2, pp. 266–284, 2009.

[63] R. Van Ham, T. Sugar, B. Vanderborght, K. Hollander, and D. Lefeber, "Compliant actuator designs," *IEEE Robotics and Automation Magazine*, vol. 16, no. 3, pp. 81–94, 2009.

[64] B. Vanderborght, B. Verrelst, R. Van Ham, M. Van Damme, D. Lefeber, B. M. Y. Duran, and P. Beyl, "Exploiting natural dynamics to reduce energy consumption by controlling the compliance of soft actuators," *The International Journal of Robotics Research*, vol. 25, no. 4, pp. 343–358, 2006.

[65] M. Vermeulen and M. Wisse, "Intrinsically safe robot arm: Adjustable static balancing and low power actuation," *International Journal of Social Robotics*, vol. 2, pp. 275–288, 2010.

[66] J. Versace, "A review of the severity index," in *Proceedings of the 15th Stapp Conf.*, 1971, pp. 771–796.

[67] Y.-T. Wang, V. Kumar, and J. Abel, "Dynamics of rigid bodies undergoing multiple frictional contacts," in *Proceedings of the IEEE International Conference on Robotics and Automation*, May 1992, pp. 2764 –2769 vol.3.

[68] M. Wassink and S. Stramigioli, "Towards a novel safety norm for domestic robotics," in *Proceedings of the IEEE/RSJ International Conference on Intelligent Robots and Systems*, 2007, pp. 3354 –3359.

[69] S. Wolf and G. Hirzinger, "A new variable stiffness design: Matching requirements of the next robot generation," in *Proceedings of the IEEE International Conference on Robotics and Automation*, 2008, pp. 1741 –1746.

[70] K. Yamane and Y. Nakamura, "Dynamics filter - concept and implementation of online motion generator for human figures," *IEEE Transactions on Robotics and Automation*, vol. 19, no. 3, pp. 421 – 432, 2003.

[71] M. Zinn, O. Khatib, B. Roth, and J. Salisbury, "Playing it safe [human-friendly robots]," *IEEE Robotics and Automation Magazine*, vol. 11, no. 2, pp. 12 – 21, 2004.

[72] M. Zinn, B. Roth, O. Khatib, and J. K. Salisbury, "A new actuation approach for human friendly robot design," *The International Journal of Robotics Research*, vol. 23, no. 4-5, pp. 379–398, 2004.

Wissenschaftlicher Werdegang[1]

Der Lebenslauf ist in der Online-Verison aus Gründen des Datenschutzes nicht enthalten.

Erklärung[2]

Hiermit erkläre ich, dass ich die vorliegende Arbeit, mit Ausnahme der ausdrücklich genannten Hilfsmittel, selbständig verfasst habe.

[1] gemäß § 20 Abs. 3 der Promotionsordnung der TU Darmstadt
[2] gemäß § 9 Abs. 1 der Promotionsordnung der TU Darmstadt

A Simulation Model

A.1 Class Structure of a Robotic Arm in the Simulation Framework

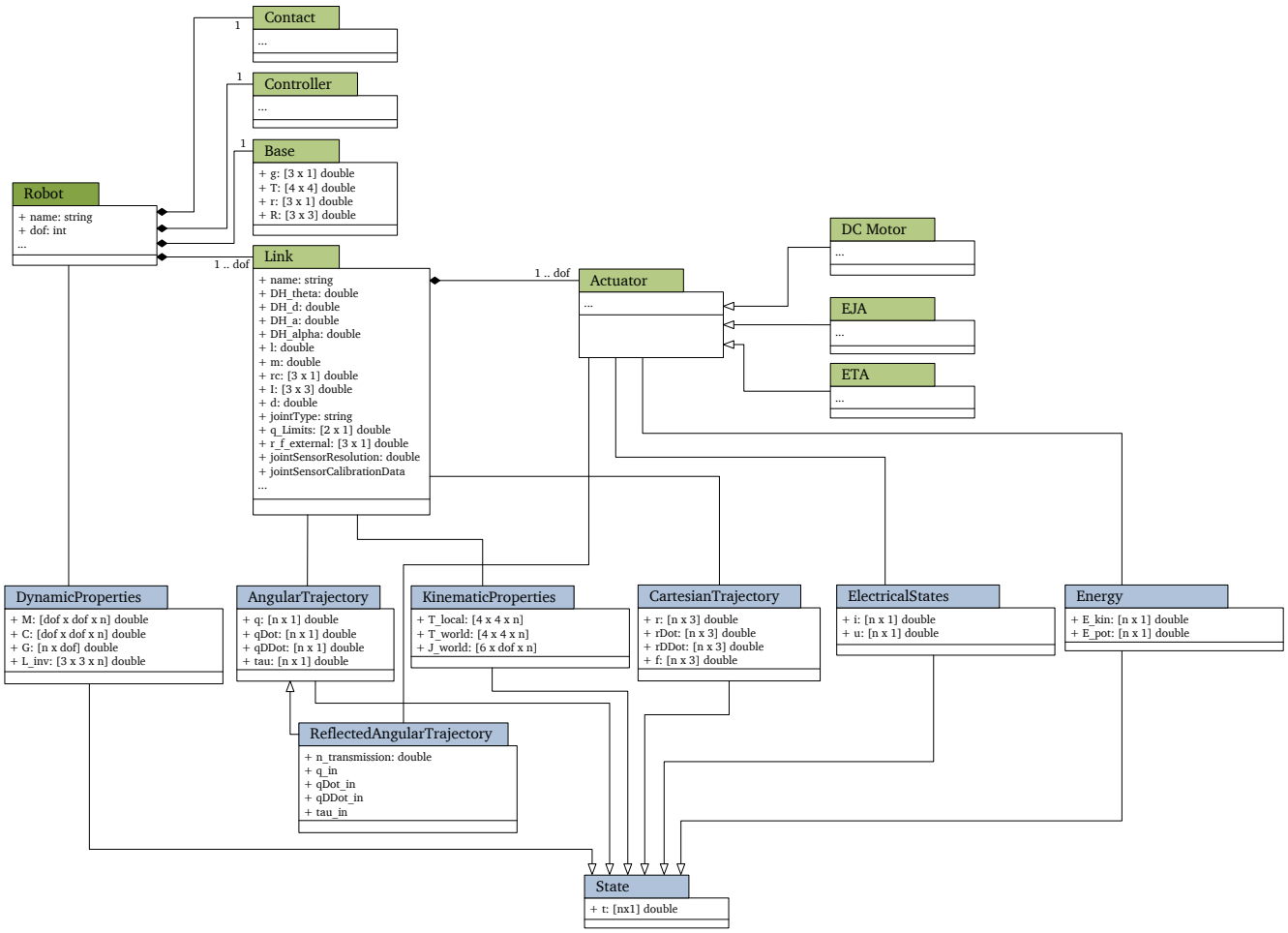

Figure A.1.: Class structure of the developed toolbox for simulation of robot arms with elastic tendon actuation.

A.2 Simulation Script for Initialization of BioRob-X4 Parameters

```
function robot = BioRob_X4_Parameters( gripperInstalled )

% ======================================================================
% Gripper Configuration
% ======================================================================
% -- Electrical gripper (Schunk) installed?
if nargin < 1
        gripperInstalled = false;
```

```
end

% ======================================================================
% Init
% ======================================================================
robot = EjRobot.Robot();
robot.createSerialLinkRobot(4);
robot.Link(4).Actuator = EjRobot.Actuators.CoupledSeriesElasticTendonVoltageMotor();

robot.name = 'BioRob_X4_SIM_JK_2011_07_18_v2';
robot.simulationModel = 'Model_4DoF_EJT_qd';

% ======================================================================
% Global Parameters
% ======================================================================
% -- Gravitational acceleration [m/s^-2].
g = [0, 0, -1];
g = g / norm(g) * 9.81;
robot.Base.g = g;

% -- Manipulator base position [3x1] [m].
robot.Base.r = [0, 0, 0]';

% -- Manipulator base orientation [3x1] [m].
robot.Base.R = eye(3, 3);

% ======================================================================
% Elastic Joint Manipulator Parameters
% ======================================================================
% ----------------------------------------------------------------------
% -- Manipulator parameters
% ----------------------------------------------------------------------
robot.Link(1).DH_theta = 0;
robot.Link(1).DH_d = 0.276;
robot.Link(1).DH_a = 0;
robot.Link(1).DH_alpha = pi/2;

robot.Link(2).DH_theta = 0;
robot.Link(2).DH_d = 0;
robot.Link(2).DH_a = 0.307;
robot.Link(2).DH_alpha = 0;

robot.Link(3).DH_theta = 0;
robot.Link(3).DH_d = 0;
robot.Link(3).DH_a = 0.310;
robot.Link(3).DH_alpha = 0;

robot.Link(4).DH_theta = 0;
robot.Link(4).DH_d = 0;
if ~gripperInstalled
        robot.Link(4).DH_a = 0.10;
else
        robot.Link(4).DH_a = 0.17;
end
robot.Link(4).DH_alpha = 0;

% -- Symbolic functions
robot.symbolicMassMatrixFunction = @EjRobot.Symbolic.BioRob_X4h.M;
robot.symbolicCoriolisMatrixFunction = @EjRobot.Symbolic.BioRob_X4h.C;
robot.symbolicGravitationalVectorFunction = @EjRobot.Symbolic.BioRob_X4h.G;

% -- Angular offset of zero position of real robot hardware with respect to
%   DH formulation.
robot.Link(1).jointZeroPositionHardware = 0;
robot.Link(2).jointZeroPositionHardware = pi/2;
robot.Link(3).jointZeroPositionHardware = 0;
```

```
robot.Link(4).jointZeroPositionHardware = 0;

%-- Definition of the configuration with zero potential gravitational energy.
robot.zeroPotentialEnergyConfiguration = [0, -pi/2, 0, 0];

%-------------------------------------------------------------------------
%-- Manipulator: center of mass (COM) of the links [3x1] [m].
%-------------------------------------------------------------------------
%-- The COM position is given with respect to the
%   coordinate system CS_i, which is located in joint i+1, i.e. we
%   define  i^r_{ci} .
robot.Link(1).rc = [0, -robot.Link(1).l / 2, 0];
robot.Link(2).rc = [-robot.Link(2).l - 0.010, 0, 0];
robot.Link(3).rc = [-robot.Link(3).l / 2, 0, 0];
if ~gripperInstalled
        robot.Link(4).rc = [-robot.Link(4).l + 0.020, 0, 0];  %-- Without gripper
else
        robot.Link(4).rc = [-robot.Link(4).l + 0.100, 0, 0];  %-- With gripper
end

%-------------------------------------------------------------------------
%-- Manipulator: link masses [kg].
%-------------------------------------------------------------------------
robot.Link(1).m = 2.350;
robot.Link(2).m = 1.530;
robot.Link(3).m = 0.160;
if ~gripperInstalled
        robot.Link(4).m = 0.055;
else
        robot.Link(4).m = 0.204;
end

%-------------------------------------------------------------------------
%-- Manipulator: inertia of the links [kg*m^2]
%-------------------------------------------------------------------------
m = [robot.Link.m];
l = [robot.Link.l];
robot.Link(1).I = [(m(1)*l(1)^2)/12, 0, 0; 0, (m(1)*l(1)^2)/12, 0; 0, 0, (m(1)*0.1^2)/2];
robot.Link(2).I = [(m(2)*0.03^2)/2, 0, 0; 0, (m(2)*l(2)^2)/12, 0; 0, 0, (m(2)*l(2)^2)/12];
robot.Link(3).I = [(m(3)*0.02^2)/2, 0, 0; 0, (m(3)*l(3)^2)/12, 0; 0, 0, (m(3)*l(3)^2)/12];
robot.Link(4).I = [(m(4)*0.02^2)/2, 0, 0; 0, (m(4)*l(4)^2)/12, 0; 0, 0, (m(4)*l(4)^2)/12];

%-------------------------------------------------------------------------
%-- Joint damping
%-------------------------------------------------------------------------
%-- Viscous damping in the manipulator joints [Nms/rad].
robot.Link(1).d = 0.25;
robot.Link(2).d = 1.5;
robot.Link(3).d = 0.5;
robot.Link(4).d = 0;

%-------------------------------------------------------------------------
%-- Sensors
%-------------------------------------------------------------------------
%-- Joint sensor resolution [ticks/360°]
robot.Link(1).jointSensorResolution = 4096;
robot.Link(2).jointSensorResolution = 4096;
robot.Link(3).jointSensorResolution = 4096;
robot.Link(4).jointSensorResolution = 4096;

%-- Joint calibration data [jointResolution x N] [rad]
jointSensorOffsets = [];
load(fullfile(fileparts(mfilename('fullpath')), ...
        'BioRob_X4_SIM_2011_08_12_jointSensorOffsets.mat'));
robot.Link(1).jointSensorCalibrationData = jointSensorOffsets(:, 1);
robot.Link(2).jointSensorCalibrationData = jointSensorOffsets(:, 2);
```

```
robot.Link(3).jointSensorCalibrationData = jointSensorOffsets(:, 3);
robot.Link(4).jointSensorCalibrationData = jointSensorOffsets(:, 4);

% ── Motor sensor resolution  [ticks/360°]
robot.Link(1).Actuator.motorSensorResolution = 2000;
robot.Link(2).Actuator.motorSensorResolution = 2000;
robot.Link(3).Actuator.motorSensorResolution = 2000;
robot.Link(4).Actuator.motorSensorResolution = 2000;

% ──────────────────────────────────────────────────────────────────────
% ── Series elastic actuator parameters (DC motor + elastic transmission).
% ──────────────────────────────────────────────────────────────────────
% ── DC motor: torque constant [Nm/A].
robot.Link(1).Actuator.kt = 0.0259;
robot.Link(2).Actuator.kt = 0.0259;
robot.Link(3).Actuator.kt = 0.0259;
robot.Link(4).Actuator.kt = 0.0235;

% ── DC motor: gearbox ratio = omega_motor / omega_out [−].
robot.Link(1).Actuator.ng = 23;
robot.Link(2).Actuator.ng = 23;
robot.Link(3).Actuator.ng = 18;
robot.Link(4).Actuator.ng = 19;

% ── Pulley transmission ratio = omega_in / omega_out [−].
robot.Link(1).Actuator.np = 48/15;
robot.Link(2).Actuator.np = 80/23;
robot.Link(3).Actuator.np = 60/23;
robot.Link(4).Actuator.np = 50/18;

% ── DC motor: rotor inertia with respect to motor [kg*m^2].
robot.Link(1).Actuator.Ir = 3.33E−6;
robot.Link(2).Actuator.Ir = 3.33E−6;
robot.Link(3).Actuator.Ir = 3.33E−6;
robot.Link(4).Actuator.Ir = 1E−6;

% ── DC motor: gearbox inertia with respect to motor axis [kg*m^2].
robot.Link(1).Actuator.Ig = 0.8E−7;
robot.Link(2).Actuator.Ig = 0.8E−7;
robot.Link(3).Actuator.Ig = 0.8E−7;
robot.Link(4).Actuator.Ig = 0.5E−7;

% ──────────────────────────────────────────────────────────────────────
% ── DC motor: gearbox viscous damping with respect to motor [Nms/rad].
% ──────────────────────────────────────────────────────────────────────
robot.Link(1).Actuator.dvg = 1.5 * 1e−4;
robot.Link(2).Actuator.dvg = 1.5 * 1e−4;
robot.Link(3).Actuator.dvg = 0.5 * 1e−4;
robot.Link(4).Actuator.dvg = 1.5 * 1e−4;

% ──────────────────────────────────────────────────────────────────────
% ── DC motor: gearbox Coulomb damping with respect to joint [Nm].
% ──────────────────────────────────────────────────────────────────────
robot.Link(1).Actuator.dCg_joint = 0.23;
robot.Link(2).Actuator.dCg_joint = 0.28;
robot.Link(3).Actuator.dCg_joint = 0.06;
robot.Link(4).Actuator.dCg_joint = 0.70;

% ──────────────────────────────────────────────────────────────────────
% ── DC motor: speed constant [Vs/rad].
% ──────────────────────────────────────────────────────────────────────
robot.Link(1).Actuator.kv = (369*(2*pi/60))^−1;
robot.Link(2).Actuator.kv = (369*(2*pi/60))^−1;
robot.Link(3).Actuator.kv = (369*(2*pi/60))^−1;
robot.Link(4).Actuator.kv = (407*(2*pi/60))^−1;
```

```
% ------------------------------------------------------------------------
% -- DC motor: terminal resistance [Ohm].
% ------------------------------------------------------------------------
robot.Link(1).Actuator.Ra = 0.611;
robot.Link(2).Actuator.Ra = 0.611;
robot.Link(3).Actuator.Ra = 0.611;
robot.Link(4).Actuator.Ra = 2.19;

% ------------------------------------------------------------------------
% -- DC motor: terminal inductance [H].
% ------------------------------------------------------------------------
robot.Link(1).Actuator.La = 0.119 * 1e-3;
robot.Link(2).Actuator.La = 0.119 * 1e-3;
robot.Link(3).Actuator.La = 0.119 * 1e-3;
robot.Link(4).Actuator.La = 0.238 * 1e-3;

% ------------------------------------------------------------------------
% -- DC motor: terminal inductance differentiation time constant [s].
% ------------------------------------------------------------------------
robot.Link(1).Actuator.La_T = 1e-4;
robot.Link(2).Actuator.La_T = 1e-4;
robot.Link(3).Actuator.La_T = 1e-4;
robot.Link(4).Actuator.La_T = 1e-4;

% ------------------------------------------------------------------------
% -- DC motor: Maximum motor voltage [V].
% ------------------------------------------------------------------------
for k = 1 : 4
        robot.Link(k).Actuator.max_motor_voltage = 12; % [V]
end

% ------------------------------------------------------------------------
% -- DC motor: Maximum fuse current [A].
% ------------------------------------------------------------------------
I_max = 6.3; % [A]
for k = 1 : 4
        robot.Link(k).Actuator.max_motor_torque = I_max * robot.Link(k).Actuator.kt;
end

% ------------------------------------------------------------------------
% -- Elastic transmission: mechanical spring stiffnesses with respect to
%    joint [Nm/rad].
% ------------------------------------------------------------------------
robot.Link(1).Actuator.ke = 100;
robot.Link(2).Actuator.ke = 80;
robot.Link(3).Actuator.ke = 40;
robot.Link(4).Actuator.ke = 6;

% ------------------------------------------------------------------------
% -- Elastic transmission: viscous damping in the spring with respect to the
%    joint[Nms/rad].
% ------------------------------------------------------------------------
robot.Link(1).Actuator.de = 0.05;
robot.Link(2).Actuator.de = 0.05;
robot.Link(3).Actuator.de = 0.05;
robot.Link(4).Actuator.de = 0.05;

% ------------------------------------------------------------------------
% -- Equilibrium shift factors caused by tendon coupling
% ------------------------------------------------------------------------
robot.Link(4).Actuator.equilibriumShiftFactors = [0 0 -0.5 0];


% ========================================================================
% -- Controller + Observer
% ========================================================================
```

```
% ------------------------------------------------------------------------
% -- Controller parameters
% ------------------------------------------------------------------------
% -- Controller parameters for model-based dynamic compensation (joint and
%    motor trajectory)
robot.kp_q = [5, 5, 5, 5]' * 50;
robot.kd_q = [1, 1, 1, 1]' * 50;
robot.ki_q = [0 0 0 0]';
robot.kp_theta = [5, 5, 5, 5]' * 45;
robot.Controller.maxOutputTorque = [10 10 10 10];

% -- Activate controller.
robot.Controller.activateController = 1;
robot.Controller.activateGravityCompensation = 1;
robot.Controller.activatePIDController = 1;
```

A.3 Simulation Script for Initialization of Contact Model Parameters

```
function contact = ContactParameters( )

% ========================================================================
% Create Contact Object
% ========================================================================
contact = EjRobot.Contact();

% ------------------------------------------------------------------------
% Collision model
% ------------------------------------------------------------------------
% -- Ground position (z-axis)
contact.z_coll = 0.185;

% -- Vertical collision force constant [N/m]
contact.k_coll = 1e4;

% -- Nonlinear damper [Ns/m^2]
contact.lambda_coll = 5e5;

% ------------------------------------------------------------------------
% -- Ground friction model parameters (tangential components)
% ------------------------------------------------------------------------

% -------------------------------
% -- Kinetic (dynamic) friction
% -------------------------------
% -- Sliding friction coefficient []
contact.mu_fric_slide = 0.4;

% -- Sliding friction to stiction transition velocity limit [m/s]
contact.v_fric_to_stic = 0.001;

% -------------------------------
% -- Static friction (stiction)
% -------------------------------
% -- Maximum stiction force coefficient []
%    mu_stic >= mu_fric_slide !
contact.mu_stic = 0.4;

% -- Horizontal ground interaction stiffness [N/m]
contact.k_stic = 1e4;

% -- Stiction damper [Ns/m]
contact.d_stic = 4;

end
```